High-Fidelity Aerostructural Design Optimization of Transport Aircraft with Continuous Morphing Trailing Edge Technology

by

David A. Burdette Jr.

A dissertation submitted in partial fulfillment
of the requirements for the degree of
Doctor of Philosophy
(Aerospace Engineering)
in The University of Michigan
2017

Doctoral Committee:

Professor Joaquim R. R. A. Martins, Chair
Associate Professor Karthik Duraisamy
Associate Professor Krzysztof J. Fidkowski
Professor Yin L. Young

David A. Burdette Jr.

daburdet@umich.edu

ORCID iD: 0000-0001-5128-8436

To my family, who has always supported me and without whom none of this would have been possible.

To Ally, whose love, patience, and support has meant everything to me.

ACKNOWLEDGEMENTS

I have a large number of people I would like to acknowledge for helping me reach this point. First, I want to say thank you to my adviser, Professor Joaquim R.R.A. Martins. I have learned so much from you over the past few years as a member of the MDOLab, academically, professionally, and personally. The way I think about engineering design (and everything else in life that can be optimized) has been forever changed thanks to your class and my interactions with you, and for that I am truly thankful.

I would also like to thank the other members of my committee: Professor Karthik Duraisamy, Professor Krzysztof Fidkowski, and Professor Yin Lu Young for their helpful suggestions and thoughtful consideration of my thesis.

The other members of the MDOLab were a crucial aspect of my success at the University of Michigan. I would particularly like to thank Dr. Gaetan Kenway, with whom I worked closely and learned much from, and whose work laid the groundwork for much of what I was able to accomplish. I would also like to thank Dr. John T. Hwang, who initially introduced me to MDO, and was my inspiration for joining the MDOLab. Other members of the lab with whom I worked directly and would like to thank include Zhoujie (Peter) Lyu, Jason Kao, Justin Gray, John Wurts, Sicheng He, Tim Brooks, Eirikur Jonsson, Sandy Mader, Ney Secco, Tristan Dhert, Song Chen, Yin Yu, Nicolas Bons, Shamsheer Chauhan, and John Jasa. I couldn't have hoped for a better group of people to work with during my graduate studies.

Next I would like to thank my professors, both at the University of Michigan and

Syracuse University. In particular I would like to thank Dr. John F. Dannenhoffer III, my adviser during my undergraduate years at Syracuse. He was a truly inspiring mentor, who cemented my decision to pursue aerospace engineering during his introduction to engineering class in 2009.

Special thanks go to my friends and colleagues, who through their support and friendship have helped me become the person I am: John Dannenhoffer IV, Justin Storms, Alex Russomano, Kyle Hanquist, Joel Hartenberger, Yevgeniy Yesilevskiy, Narayanan Kidambi, Dakotah Thompson, Christopher Petersen, Adam Jardine, Michelle Lynde, Katie Reichl, Ben Houston, Daniel Gorski, Daniel Ghitman, Robert Ross, Alex Killebrew, Nathan Travis, Liz Weeden, Chip Murphy, and Erik Holmes.

Finally, I would like to extend my most sincere gratitude to my family who has always provided the strongest and most important support in my life. First to my brothers Daniel and James: Thank you for always challenging me to be my best. I am inspired by both of your successes, and am proud to call you both my brothers. Next, to Ally: Thank you for being eternally patient through the late nights, limited communication, and distance. Without your patience, understanding, and support, this would not have been possible. Finally, to my parents: Thank you so much for all of the sacrifices you both made to make this possible for me. Know that I am forever grateful for all that you have done for me, and that I consider myself extremely lucky to have been born your son.

TABLE OF CONTENTS

LIST OF FIGURES

Figure

LIST OF TABLES

Table

LIST OF ABBREVIATIONS

MDO Multidisciplinary Design Optimization

FFD Free Form Deformation

CFD Computational Fluid Dynamics

RANS Reynolds-Averaged Navier–Stokes

SA Spalart–Allmaras

CSM Computational Structural Mechanics

CRM Common Research Model

ADODG Aerodynamic Design Optimization Discussion Group

uCRM undeflected Common Research Model

ATAG Air Transport Action Group

TBW Truss Braced Wing

BWB Blended Wing Body

AFRL Air Force Research Lab

NASA National Aeronautics and Space Administration

MFC Macro Fiber Composite

AFTI Advanced Fighter Technology Integration

MAW Mission Adaptive Wing

DARPA Defense Advanced Research Projects Agency

SMA Smart Memory Alloy

LaRC Langley Research Center

TDT Transonic Dynamics Tunnel

UCAV Uninhabited Combat Air Vehicle

MAS Morphing Aircraft Structures

VCCTEF Variable Camber Continuous Trailing Edge Flap

UAV Unmanned Aerial Vehicle

CMA-ES Covariance Matrix Adaptation Evolution Strategies

GAs Genetic Algorithms

PSOs Particle Swarm Optimizations

TOGW Take Off Gross Weight

AD Automatic Differentiation

ACTE Adaptive Compliant Trailing Edge

GTM Generic Transport Model

RMTS Regularized Minimal-energy Tensor-product Spline

ABSTRACT

High-Fidelity Aerostructural Design Optimization of Transport Aircraft with Continuous Morphing Trailing Edge Technology

by

David A. Burdette Jr

Chair: Joaquim R. R. A. Martins

Adaptive morphing trailing edge technology offers the potential to decrease the fuel burn of transonic commercial transport aircraft by allowing wings to dynamically adjust to changing flight conditions. Current configurations allow flap and aileron droop; however, this approach provides limited degrees of freedom and increased drag produced by gaps in the wing's surface. Leading members in the aeronautics community including NASA, AFRL, Boeing, and a number of academic institutions have extensively researched morphing technology for its potential to improve aircraft efficiency.

With modern computational tools it is possible to accurately and efficiently model aircraft configurations in order to quantify the efficiency improvements offered by morphing technology. Coupled high-fidelity aerodynamic and structural solvers provide the capability to model and thoroughly understand the nuanced trade-offs involved in aircraft design. This capability is important for a detailed study of the capabilities of morphing trailing edge technology. Gradient-based multidisciplinary design optimization provides the ability to efficiently traverse design spaces and optimize the

trade-offs associated with the design.

This thesis presents a number of optimization studies comparing optimized configurations with and without morphing trailing edge devices. The baseline configuration used throughout this work is the NASA Common Research Model. The first optimization comparison considers the optimal fuel burn predicted by the Breguet range equation at a single cruise point. This initial singlepoint optimization comparison demonstrated a limited fuel burn savings of less than 1%. Given the effectiveness of the passive aeroelastic tailoring in the optimized non-morphing wing, the singlepoint optimization offered limited potential for morphing technology to provide any benefit. To provide a more appropriate comparison, a number of multipoint optimizations were performed. With a 3-point stencil, the morphing wing burned 2.53% less fuel than its optimized non-morphing counterpart. Expanding further to a 7-point stencil, the morphing wing used 5.04% less fuel. Additional studies demonstrate that the size of the morphing device can be reduced without sizable performance reductions, and that as aircraft wings' aspect ratios increase, the effectiveness of morphing trailing edge devices increases. The final set of studies in this thesis consider mission analysis, including climb, multi-altitude cruise, and descent. These mission analyses were performed with a number of surrogate models, trained with $\mathcal{O}(100)$ optimizations. These optimizations demonstrated fuel burn reductions as large as 5% at off-design conditions. The fuel burn predicted by the mission analysis was up to 2.7% lower for the morphing wing compared to the conventional configuration.

CHAPTER 1

Introduction

1.1 Motivation

Worldwide demand for sustainable initiatives to combat climate change is influencing the aerospace market. The aerospace industry is responding with a clear push for aircraft transportation solutions with increased efficiency and reduced emissions. Leaders in industry, academia, and government agencies around the world are investing in research pursuing more efficient aircraft technologies.

The airline industry is a substantial contributor to greenhouse gas emissions. According to the Air Transport Action Group (ATAG), aircraft emissions contributed 781 million metric tons of CO_2 to the Earth's atmosphere in 2015 [1]. That value is more than 2% of the total 36 billion metric tons produced by humans that year. CO_2 emissions are the major driver in aviation's long-term impact on Earth's climate, while other emissions—of nitrogen oxides (NO_x) and particulates like soot and sulfates—and the production of contrails and cirrus clouds contribute shorter-term impacts. In 2005, aviation's radiative forcing—a measure of the change in energy in the atmosphere—was an estimated 78 mW m^{-2}, or 4.9% of that year's anthropogenic forcing [2]. Figure 1.1 demonstrates the dire circumstances surrounding the atmospheric concentrations of CO_2 and NO_x, and the dramatic shift these concentrations have made in the last 250 years. Changes need to be made in order to slow

these trends and to mitigate the heating of our planet. One such change is increasing the energy efficiency and reducing the emission production of aircraft to help reduce anthropogenic contributions to climate change.

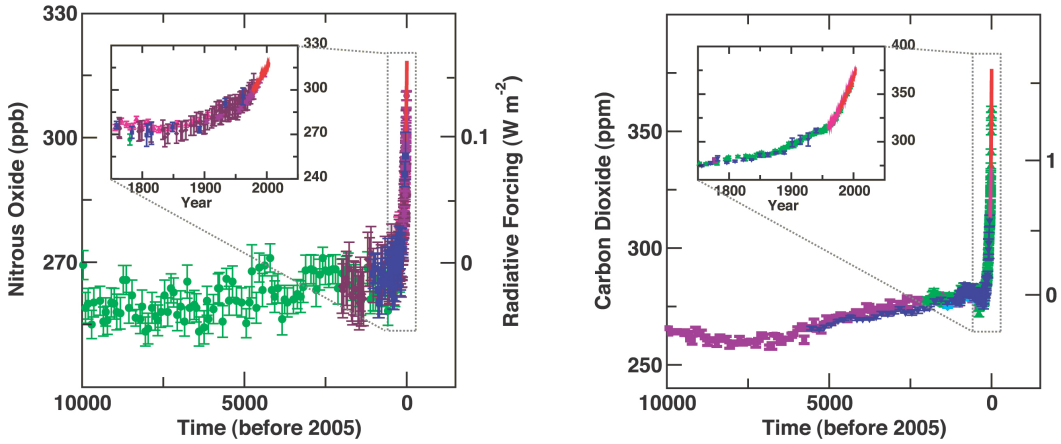

Figure 1.1: There has been a dramatic increase in atmospheric concentrations of CO_2 and NO_x in the past 250 years compared with the global history over the last 10,000 years. Adapted from Figure SPM.1 of IPCC [3].

Aircraft researchers are pursuing a number of options to continue improving aircraft fuel efficiency, including aerodynamic flow control [4], advanced materials and composites [5, 6, 7], improved engine technology [8, 9], electric propulsion [10], laminar flow design [11], morphing technology [12], and new (non tube-and-wing) aircraft configurations, like the Truss Braced Wing (TBW) [13, 14], Blended Wing Body (BWB) [15, 16, 17], and double bubble D8 [18, 19].

The studies in this thesis consider the effectiveness of morphing technology for improving fuel efficiency of commercial transport. While morphing technology has potential applications in military and unmanned applications, where performance requirements may dictate flight at a wide variety of flight conditions, those cases are not considered herein. Commercial aircraft contribute the majority of the fuel consumption among aircraft [20], and the long range and transonic speeds of their missions suggest they offer significant potential for reducing the overall fuel consumption of aircraft.

To motivate this work, we consider a variety of previous work in the area. We first consider general theory and historical perspectives of morphing technology. We then reduce the scope of our consideration and focus on previous work considering morphing trailing edge technology. In this work, I use Multidisciplinary Design Optimization (MDO) [21, 22] to determine optimized morphing trailing edge shapes and thus find the maximum potential of such devices. As such, we consider previous work in the field of MDO, particularly with applications in aircraft design. Finally, we consider specifically the state of the art with respect to MDO of morphing trailing edge devices and what needs in the field are addressed in this work. That motivation sets the table for the objectives and outline of the remainder of this thesis.

1.1.1 Morphing technology

Various researchers have different opinions about what qualifies as aircraft morphing. The broadest view, like that used by Weisshaar [23] and adopted by Martins [24] considers "a broad range of air vehicles and vehicle components that adapt to planned and unplanned multipoint mission requirements" as morphing aircraft. This includes changes like deployment and storage of landing gear, or use of high-lift devices. While the semantics of what does and does not qualify as a morphing device may be a point of debate among scholars in the field, the objective of morphing technology is clear. Actively altering the defining characteristics of an aircraft in flight provides increased aerodynamic performance at a wide range of flight conditions. An adaptive morphing configuration can tailor its performance for a variety of flight conditions. In the case of landing gear, the ability to retract landing gear provides a substantial drag reduction for the majority of a flight, when a deployed landing gear is not required. Similarly, high-lift devices enable low speed flight, which is required for safe takeoff and landing, while maintaining efficient aerodynamic performance at cruise.

Within this general definition of morphing, deformations of any control surface,

like ailerons, elevators, or rudders, constitute morphing. This type of conventional control surface approach—using a series of rigid actuated sub-surfaces on a wing to produce adaptive flight performance—is one of two approaches used historically. Alternatively, non-rigid, compliant structures can be used as control surfaces. These compliant surfaces can be deformed through actuation involving applied loading. This approach more closely mirrors that of flying animals. While the first approach with rigid control surfaces seems more intuitive given the current state of aircraft, the compliant morphing approach dates back to earlier days in manned aviation. The Wright Flyer in 1903 achieved roll control using compliant morphing structures. Specifically, the wing twist of the biplane was adjusted in flight using a series of cables. This compliant wing control system is shown in Figure 1.2

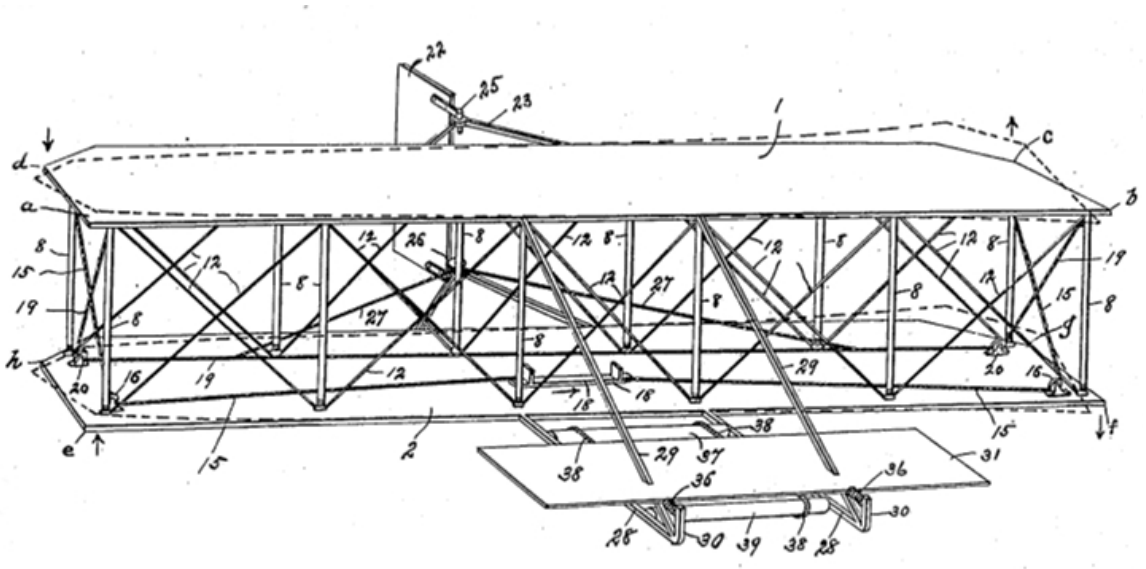

Figure 1.2: The compliant wing control approach used by the Wright brothers is visible in images from their 1903 patent application [25].

A large subset of morphing technologies within the general definition defined above involve wing morphing. Wing morphing can be divided into three classifications: planform alteration, out-of-plane transformation, and airfoil adjustment [26]. Planform alterations include changes to wing span, chord, and sweep. Out-of-plane transfor-

mations include changes to the wing's twist, dihedral, or spanwise bending. The third classification, airfoil adjustments, includes changes to the wing's camber and thickness. Weissharr [23] assembled a thorough review of morphing wing technology including historical perspectives, and Barbarino [12] reviewed the history of morphing technologies in aircraft, including considerations of morphing mechanisms.

Throughout history there have been a number of aircraft designs that utilized planform alteration. Many aircraft have used variable sweep to reduce the required speed and distance at both takeoff and landing while reducing wave drag at supersonic speeds. One of the earliest aircraft to test variable sweep technology was the Bell X-5. Other aircraft that utilized variable sweep include the F-111 Aardvark, the MIG-23, the F-14 Tomcat, and the B-1 Lancer, among several others. There are fewer examples of variable span aircraft, although some examples include the telescoping French MAK-10 in the 1930's and the German Akaflieg Stuttgart FS-29 glider in the 1970's. Span changes are used to increase an aircraft's range and endurance. At cruise the span is increased, to increase the wing's efficiency and reduce the induced drag. At high-load cases, the span is decreased, reducing the root bending moment and allowing for a lighter structure than what would be required without variable span capabilities.

There have also been a number of aircraft that utilized out-of-plane morphing. The Wright Flyer was an early example of a variable twist aircraft. The XB-70 Valkyrie utilized a hinged region of the wing, allowing for the outer region to bend downward at supersonic speeds for improved performance. The Lockheed Martin Defense Advanced Research Projects Agency (DARPA) Morphing Aircraft Structures (MAS) aircraft dramatically bends its wing out of plane for both cruise and dash performance [27]. More recently, the Boeing 777X has been designed to utilize folding wingtips to meet gate size constraints at airports, while allowing higher aspect ratios and better performance in flight.

While the Wright Flyer utilized compliant structures to achieve aircraft morphing, the vast majority of morphing following it for the next 60-70 years utilized articulation of rigid components, as evidenced in many of the examples above. As time passed and aircraft performance requirements became more demanding, the use of heavier, less compliant materials became necessary to support the aerodynamic and structural loads on the aircraft. This trend limited the use of compliant morphing for many decades, and led to the various hinged and actuated global morphing approaches previously discussed. With relatively recent materials science technology improvements, it has again become possible to utilize local compliant morphing within structures that are strong enough to support the required loads. As such, starting in the 1980's a number of programs were started that developed aircraft designed to study airfoil adjustment morphing.

In the 1980's, National Aeronautics and Space Administration (NASA) and the United States Air Force started the AFTI project. Within the project, an F-111 was retrofitted with a MAW developed by Boeing [28]. This wing included variable camber leading and trailing edge devices, with a continuous, compliant skin. As such, this configuration largely removed the losses produced by the edges of control surfaces, while allowing the wing to morph for performance at subsonic, transonic, and supersonic conditions. This configuration additionally included distributed pressure sensors and a closed control loop prescribing the morphing shapes. The AFTI study demonstrated the ability of variable camber technology to improve performance at cruise and maneuver, and reduce wing loading [29]. The study additionally demonstrated an effective variable camber control algorithm that was transparent to the pilot. The AFTI aircraft with adapted wing camber on the leading and trailing edges is shown in Figure 1.3.

Later, in collaboration with DARPA, NASA funded the Aircraft Morphing Program, building off the results from the AFTI. The program's goal was "the devel-

Figure 1.3: The retrofit wings on the AFTI test aircraft included supercritical MAW devices on the leading and trailing edges.

opment of smart devices using active component technologies to enable self-adaptive flight for a revolutionary improvement in aircraft efficiency and affordability." [30] While previous studies had not led to integration of variable camber technology on a number of aircraft, the project sought to advocate for the benefits of the technology by explicitly identifying applications of the technology that offered the best cost-to-benefit ratio. The program focused on four areas:

- Improved health monitoring to reduce operations and maintenance costs by 10%
- Wing bending load alleviation of 30%
- Noise reduction of 3 dBA
- Flow separation control yielding a 15% lighter high-lift system

In the late 1990's, the Smart Wing program, funded by DARPA, the Air Force Research Lab (AFRL), and NASA, in partnership with Northrop Grumman Corporation, developed and demonstrated smart technologies for use on military aircraft. The project was divided into two phases. In Phase 1, a smart structure consisting of Smart Memory Alloy (SMA) torque tubes was designed and built on a 16% scale

model. That model was then tested in the NASA Langley Research Center (LaRC) Transonic Dynamics Tunnel (TDT). The model demonstrated performance improvements of 8-12% compared to the conventional configuration with rigid flaps [31]. In Phase 2, they made a number of improvements. A full-span 30% scale model of a Northrop Grumman Uninhabited Combat Air Vehicle (UCAV) with one conventional wing and one smart wing with morphing leading and trailing edges was fabricated and tested at representative flight conditions [32]. The second phase also tested rapid-morphing "eccentuators" driven by ultrasonic piezo-electric motors. The morphing mechanism demonstrated high deflection rates and limits, and produced improvements of 15% in both the rolling and pitching moment coefficients [33].

This thesis focuses on airfoil adjustments, specifically, variable camber. Multiple approaches exist for achieving variable camber, although the majority of current research revolves around morphing devices at the leading and trailing edges. In this thesis, I focus specifically on continuous morphing trailing edge technology. The next section presents the current state of research beyond large-scale government programs involving morphing trailing edge devices.

1.1.2 Morphing trailing edge background

A sizable amount of recent and current research is dedicated to developing and studying morphing mechanisms. The design of such devices can be very challenging, given the simultaneous and potentially conflicting design goals associated with a morphing trailing edge device. On one hand, the device should require relatively small actuation loads, to mitigate the losses associated with the weight and power requirements of the morphing actuators. Conversely, the skin over the morphing region needs to support the aerodynamic loads encountered in flight without adversely affecting the outer mold line of the wing. Additional challenges arise from the changes in the wetted area of the wing resulting from camber morphing. A morphing trailing edge

mechanism design needs to address all of these challenges without adding substantial weight to the aircraft. In essence, a morphing mechanism design needs to manage the trade-offs between the weight of the mechanism, the ability of the mechanism to support aerodynamic loads, and the device's morphing capability.

Szodruch and Hilbig [34] published a comprehensive study including analytic and experimental considerations of morphing devices for civil transport aircraft and military applications. Reckzeh [35] described Airbus' current approach to wing movables, and how variable camber at cruise can be used for load control. Molinari *et al.* [36, 37] explored the benefits of continuous morphing trailing edge technology using low-fidelity aerodynamic models and has subsequently manufactured and tested a piezoelectric adaptive wing. Pankonien [38] studied a variety of topics pertaining to morphing trailing edge devices for unmanned aerial vehicles (UAVs), including the development of a modular smart material morphing aileron with embedded positional sensing, an additively manufactured elastomeric skin, and a hybrid morphing aileron consisting of multiple smart materials.

Some morphing designs have a high technology readiness level, and are rapidly approaching commercial availability. One such design is the FlexSys FlexFoil. The FlexFoil provides a smooth and continuous control surface with spanwise variability [39, 40], like the morphing mechanisms designed throughout this thesis. Rather than using smart materials like many others researching airfoil morphing technology, FlexSys utilizes internal global compliant mechanisms. These mechanisms employ compliant structural technology; however, the novelty comes in the global distribution of the compliance to avoid large localized strains. This design approach produces strong, joint-less, scalable, lightweight, fatigue-resistant, monolithic morphing mechanisms that have thus far demonstrated promising results. As a demonstration of the feasibility of this mechanism, in collaboration with NASA and the AFRL, FlexSys retrofitted a FlexFoil on a Gulfstream GIII business jet and performed a series of

flight tests [41]. Figure 1.5 shows the retrofitted aircraft with the morphing device that was used for those flight tests. Those tests were primarily intended to validate the structural integrity of the morphing device, but a number of additional flight tests are being planned and conducted, including higher speed flights, flights with span twist, and installation and testing on a Boeing KC-135 Stratotanker [41]. While these and other flight tests are still required for full validation of the device's capabilities, the morphing mechanism can be considered for next generation aircraft design in the near future.

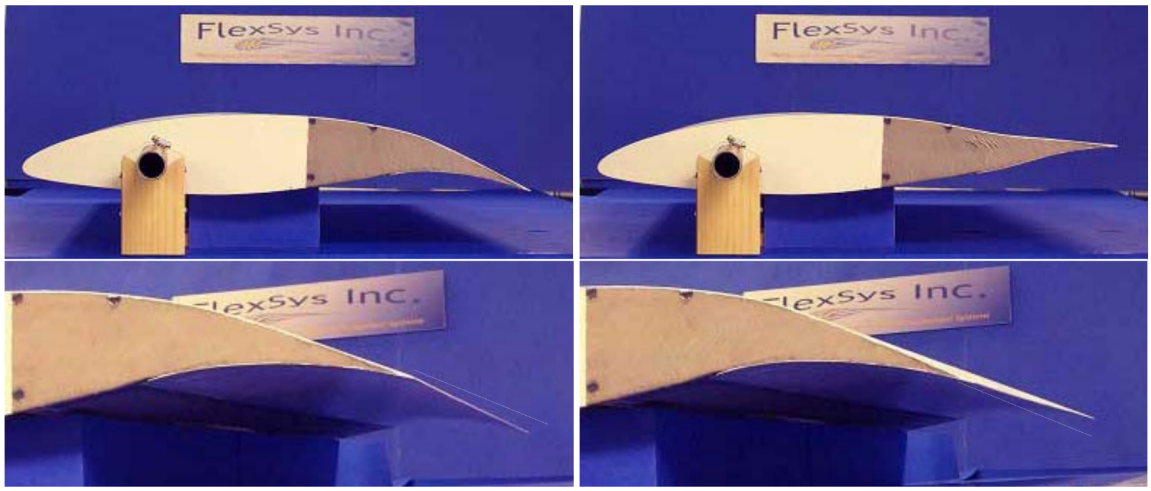

Figure 1.4: A demonstration of a FlexSys morphing trailing edge device undergoing a $\pm 10^{\circ}$ flap deflection with a 3° twist [42].

Given the wide variety of morphing mechanisms in literature, and the lack of consensus among researchers working on morphing technology about what type of mechanism is best suited for use on commercial transport aircraft, this thesis does not include explicit modeling of a morphing mechanism. Instead, general shape changes are prescribed, and we assume that the morphing mechanism can achieve the desired shapes. By removing restrictions on the morphing capabilities, we can identify an ideal limit of the potential efficiency improvements morphing technology offers. Even with this general approach, the final morphing shapes designed in this work are

Figure 1.5: The 19–foot ACTE device installed on the testbed aircraft used in flight tests in 2014, deflected at 20° [43].

achievable by at least a subset of current morphing wing technology [44].

1.1.3 Multidisciplinary design optimization

The aircraft design process has evolved dramatically over the past 100 years. The introduction of computational models and methods has had a particularly substantial influence on the aircraft design process over the past 40 years. In the past, extensive suites of expensive experimental tests were required to analyze aircraft designs. Over the past few decades, verified and validated computational models have been increasingly used in place of physical experiments. This shift has been enabled by improvements of both computational hardware and analysis software. The fidelity and robustness of analysis tools including both Computational Fluid Dynamics (CFD) and Computational Structural Mechanics (CSM) have improved dramatically. These computational analysis methods can be particularly valuable for studying new configurations or technologies, for which engineering intuition may be limited. Improved robustness and fidelity of computational models additionally enables the use of computational design and optimization tools. MDO is of particular interest in this thesis

because of its ability to leverage these analysis tools to generate optimal aircraft designs.

Optimization problems are formulated as a minimization of an *objective function* with respect to *design variables* subject to a number of *constraints*. To give a few concrete examples within the context of aircraft design optimization, potential objective functions include fuel burn, Take Off Gross Weight (TOGW), and drag. Design variables could be the wing shape, the aircraft's flight conditions, and the structural layout. Constraints are used to limit the design space and produce physically feasible optimization results, and might include limits on: geometric shape changes, lift, pitching moments, and structural stresses. Additional objective functions, design variables, and constraints are used throughout this thesis.

There are two major approaches within design optimization: gradient-free methods and gradient-based methods. Gradient-free methods such as Genetic Algorithms (GAs) [45] and Particle Swarm Optimizations (PSOs) [46] use populations to explore design spaces. These methods are in general more likely to produce a result closer to a global minimum, and are therefore valuable for multimodal design spaces. These methods are additionally valuable for problems with discontinuous design spaces, discrete design variables, and otherwise non-differentiable functions. One of the most substantial issues with gradient-free methods is their computational cost. They may perform relatively well for cheap objective and constraint functions with relatively few design variables; however, a large number of design variables leads to exceedingly slow gradient-free optimizations [47] that produce solutions that are not guaranteed to be minima.

Gradient-based methods use not only objective function and constraint value information, but also information about the gradients of those functions. Including gradients and intelligently using this information allows gradient-based methods to produce local minima using a much smaller number of function evaluations than are

required in gradient-free methods [47]. The computationally expensive functions of interest and large number of design variables used in this thesis necessitate the use of gradient-based methods.

Effective use of gradient-based methods requires efficient and accurate gradient calculation. While finite-difference methods for approximating derivatives are quite simple to implement, they suffer from accuracy and efficiency problems. The complex-step method [48] removes the subtractive error that largely limits the accuracy of finite-difference derivatives, but they still require one function evaluation per derivative value, making them prohibitively expensive for a large number of design variables. The solution which allows for efficient gradient calculation is the adjoint method, in which the cost of a gradient calculation is nearly independent of the number of design variables. Martins and Hwang [49] reviewed derivative computation methods and provided a unifying theory from which each calculation method can be derived. The synergistic use of the adjoint method and gradient-based optimization methods yields efficient optimization algorithms capable of handling the large design spaces required for high-fidelity aircraft shape and size optimization. The adjoint implementation used in this work additionally leverages the Automatic Differentiation (AD) approach to efficiently calculate partial derivatives within the coupled system [50].

Adjoint-supported gradient-based optimization has been used extensively in aerodynamic shape optimization. Jameson [51] first demonstrated adjoint-based shape optimization using the Euler equations. That work was expanded to full aircraft configurations and multipoint problem definition [52, 53]. Additional developments enabled optimization of non-planar wings [54] and additional design variation by providing more robust mesh movement [55].

Modern design of transonic aircraft requires the use of the RANS equations with a turbulence model [56]. As the Euler equations do not include a model of viscous effects, the influence of the boundary layer on shock development cannot be accurately

captured. This means that wave drag at transonic conditions cannot be accurately captured. This requirement of RANS analysis for transonic wing design is explicitly demonstrated in Chapter 3.

Again, Jameson [57] first demonstrated adjoint-based optimization using the RANS equations in 1998. Nielsen [58] demonstrated a 3-D implementation of a discrete adjoint of the RANS equations, and subsequently used them for aerodynamic shape optimization. Lyu and Martins [59] performed a wide variety of gradient-based aerodynamic shape optimizations using the RANS equations.

These optimization techniques allow for the detailed shape optimizations required for aerodynamic transonic wing design; however, they do not include the structural deflections experienced by the wing. To capture these effects, the aerodynamic CFD solver must be coupled with a CSM solver. Haftka [60] produced some of the earliest coupled aerostructural optimization results, using a low-fidelity aerodynamic panel method coupled with a finite element structural model. Martins [61] first proposed and used a coupled adjoint method for aerostructural optimization. This approach allowed for the efficient adjoint-based gradient calculations nearly independent of the number of design variables discussed previously for aerodynamic-only optimization, including coupled derivatives. In that work, an Euler-based CFD solver was coupled with linear finite element analysis. This method was used to optimized the aerodynamic shape and structural sizing of a supersonic business jet [62]. Kenway and Martins [63, 64] later demonstrated multipoint coupled aerostructural optimization of the NASA Common Research Model (CRM) with RANS CFD coupled to a linear finite element model. Similar methods have been used in the design of wind turbines [65] and hydrofoils [66].

1.1.4 Optimization of morphing trailing edge aircraft

Given the state of morphing trailing edge technology in the aircraft industry and the substantial capabilities demonstrated by MDO techniques shown in the previous subsection, there is a natural fit for application of MDO techniques to morphing trailing edge design. MDO of morphing devices can maximize the performance benefits provided by the technology, increasing the incentive to include the technology in future aircraft designs or retrofit aircraft upgrades. Given this natural pairing, a number of researchers have already used MDO in morphing device design.

Henry [67] performed optimization of a morphing configuration using piezoelectric Macro Fiber Composite (MFC) patches for improved roll control. Gamboa [68] performed aerodynamic optimization and sequential aerostructural analysis of a morphing trailing edge wing for a Unmanned Aerial Vehicle (UAV). Using the gradient-free Covariance Matrix Adaptation Evolution Strategies (CMA-ES) optimization algorithm [69] and low-fidelity models, Molinari [36] optimized the aerodynamic shape and structural sizing of a morphing wing using dielectric elastomers. This work demonstrated the need for coupled aerostructural optimization as opposed to a sequential approach. The use of such low-fidelity models has been shown to be insufficient for capturing the small shape changes which can have dramatic influence on transonic wing design [15]. Lyu and Martins [70] used high-fidelity aerodynamic analysis and optimization to investigate the benefits associated with continuous morphing trailing edge technology for the NASA CRM, and found aerodynamic drag improvements of between 1 and 5% depending on how far the flight condition was from the design point. Nguyen *et al.* [71, 72, 73] have done extensive aerodynamic work studying the NASA Generic Transport Model (GTM) with Variable Camber Continuous Trailing Edge Flap (VCCTEF) devices, which consist of a series of small flaps joined with an elastic material on the wing's trailing edge. Stanford [74] also studied the VCCTEF, applying the technology to the undeflected Common Research Model (uCRM)

configuration. His study used a detailed structural wing box model with torsional springs and point loads modelling morphing actuators. The aerodynamic loading in that analysis was computed using panel methods. The study considered morphing technology's effect on flutter and maneuver alleviation, and included open loop load cases where morphing devices were not used. The open loop load cases proved to be critical in measuring the potential benefits of morphing trailing edge technology. Wakayama [75] used low-fidelity vortex lattice aerodynamic and monocoque beam structural models to perform aerostructural optimization of a morphing trailing edge device on three commercial transport–sized aircraft: a hybrid wing body (224 seats), a wide-body transport (222 seats), and a narrow-body transport (154 seats). That study additionally included weight penalties for the weight of morphing mechanisms, actuators, and hydraulics. These weight penalties were based on theoretical estimates of aerodynamic hinge moments and estimates of the force required to overcome the compliant structural stiffness. Comparing optimized designs with and without morphing, this study found fuel burn savings of 0.7%, 0.9%, and 3.0% for the hybrid wing body, narrow-body transport, and wide-body transport, respectively. The large fuel burn reduction for the wide-body transport (relative to the other configurations) was attributed to that configuration's control surface arrangement and its large wing weight relative to its overall weight.

While there have been a number of studies using MDO for morphing device design, the state of the art in this field has a number of shortcomings. The vast majority of the work involving optimization of morphing trailing edge devices falls victim to at least one of three common shortcomings: they use low-fidelity analysis like panel-method based aerodynamics, they consider only single discipline analysis (typically aerodynamic or structural), and they use a small number of non-general design variables. Even with these shortcomings, such analyses can approximate the savings provided by morphing technology; however, low-fidelity models often lack the fidelity required

to accurately design transonic aircraft. Given that the fuel burn savings provided by morphing technology are on the order of 1%, modeling or numerical errors on that same order make quantification of fuel burn savings inaccurate. Additionally, in most of the morphing trailing edge optimization literature, only a few flight conditions are typically considered. Rather than modeling the performance throughout a full mission, performance measurements are typically limited to a few cruise conditions. This approach is effectively a low-fidelity approximation of the mission discipline.

Given the benefits of morphing technology in providing performance robustness at a wide variety of conditions, analysis that does not appropriately represent the entirety of a mission likely does not accurately quantify the performance benefit provided by morphing devices. Many of these shortcomings in the literature are a result of approximations made to limit the computational costs of analyses and optimizations. While addressing many of these shortcomings can be computationally expensive, the work in this thesis seeks to efficiently address these needs in the field.

1.2 Thesis objectives

The primary goal of this thesis is to quantify the fuel burn savings potential of morphing trailing edge technology for commercial transport sized aircraft using high-fidelity gradient-based aerostructural design optimization. More specifically, to address the needs mentioned above I set the following objectives for this thesis:

1. Demonstrate the need for high-fidelity simulations in transonic aircraft design
2. Compare aircraft optimized with and without morphing at a single and at multiple design points
3. Repeat the comparison of morphing vs. conventional optimized wings for a next-generation high aspect ratio configuration

4. Find the aerodynamic benefit of morphing trailing edge technology for a full mission including climb and descent

5. Repeat the above mission analysis, adding the inclusion of structural deflections, both with and without an initial optimization for cruise performance

1.3 Thesis outline

To achieve the stated objectives, I utilize high-fidelity aerostructural design optimization to quantify the fuel burn savings provided by morphing trailing edge technology for commercial transport aircraft. The optimization framework and baseline geometries used throughout this thesis are described in Chapter 2. Before considering the implications of morphing, I first consider the importance of the fidelity of the computational models used herein. To address objective 1, in Chapter 3, I demonstrate the need for high-fidelity aerodynamic models for transonic wing design, and validate the use of such models, and their corresponding computational costs, in this thesis. Chapter 3 also describes the baseline geometry used throughout this work.

The remaining chapters of this thesis describe optimization results comparing wings with and without morphing trailing edges. In Chapter 4, I first consider the simplest optimization: a singlepoint aerostructural optimization with one maneuver condition. Building on those results, Chapter 5 describes a comparison of wings with and without morphing using multipoint optimization. The difference between singlepoint and multipoint optimization lies in the number of "cruise" conditions at which the configuration is analyzed for the calculation of fuel burn. In the multipoint optimizations of Chapter 5, there are stencils with three and seven such cruise conditions, respectively. These Chapters together address objective 2. The last subsection in the results of Chapter 5 completes objective 3, as I repeat the comparison between conventional and morphing wings for a higher aspect ratio configuration.

Such higher aspect ratios will become more reasonable with the development of next generation structures and composites. I pursued the higher aspect ratio configuration under the hypothesis that the increased wing flexibility associated with the higher aspect ratio would increase the benefits offered by morphing technology. Chapter 6 compares wings with and without morphing using a full mission analysis, supported by aerodynamic performance surrogates trained with $\mathcal{O}(100)$ optimizations. This Chapter includes aerodynamic-only and coupled aerostructural analyses, and therefore addresses objectives 4 and 5. Finally, in Chapter 7, I summarize the findings and contributions of this thesis, and suggest additional future work.

CHAPTER 2

Aerostructural design optimization framework

In this chapter, we present the optimization framework, and various computational tools within it, that were used in this work. Collectively, the tools are known as the MDO of Aircraft Configurations with High-fidelity (MACH) framework [63, 76]. The tools outlined herein have been used on a wide variety of aerodynamic [59, 77, 78] and aerostructural aircraft design optimization problems [79, 80, 81, 82] as well as optimizations of wind turbine blades [65] and hydrofoils [66].

2.1 Geometric parameterization

A wide variety of approaches have been followed for parameterizing aircraft geometry for optimization, as surveyed by Samareh [83]. The approach followed in our framework is the Free Form Deformation (FFD) parameterization. This technique originates in computer graphics [84], but has many features that make it particularly well suited for use in aircraft design optimization. The basic idea of the approach is to insert the geometry of interest into a bounding volume, which we refer to as the FFD, and then to create deformations of the volume (and anything contained therein) using a number of control points distributed over the FFD's surface. The FFD is defined as a tri-variate B-spline volume, so the transformation resulting from the control point deformations can be explicitly applied to the embedded geometry.

The FFD approach to geometric parameterization is effective for aircraft design optimization for a number of reasons. Unlike a number of other parameterization techniques, FFDs do not parameterize the surface itself, but rather the changes to the surface. As a result, the outer mold line (OML) of the geometry does not need to be approximated by any surface fitting operations, and therefore can exactly match a specified initial shape. This is a substantial benefit, as aerostructural optimization often starts with a specified initial configuration, and this approach can precisely match that design. This approach additionally avoids concerns about preserving a watertight geometric model, which is important for aerodynamic analysis. This parameterization of the geometric changes rather than the geometry itself also allows for design variables to be reused with slight variations to the geometry. An example demonstrating this situation is discussed in more detail in Section 3.2.4. Another benefit of this approach is its versatility in terms of design variable definition. Local geometric shape changes are enabled through movement of individual control points. Global geometric design variables (like span, sweep, dihedral, and twist) can also be defined, using simultaneous manipulations of multiple control points. In aerostructural optimization, the FFD approach also offers the benefit of simultaneously parameterizing both the aerodynamic and structural geometries, with no additional matching required. Finally, the use of the tri-variate B-spline interpolation functions to create surface deformations from control point changes allows for an analytic definition of the gradients of this transformation. This feature is extremely useful for application within an adjoint implementation which is required for gradient-based optimization of computationally demanding functions (like coupled CFD and CSM).

The FFD approach is versatile, as it allows for a wide variety of geometric design spaces. Much of the work throughout this thesis leverages FFDs with uneven spacing to define specific regions with high and low curvature. This enables the definition the locations of continuous morphing transition regions. Alternatively, as shown

by Lyu [85], nested sub-FFDs can be used to define nested regions of geometric deformation. Given this versatility and the many benefits noted above, the FFD approach lends itself well to use within the MACH framework. A number of different FFD configurations were used throughout this work, and an example of a relatively simple FFD is shown in Figure 2.1.

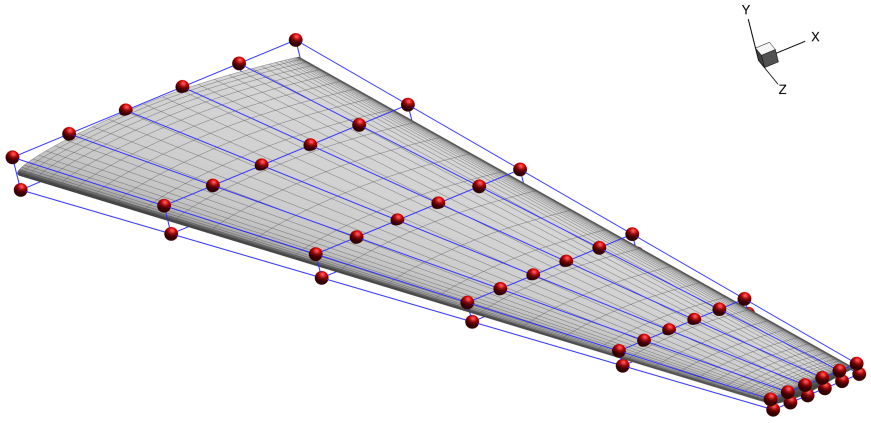

Figure 2.1: An example FFD with a total of 72 control points surrounding a wing.

The use of FFD parameterization in the morphing region is not typical in literature. Most morphing studies start with an assumed mechanism, and simulate associated simple morphing shapes, like a number of rigid rotations or a number of spanwise polynomial deformation profiles. The morphing deformations produced using FFDs in this work are more general. This relatively unrestrictive parameterization permits a wide variety of morphing shapes, which when coupled with gradient-based optimization allows the exploration of the potential of morphing technology, rather than the potential of a specific morphing mechanism. By avoiding preliminary design space reductions associated with specific devices, optimization results in this thesis represent mechanism-independent optimal shapes. While this approach is useful for quantifying the potential of general morphing technology, it additionally informs the design of morphing mechanisms. Mechanisms able to produce the shapes found in these studies

can produce the full savings possible with morphing technology, while more restrictive mechanisms yield reduced returns. This approach additionally demonstrates the types of deformations that are not needed for optimal returns. As such, these results demonstrate that weight penalties in morphing device design that enable a series of shapes that were not produced herein are likely not valuable (although a more complete analysis of all critical sizing conditions is required to definitively eliminate potential shapes). Given the diversity of morphing devices and their capabilities, optimization using this more general approach is preferable to analogous optimizations with specific morphing devices.

2.2 Mesh deformation

As described in the previous section, an FFD is used to generate the transformation from design variables to surface deformations. Once surface deformations are defined over the OML, those deflections need to be propagated to the remainder of nodes in the volume mesh. This transformation is referred to as mesh deformation, and is implemented in two different methods within the MACH framework. Both methods were used, although the second method described herein, pyWarpUStruct, proved to be more robust for many of the morphing cases.

2.2.1 pyWarp: Hybrid analytic and linear elastic warping algorithm

The first mesh warping implementation in the MACH framework is pyWarp, which uses a hybrid analytic, linear elastic algorithm. The method was developed by Kenway [86]. The linear elastic aspect of the algorithm is based largely on linear elastic structural deformation theory, which is a generally robust mesh deformation method, although it can be computationally expensive. In order to improve the computational efficiency of the method, a linear elastic deformation is applied to a coarsened version of the mesh, capturing the low frequency shape changes, and an analytic deforma-

tion is applied to represent the more localized, higher frequency shape changes. This hybridization produces an effective compromise between the robustness and computational cost of the warping algorithm.

2.2.2 pyWarpUStruct: Inverse distance weighting warping algorithm

The second mesh warping scheme in the MACH framework is pyWarpUStruct, which was used for the majority of the results in this thesis. pyWarpUStruct uses an explicit inverse distance weighted algorithm to propagate the surface deformations and rotations to the rest of the mesh, in a fashion similar to that outlined by Luke *et al.* [87]. The inclusion of the surface rotations in the mesh deformation helps to preserve surface perpendicularity in the deformed mesh. This feature of the warping algorithm is beneficial for the accuracy of the RANS simulations. This preservation of the mesh quality near the surface also proved to be particularly beneficial for optimization of morphing trailing edge configurations, which often produce surface deformations with substantial rotations localized near the trailing edge that were too large to be handled by other warping methods. A KD-tree produced with an efficient spatial search algorithm is used to improve the computational performance of the warping. Figure 2.2 shows a demonstration of the mesh warping algorithm applied on a high aspect ratio wing with a morphing trailing edge, with two spanwise slices of the mesh shown in red and blue for each configuration.

2.3 CFD solver

The aerodynamic flow solver used in the MACH framework is ADflow [88]. In this work, the primary set of governing flow equations solved by ADflow are the RANS equations, although the Euler equations (removing viscous terms) are used for comparison in Chapter 3. As a reference, the instantaneous compressible continuity

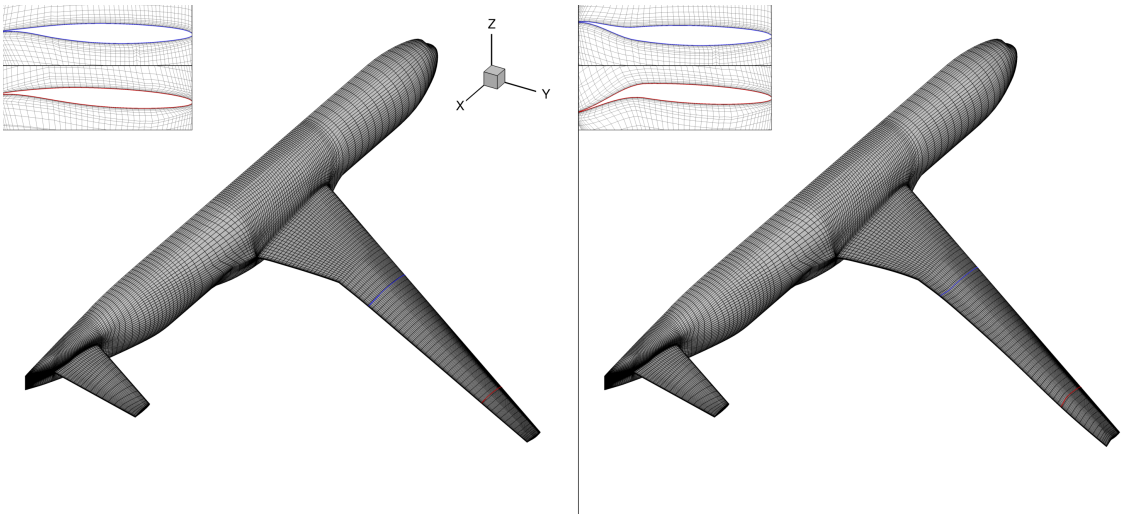

Figure 2.2: A comparison of an initial and warped mesh using pyWarpUStruct for an example morphing trailing edge deformation.

equations (mass, momentum, and energy) can be written in index notation as:

$$\frac{\partial \rho}{\partial t} + \frac{\partial}{\partial x_j}(\rho u_j) = 0 \tag{2.1}$$

$$\frac{\partial}{\partial t}(\rho u_i) + \frac{\partial}{\partial x_j}(\rho u_i u_j + p\delta_{ij} - \tau_{ji}) = 0 \tag{2.2}$$

$$\frac{\partial}{\partial t}(\rho e_0) + \frac{\partial}{\partial x_j}(\rho u_j e_0 + p u_j + q_j - u_i \tau_{ij}) = 0 \tag{2.3}$$

where

$$\tau_{ij} = 2\mu S^*_{ij} \tag{2.4}$$

$$S^*_{ij} = \frac{1}{2}\left(\frac{\partial u_i}{\partial x_j} + \frac{\partial u_j}{\partial x_i}\right) - \frac{1}{3}\frac{\partial u_k}{\partial x_k}\delta_{ij} \tag{2.5}$$

These equations are the basis upon which both the RANS and Euler equations used by ADflow are derived. For the RANS calculations, the set of equations is closed using a Spalart–Allmaras (SA) turbulence model. In this work ADflow is used as a cell centered multiblock solver of the steady governing equations, although additional capabilities include unsteady and time-spectral modes, and overset mesh solutions [89].

A coupled Newton–Krylov (NK) scheme is used to simultaneously solve the mean flow and turbulence equations. Gradients are computed in ADflow using a discrete adjoint approach [56].

2.4 Structural solver

The CSM solver in the MACH framework is the Toolkit for Analysis of Composite Structures (TACS) [90]. TACS is a parallel finite element solver that is designed for use on aircraft structures, particularly the thin shell components typical of wing box members, which often lead to poorly conditioned matrices in the governing equations. Those equations written as residuals are:

$$\mathcal{S}(d) = Kd - F = 0 \tag{2.6}$$

TACS additionally computes structural gradients using the adjoint method, often employing Kreisselmeier–Steinhauser function aggregation to limit the number of functions of interest.

2.5 Coupled aerostructural solver

The code that couples ADflow and TACS within MACH is pyAeroStruct. Before considering the coupled aerostructural equations, we first write the aerodynamic equations (2.1) – (2.3) as residuals:

$$\mathcal{A}(w) = 0 \tag{2.7}$$

where

$$w = \begin{bmatrix} \rho & \rho u_1 & \rho u_2 & \rho u_3 & \rho e_0 \end{bmatrix}^T \tag{2.8}$$

Then adding the structural residuals from 2.6, we have the coupled residual equation:

$$\mathcal{R} = \begin{bmatrix} \mathcal{A}(w,d) \\ \mathcal{S}(w,d) \end{bmatrix} = 0 \tag{2.9}$$

A rigid link approach [91, 61] is used to couple the aerodynamic and structural solutions. The surface nodes of the aerodynamic mesh are rigidly linked to structural nodes, allowing structural deformations to be extrapolated to the aerodynamic surface. Inversely, the method of virtual work is used to calculate a consistent force vector from the integrated aerodynamic loads, which is then applied to the structural model. The coupled equations are solved using a Gauss–Seidel solver. The derivatives are calculated using a coupled adjoint approach [49], summarized as:

$$\begin{bmatrix} \frac{\partial \mathcal{A}}{\partial w} & \frac{\partial \mathcal{A}}{\partial s} \\ \frac{\partial \mathcal{S}}{\partial w} & \frac{\partial \mathcal{S}}{\partial s} \end{bmatrix}^T \begin{bmatrix} \psi_{\mathcal{A}} \\ \psi_{\mathcal{S}} \end{bmatrix} = - \begin{bmatrix} \frac{\partial I}{\partial w} \\ \frac{\partial I}{\partial s} \end{bmatrix}, \tag{2.10}$$

$$\frac{\mathrm{d}I}{\mathrm{d}x_{dv}} = \frac{\partial I}{\partial x_{dv}} + \psi_{\mathcal{A}}^T \frac{\partial \mathcal{A}}{\partial x_{dv}} + \psi_{\mathcal{S}}^T \frac{\partial \mathcal{S}}{\partial x_{dv}} \tag{2.11}$$

2.6 Mission analysis

The mission analysis in this work is done using pyMission [92]. This tool uses a direct transcription approach with enforcement of the governing equations at collocation points. B-splines are used to interpolate the velocity and altitude between a series of control points. pyMission offers optimization capabilities; however, that functionality is not used in this work. Rather, altitude and Mach number profiles are prescribed, and pyMission is used for analysis of the aircraft performance through an integration of an aircraft's fuel burn. A surrogate model for aircraft performance with respect to flight condition is used within pyMission to avoid too large a number

of high-fidelity function calls during the mission analysis.

2.7 Optimization algorithm

The optimization algorithm used throughout this work is SNOPT (Sparse Nonlinear OPTimizer) [93]. SNOPT is based on the sequential quadratic programming (SQP) optimization technique, with a quasi-Newton approximation of the Hessian of the Lagrangian. It is capable of handling the large number of design variables used in the optimization problems in this thesis and requires a comparatively small number of iterations, which is important given the computational requirements of high-fidelity coupled aerostructural analysis. The solvers and other computational tools are linked to SNOPT using pyOpt [94], a Python interface which provides access to a number of optimization algorithms, including IPOPT [95], SLSQP [96], CONMIN [97], NOMAD [98, 99], GCMMA [100], ALPSO [101], and NSGA2 [102].

CHAPTER 3

The need for high-fidelity simulation in aircraft design

One of the notable aspects of this work is the high-fidelity of the aerodynamic and structural models used within the optimizations. Implicit in the use of these high-fidelity models is the assumption that the improved model accuracy is worth the increased computational time required for analysis. A substantial amount of aircraft optimization research has been conducted using lower fidelity models [52, 53, 103, 104], which can often effectively identify first order effects. High-fidelity models are required to accurately predict the effectiveness of technologies like morphing trailing edges, particularly in the transonic regime. In order to show this need for high-fidelity, we consider a wing aerodynamically optimized using both Euler and RANS CFD aerodynamic models. Before considering the results of those optimizations, the next section first defines and discusses the baseline geometries used throughout this work, which are all based on the NASA Common Research Model (CRM) [105].

3.1 Common Research Model

The baseline geometry used for the aerodynamic analyses and optimizations throughout this work is the CRM. The configuration was designed as a benchmark for valida-

tion and CFD verification. It has since been adapted by many researchers, including those in the Aerodynamic Design Optimization Discussion Group (ADODG). Various configurations with just the wing, the wing and body, and the wing-body-tail are used for different studies. The configuration approximates a Boeing 777-200ER, and provides a thoroughly studied baseline from which to start our work. The wing-body-tail CRM configuration is shown in Figure 3.1. The nominal flight condition for the CRM is at $M = 0.85$ and $C_L = 0.5$.

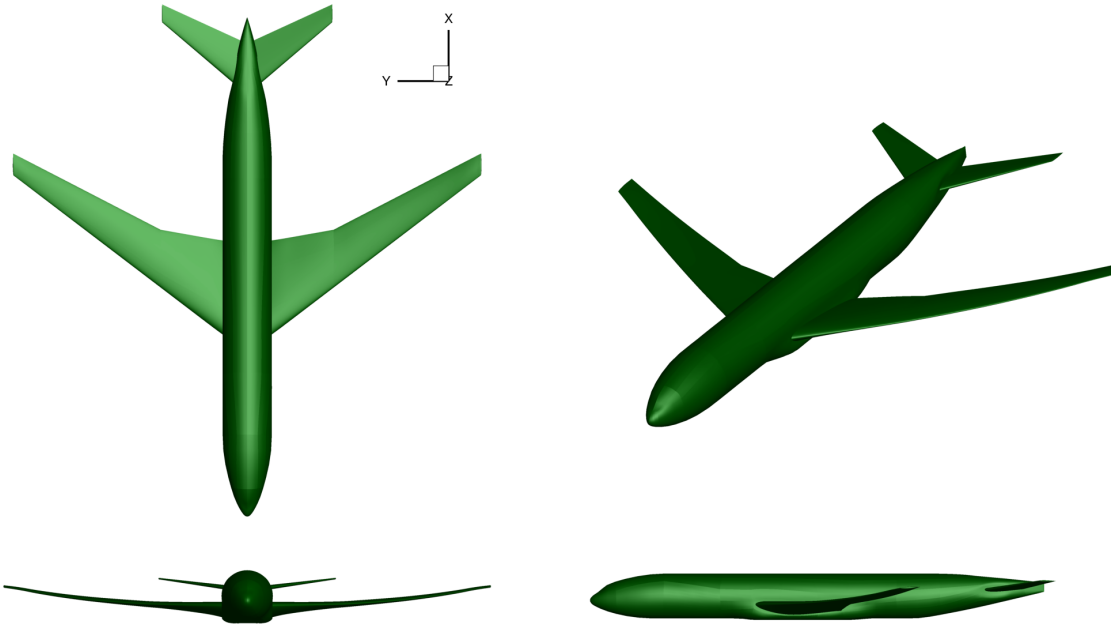

Figure 3.1: The CRM configuration is used as a starting point for our aerodynamic studies.

The grids used for the aerodynamic analyses and optimization throughout this work have been previously tested and verified [106, 107]. For completeness, grid refinement information from those studies is included in Tables 3.1 and 3.2. Note the grid size conventions introduced here and used throughout this work. Within a grid family, the various refinements are labeled as various grid levels. As the grid level increases (for example from 0 to 1, or from 1 to 2), the mesh undergoes a uniform coarsening. As such, the mesh size is reduced by a factor of 8.

Mesh level	Mesh size	C_D	C_L	C_M	α [deg]
h=0	∞	0.01990			
L00	230 686 720	0.01992	0.50000	-0.17760	2.2199
L0	28 835 840	0.01997	0.50000	-0.17900	2.2100
L1	3 604 480	0.02017	0.50000	-0.01810	2.1837
L2	450 560	0.02111	0.50000	-0.01822	2.1944

Table 3.1: CRM wing only convergence study completed by Lyu [106]

Mesh level	Mesh size	C_D	y^+	C_L	C_{M_y}
h=0	∞	0.026581			
L0	47 751 168	0.027353	0.996	0.50000	-0.0386
L1	5 968 896	0.029068	2.711	0.50000	-0.0411
L2	746 112	0.035227	5.244	0.50000	-0.0508

Table 3.2: CRM wing-body-tail convergence study completed by Chen *et al.* [107]

3.1.1 Undeflected Common Research Model

The CRM was developed for use in aerodynamic benchmark problems. As such, it is designed to represent the deflected aerodynamic shape at the nominal flight condition, and does not include any internal structural members. To perform coupled aerostructural analysis and optimization, a model of the undeflected jig shape of the wing is required. This model is defined by the undeflected Common Research Model (uCRM) [108]. The wingbox of the uCRM was developed based on that of a Boeing 777. The jig shape was determined using an iterative inverse design procedure minimizing the L^2 norm of the geometric differences between the CRM and the uCRM at the nominal flight condition. The difference in drag between the CRM and uCRM at the nominal flight condition is less than one count. The uCRM is used as the starting point for the aerostructural optimizations throughout this work. Additional details about the uCRM configuration can be found in Table 3.3 and the configuration, including the rib and spar locations, is shown in Figure 3.2.

Parameter	Value	Units
Span	58.8	m
Aspect ratio	9.0	-
Reference wing area	383.7	m^2
Reference chord	7.005	m
Moment reference (x)	33.68	m
Moment reference (z)	4.52	m
Leading edge sweep	37.4	deg
Maximum takeoff weight (MTOW)	297 500	kg
Maximum landing weight (MLW)	213 180	kg
Maximum zero fuel weight (MZFW)	195 040	kg
Operational Empty Weight	138 100	kg
Range	7 725	nm
Payload	34 000	kg
Reserve fuel	15 000	kg
Wing weight	30 286	kg
Fixed weight	107 814	kg
Thrust specific fuel consumption (TSFC)	0.53	$lb/(lbf \cdot h)$

Table 3.3: Summary of baseline uCRM parameters based on the uCRM development [108] and publicly available Boeing 777-200ER data [109].

3.1.2 High aspect ratio undeflected Common Research Model

The last study in Chapter 5 considers a high-aspect ratio variation of the uCRM, the uCRM-13.5. As materials science and composite design continue to improve, higher aspect ratios will become possible. This configuration was designed to begin studies on such configurations. To generate this variant, the planform of the original uCRM was stretched, while maintaining a constant wing area, until the aspect ratio was increased to 13.5. This stretched wing performed very poorly, so an initial multi-point optimization was performed to improve the design. This optimization included buffet constraints, and closely resembles that described by Kenway *et al.* [110]. The uCRM-13.5 configuration is shown in Figure 3.3.

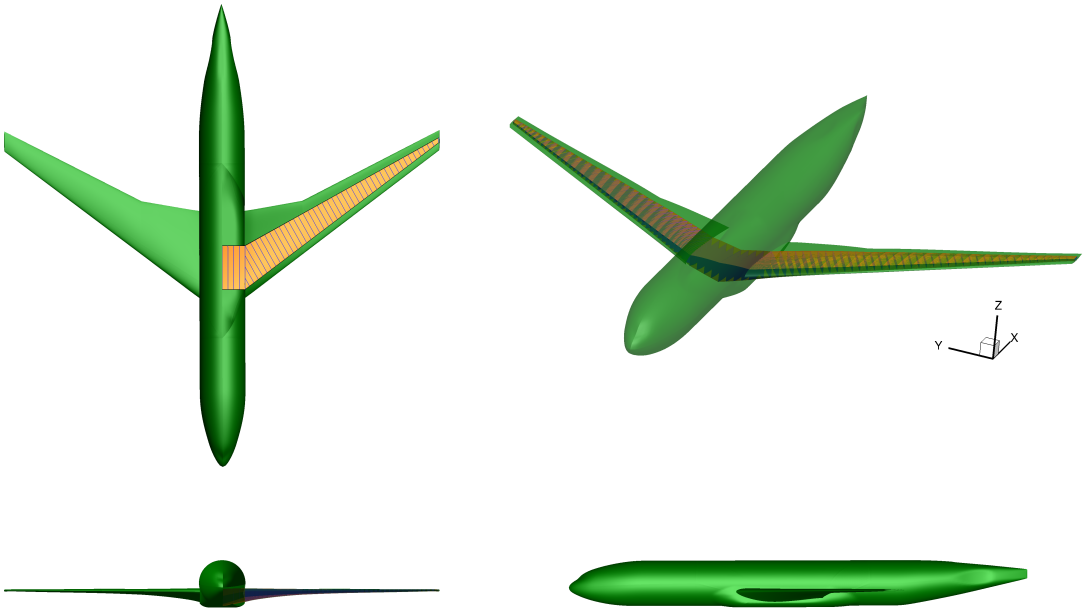

Figure 3.2: The uCRM configuration is used as a starting point for our aerostructural studies.

3.2 Comparison of Euler and RANS aerodynamic analysis

In order to demonstrate the need for high-fidelity analysis in aerodynamic and aerostructural aircraft wing design, we consider two aerodynamic optimizations of the CRM, using different fidelity aerodynamic models. The wings optimized using the RANS and Euler governing equations are then compared.

3.2.1 Problem definition

The baseline geometry for these optimizations is the wing of the CRM configuration, as shown in Figure 3.1. A second geometry was produced with a slight alteration at the trailing edge. The baseline CRM geometry has a dull trailing edge representative of what is realistically manufacturable; however, a sharp trailing edge is required for convergence with the Euler analysis. The Free Form Deformation (FFD) used in the optimizations has 15 spanwise control points and 24 chordwise control points, as

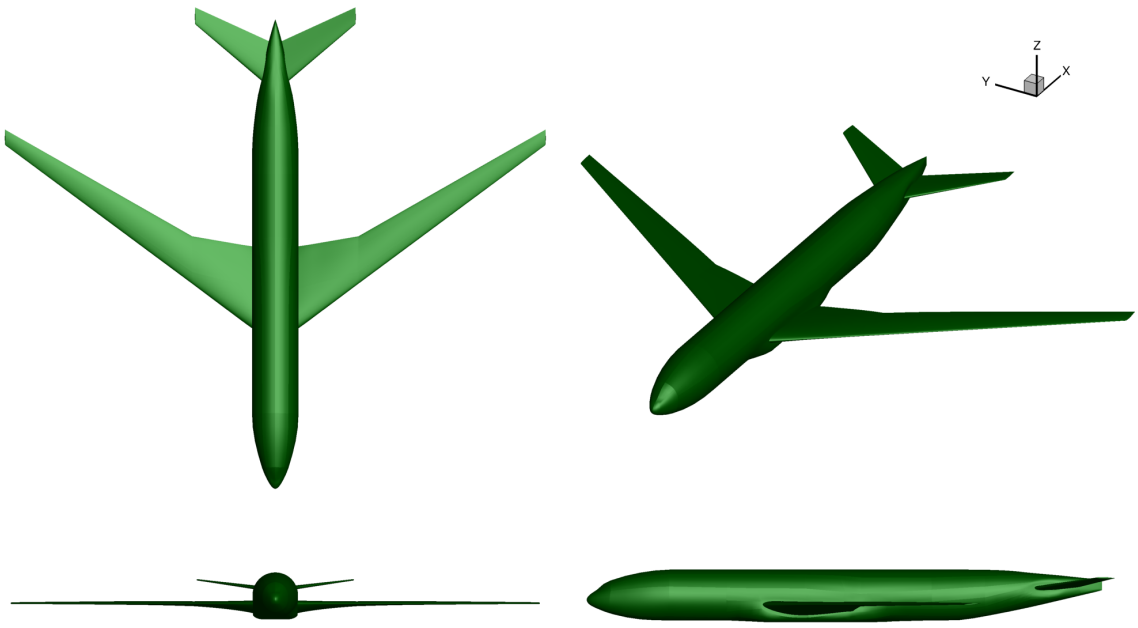

Figure 3.3: The uCRM-13.5 configuration is used as a starting point for the aerostructural studies of high aspect ratio configurations in Chapter 5.

shown in Figure 3.4.

The optimizations are formulated as lift constrained drag minimizations. Except for the aerodynamic governing equations, the two optimizations are identical. The optimization problem formulation is summarized in Table 3.4. Each of the control points is free to move in the z-direction, which preserves the planform, but allows for local shape changes. The angle of attack (AoA) is also a design variable. While previous results have shown that including twist as a design variable is generally a best practice, that is not done here, as this problem was based largely on a benchmark case put forward by the Aerodynamic Design Optimization Discussion Group (ADODG). Instead of a pure rotational twist, this problem formulation generates a shear twist, as evidenced by the set of leading and trailing edge constraints. At the trailing edge, control points above and below the wing have to move in equal and opposite directions, thus preserving the location of the trailing edge. This is not the case on the

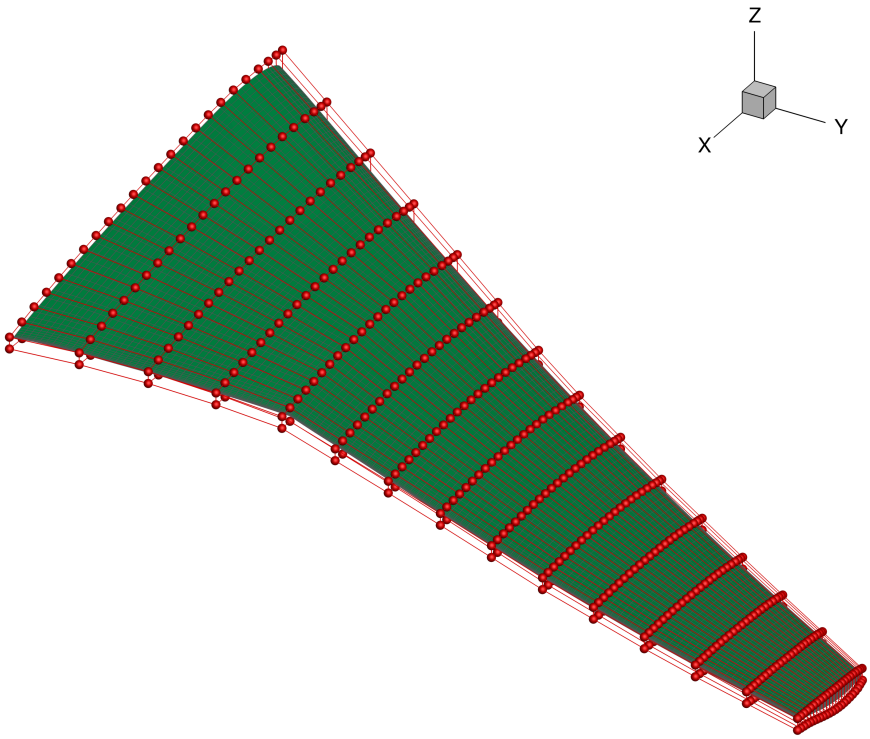

Figure 3.4: The FFD used for the Euler and RANS optimizations has a total of 720 ($24 \times 15 \times 2$) control points, shown in red.

leading edge. At the root, the same type of constraint is applied, but the rest of the leading edge is free to move vertically, thus allowing shearing twist. Other geometric constraints prevent the overall volume of the wing from decreasing, to assure sufficient space for fuel, and prevent any local thicknesses from reducing beyond 25% of their initial value. Additional constraints include a lift constraint ($C_L = 0.5$) and a pitching moment constraint ($C_{M_y} \geq -0.17$).

3.2.2 Euler optimized wing

Optimizing the problem defined in the previous section using Euler analysis produced the wing shown on the right side of Figure 3.5 . On the left side of the figure is the baseline CRM wing, solved for a lift coefficient of 0.5. This format, and a num-

	Function/variable	Description	Quantity
minimize	C_D		
w.r.t.	x_{α_c}	Cruise AoA	1
	x_{shape}	Wing shape (FFD)	720
		Total DVs	**721**
subject to	$C_L = C_L*$	Lift coefficient	1
	$C_{M_y} \geq -0.17$	Pitching moment	1
	${}^{V}/_{V_i} \geq 1$	Fuel volume	1
	${}^{t}/_{t_i}\|_{\text{LE}} \geq 0.25$	thickness	750
	$\Delta z_{\text{LE}_u} = -\Delta z_{\text{LE}_l}$	Fixed leading edge root	1
	$\Delta z_{\text{TE}_u} = -\Delta z_{\text{TE}_l}$	Fixed trailing edge	15
		Total constraints	**769**

Table 3.4: Overview of the aerodynamic shape optimization performed with both Euler and RANS analysis.

ber of variations thereof, are used throughout this thesis to visualize and compare aerodynamic and aerostructural optimization results. As this is the first of these comparisons, we now briefly consider each component of the figure. In the upper left are two contour plots of the pressure coefficient superimposed over the wings' planforms. The wing on the left is the baseline CRM, while the wing on the right shows the results after the optimization, as shown in the green and blue labels. The labels also show a few key metrics for the two wings being compared (C_D, C_L, and C_M in this case). Note also that the blue and green coloration refers to the appropriate wing in the other components of the figure as well.

Under the planform view is a front view of the wing. This view shows a visualization of the shock surface, shown in orange here. For aerostructural results this view can additionally compare structural deformations at various conditions. Below the front view are a number of plots showing various spanwise distributions. In this figure are (from top to bottom) the normalized lift distribution, the twist distribution, and the thickness distribution, normalized by the chord. Note that the spanwise coordinate of these plots matches that of the front view above them. On the right

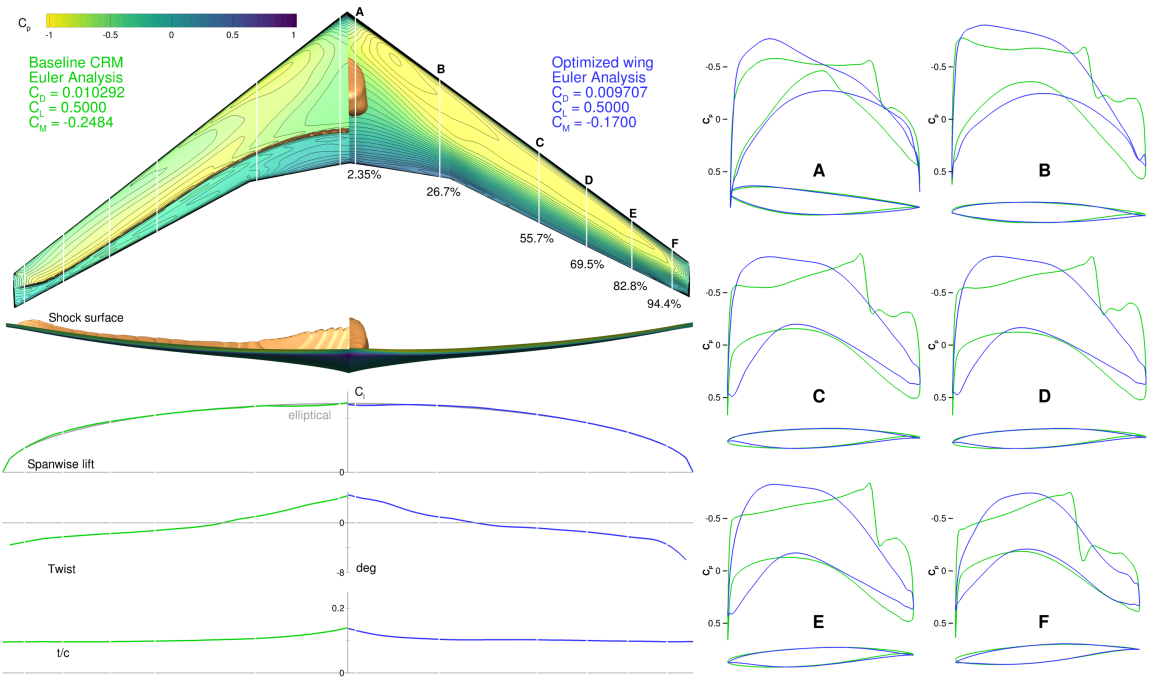

Figure 3.5: Using Euler analysis, an aerodynamic optimization of the CRM wing produces a reduction of 5.85 drag counts.

side of the figure are six plots showing pressure distributions and airfoil profiles at various spanwise locations. The spanwise locations of these slices are labeled with a white line and a letter (A-E) on the left side of the plot. The selection of the slice locations in this case was based on specifications in a similar ADODG benchmark optimization problem.

While at this point we have not discussed in detail the optimization methods used to generate the optimized shape, the results of the optimization alone are sufficient for motivating the use of high-fidelity models. More details on the solvers and optimization methods are given in Chapter 2. Looking at the results of the Euler optimization of the CRM, we can see that the optimized wing shows a drag reduction of 5.85 counts. While the baseline CRM had a shock across nearly the entire span of the wing, the shape optimization removed most of the shock. This can be seen in the pressure contours and in the front view of the wing. The results additionally show a more elliptical lift distribution, which produces a lower induced drag. This design

optimized for performance with an Euler model will be used as a reference for the comparisons made later in this chapter.

3.2.3 RANS optimized wing

We repeated the aerodynamic optimization detailed in Table 3.4, this time with RANS rather than Euler analysis. The results of this optimization are shown in Figure 3.6.

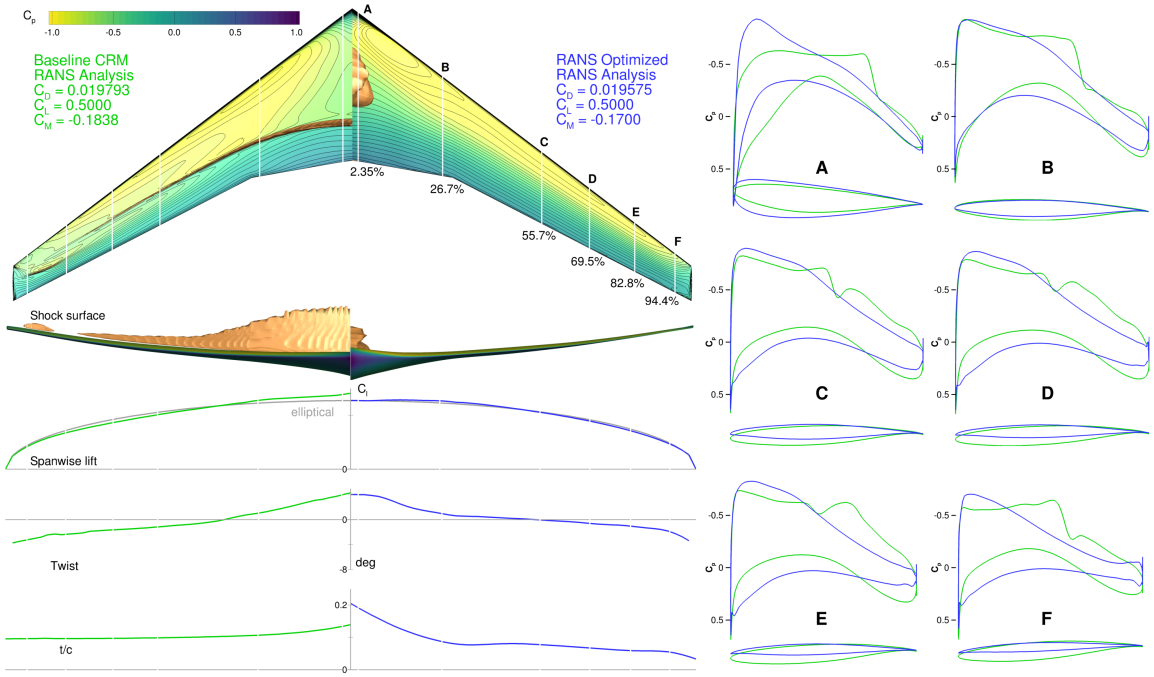

Figure 3.6: Using RANS analysis, an aerodynamic optimization of the CRM wing produces a reduction of 2.18 drag counts.

Starting from the baseline CRM, the RANS optimization produced a wing with a drag value 2.18 counts lower. That reduction represents a 1.11% reduction in drag for the CRM wing. While this drag reduction is less substantial than that seen in the Euler case, many similar traits are seen in this optimization. Again, the wing started with a shock spanning most of the wing, which the optimizer was largely able to remove. The spanwise lift distribution is also again shifted closer to elliptical. Something new in this optimization result is the inboard shift of the wing thickness for

improved viscous drag. At first glance, this is the most visible difference between the two optimized designs. To get a meaningful comparison of the two designs however, they need to be compared closely and from a common perspective. As such, we now consider the performance of the optimized wings in both the inviscid Euler model and the viscous RANS model.

3.2.4 Comparison of the optimized wings

With optimized shapes of the wings based on each of the analysis techniques, analyses are conducted to determine how the wings perform when analyzed with the alternative method. That is, the RANS equations are used to analyze the wing optimized with the Euler equations, and vice versa. This yields a measure of the effectiveness of the lower fidelity Euler analysis method for optimization. If the lower fidelity Euler-based optimization produces a wing that performs relatively well when analyzed with the RANS equations, there may not be a need to perform the more costly higher-fidelity analysis within optimizations. If the wing produced with the low-fidelity optimization does not perform well under higher fidelity analysis, the optimization requires at least some consideration of the high-fidelity model in its analysis loop.

Before considering the wing analysis, note that this example demonstrates one of the important benefits of using the FFD approach for geometry parameterization, as outlined in Section 2.1. Again, the FFD parameterized the changes in the shape, rather than the shape itself, which enables this comparison. As the geometry at the trailing edge needs to be different for the two types of analysis, using an approach that parameterizes the geometry itself would prove difficult. Using FFDs, the appropriate initial geometry (with a blunt or sharp trailing edge) is simply implanted and then the control point deformations from each optimization are applied.

Next, consider the optimized wings analyzed using the Euler equations, as shown

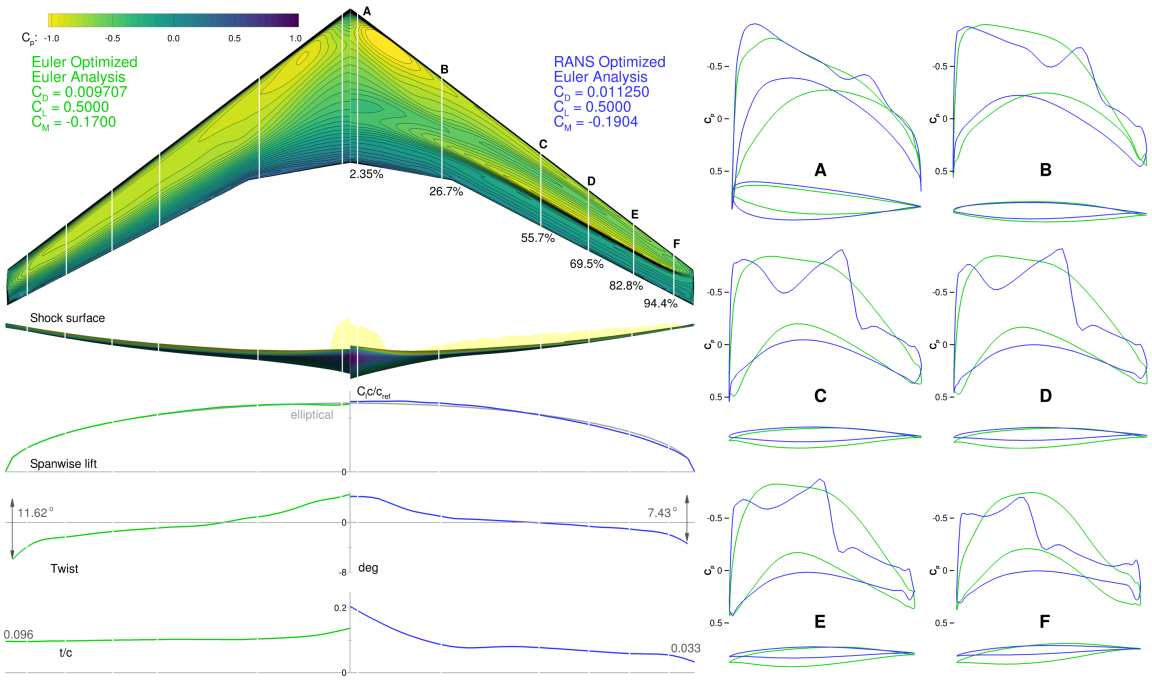

Figure 3.7: Euler analysis of the wing optimized using RANS based analysis shows very poor performance, including a substantial shock spanning the majority of the wing.

in Figure 3.7. The results for the wing optimized with Euler analysis are exactly the same as those results at the end of the optimization. The wing optimized with RANS was run with a variable angle of attack until the lift coefficient matched the 0.5 value constrained in the original optimization formulation. This equal lift coefficient value allows for meaningful comparison of the two results. Looking at the drag coefficients of the two wings, the wing optimized with RANS has about 15.9% more drag. The pitching moment produced by the two wings is quite different, and that the RANS optimized wing now violates the pitching moment constraint. From these high level wing metrics alone, it is apparent that the two optimization approaches designed drastically different wings. These results seem to suggest that there are substantial differences in the optimization problems; however, it is not enough for the low-fidelity wing to outperform the high-fidelity wing when analyzed with low-fidelity. The more meaningful test is a comparison of the two wings when analyzed with the high-fidelity

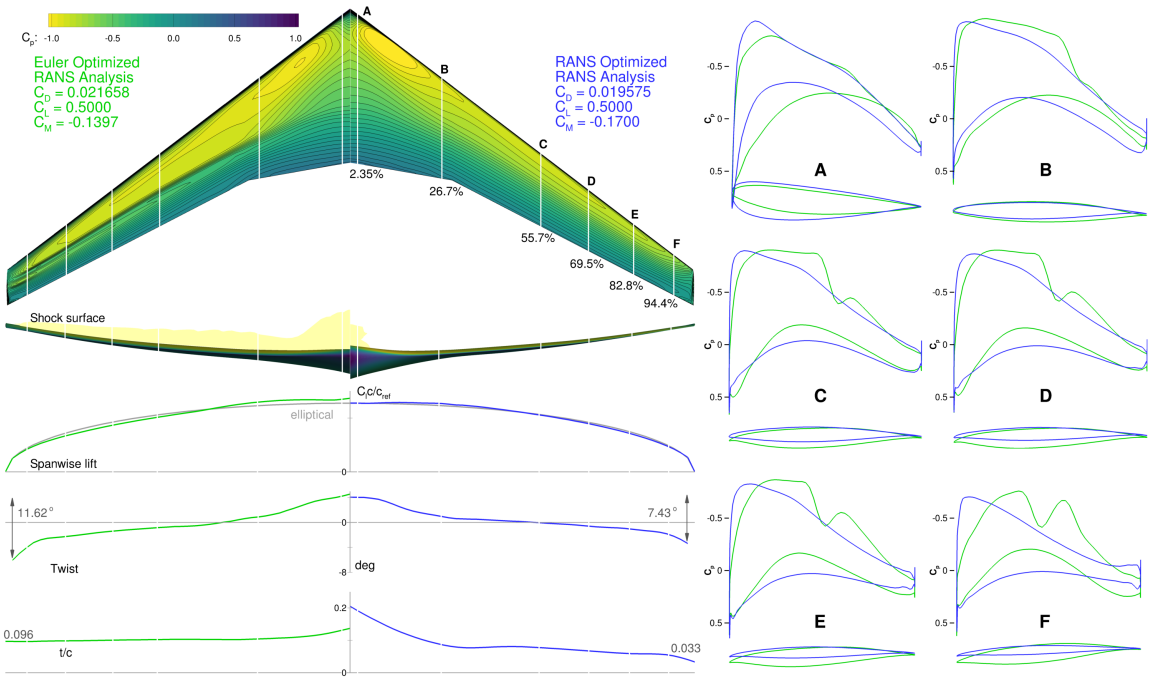

Figure 3.8: RANS analysis of the wing optimized with the Euler equations shows a large shock and poor performance, demonstrating the importance of RANS based analysis in the optimization loop.

RANS equations. As such, the next comparison shows the differences in the two wing designs in more detail within that context.

Consider the RANS analysis of the optimized wing shapes, shown in Figure 3.8. As was the case with the Euler analysis, we can see a substantial discrepancy in the drag and moment coefficients of the two wings. The wing optimized with RANS produces a lift distribution much closer to elliptical and shows much less washout near the tip of the wing. The RANS-optimized wing shifted a large amount of the wing volume inboard to reduce viscous drag, while the Euler-optimized wing maintained a nearly constant thickness to chord ratio. The Euler optimized wing also produces a number of shocks across a large portion of the wing, seen in the front view of the wing and in the pressure contours. These shocks contribute a substantial amount of wave drag. Lyu *et al.* [56] conducted a similar comparison with an ONERA M6 wing; however, the wings were compared at a lower Mach number ($M = 0.8395$) and lift

coefficient ($C_L = 0.271$). In his comparison he observed differences in the optimized shape similar to those seen herein, but the difference in performance was much less substantial. This difference can be directly attributed to the flight conditions at which the designs were optimized and compared. This result suggests that as the lift coefficient and Mach number are increased, the drag becomes increasingly dependent on small shape changes. This result will be observed again in Chapter 6.

3.3 Summary

The performance of the Euler-optimized and RANS-optimized wings when analyzed with the RANS equations demonstrate that low-fidelity Euler analysis alone in the optimization loop is insufficient for transonic wing design. Performing such low-fidelity optimizations produces designs substantially different than analogous optimizations with higher fidelity models. The inclusion of viscous forces has a drastic influence on the design of the wing, and ignoring those forces produces a wing with markedly worse performance, particularly in the transonic regime where small, localized shape changes have large impacts on a wing's wave drag. This result demonstrates the importance of using high-fidelity models for transonic wing design, and validates the use of those more expensive, higher fidelity models in the remainder of this work. As an additional note, this result does not suggest that lower fidelity models are not useful for optimization, but rather that lower fidelity models *alone* are not sufficient for transonic wing optimization. Multi-fidelity approaches have the potential to provide the accurate optimized shape produced with the high-fidelity optimizations here, at a reduced computational cost; however, those approaches are still under development and were not used in this work.

CHAPTER 4

Singlepoint aerostructural optimization

This chapter presents my initial aerostructural optimization comparison between a wing with and without a morphing trailing edge: a singlepoint optimization with one maneuver condition used to size the structure. The qualifier singlepoint is used here to specify that there is one cruise condition at which the aerodynamic performance is measured and used for fuel burn calculations. Multipoint, on the other hand, indicates that multiple conditions are considered in the calculation of the cruise fuel burn. Multipoint optimizations are presented in later chapters. While these optimizations are called singlepoint in reference to the single cruise point, they also include analysis at a maneuver condition. This maneuver condition is required to appropriately size the structure of the wing. As such, singlepoint optimizations still utilized morphing trailing edge capabilities. The optimizations in this section serve as the initial high-fidelity comparisons of aircraft performance with and without a morphing trailing edge.

4.1 Problem formulation

In this chapter, there are three optimization problems. The first problem is a baseline aerostructrual optimization. This baseline optimization does not include any morphing variables and represents the baseline from which the results with mor-

phing are measured. It is important that the reference for comparison be an optimized configuration rather than the initial geometry. If the initial geometry was used as a reference, any improvements resulting from correcting the non-optimized features of the initial geometry would be indistinguishable from the improvements resulting from the morphing. By performing an initial baseline optimization, we are able to generate a reference from which improvements produced by morphing can be isolated. The baseline optimization problem is summarized in Table 4.1, and a more detailed description of the objective function, design variables, and constraints of the optimization problem follow.

The second and third optimization problems define two morphing cases. The first morphing case is a wing retrofit with a morphing trailing edge device. The second morphing case is a complete clean sheet redesign of the wing, including morphing technology from the start. In Section 4.2, these morphing optimization problems will be described in terms of their differences from the baseline optimization problem.

4.1.1 Objective function

The objective function for the aerostructural optimizations outlined below is a weighted average of the fuel burn and the takeoff gross weight (TOGW). These two objectives correlate closely with the aircraft's operating costs and acquisition costs, respectively. Different airlines prefer various compromises between these two costs, and writing the objective as this weighted sum allows the development of Pareto fronts representing the compromise between the two objectives [81]. The general objective function is written as:

$$f(x) = \beta \text{ FB} + (1 - \beta) \text{ TOGW} \tag{4.1}$$

where FB is the fuel burn, and $\beta \in [0, 1]$ is the trade-off variable, defining how the two objectives are weighted.

In these optimizations, a trade-off value of 1 was used, making fuel burn the

	Function/variable	Description	Quantity
minimize	Fuel burn		
w.r.t.	x_{α_c}	Cruise AoA	1
	x_{α_m}	Maneuver AoA	1
	x_shape	Wing shape (FFD)	192
	x_twist	Wing twist	8
	x_struct	Structural sizing	884
		Total DVs	**1086**
subject to	$L = n_i W$	Lift	2
	${}^{V}/_{V_\mathrm{i}} \geq 1$	Fuel volume	1
	${}^{t}/_{t_\mathrm{i}}\vert_\mathrm{LE} \geq 1$	Leading edge thickness	20
	${}^{t}/_{t_\mathrm{i}}\vert_\mathrm{TE} \geq 1$	Trailing edge thickness	50
	${}^{t}/_{t_\mathrm{i}}\vert_\mathrm{spar} \geq 1$	Aft spar thickness	20
	$\Delta z_{\mathrm{LE}_\mathrm{u}} = -\Delta z_{\mathrm{LE}_\mathrm{l}}$	Fixed leading edge	8
	$\Delta z_{\mathrm{TE}_\mathrm{u}} = -\Delta z_{\mathrm{TE}_\mathrm{l}}$	Fixed trailing edge	8
	$L_\mathrm{panel} - x_\mathrm{panel} = 0$	Panel consistency	302
	$KS_\mathrm{stress} \leq 1$	Maneuver stress	3
	$KS_\mathrm{buckling} \leq 1$	Maneuver buckling	3
	$\vert x_{\mathrm{str}_i} - x_{\mathrm{str}_{i+1}}\vert \leq 0.0005$	Adjacency	696
		Total constraints	**1113**

Table 4.1: Overview of the baseline uCRM aerostructural optimization problem.

objective function. The fuel burn for taxi, takeoff, climb, and descent are ignored for simplicity. This allows us to estimate the fuel consumption over the cruise portion of the mission—the portion which uses the majority of the fuel for a long range mission—by applying the Breguet range equation to the design range:

$$\text{FB} = \text{LGW}\left(\exp\left(\frac{R\ \text{TSFC}}{V\frac{L}{D}}\right) - 1\right), \tag{4.2}$$

where LGW is the landing gross weight, R is the design range, TSFC is the thrust specific fuel consumption, V is the cruise speed, and $\frac{L}{D}$ is the lift-to-drag ratio. The lift-to-drag ratio is computed using the trim-corrected lift and drag coefficients, with an additional 50 counts of drag added to account for the unmodeled losses, like those from the vertical stabilizer, nacelles, and pylons.

4.1.2 Design variables

The entire list of design variables is given in Table 4.1. These design variables can be split into three sets: aerodynamic, geometric, and structural variables. The only aerodynamic design variables are the angles of attack at each flight condition, which are added to assure that a lift constraint can be added without making the problem ill-posed. Eight twist variables and the movements of 192 control points in the z-direction prescribe geometric shape changes. The control points are not given freedom in the x and y directions, meaning that the planform of the wing is held fixed. To achieve configuration-specific morphing, a subset of the control points is added a second time as design variables. These 80 control points, all of which are on the aft 40% of the wing, behind the wing box, are associated only with a specific configuration and are not applied to the FFD during the analysis of alternate configurations. The subset of control points associated with the morphing trailing edge are shown in blue in Figure 4.1.

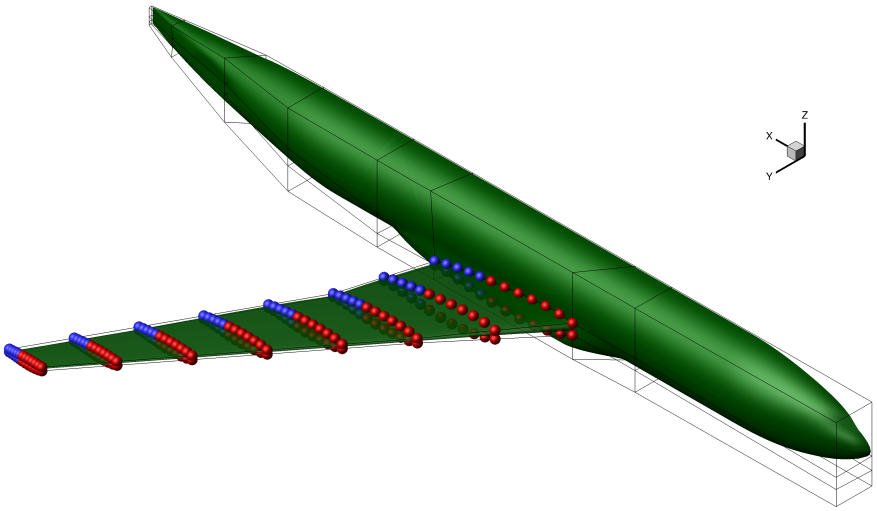

Figure 4.1: Each sphere represents one of the 192 FFD control points. The blue spheres are the subset of control points associated with the morphing trailing edge.

Structural design variables are used to parametrize the geometry of the wingbox. Note that in these analyses, the full wingbox, including the center section spanning the fuselage, is considered. This means that the structural deflection at the wing-fuselage interface is not necessarily zero. Large interface deflections result in mesh tears, but the optimization permits small deformations. A smeared stiffness panel approach is used in the analysis of the structural deformations [111]. The geometry of the stiffened panels is shown in Figure 4.2. To simplify the model and reduce the number of design variables, we take $w_b = h_s$ and $t_b = t_w$. This yields four design variables for the skins and spars in each bay of the wingbox: panel thickness, panel length, stiffener thickness, and stiffener height. The panel length is included as a structural design variable to simplify buckling calculations, and is constrained to be consistent with the geometric design variables through a series of constraints. Four additional design variables are used to define the pitch of the stiffeners on the skins and spars. Note that the stiffener pitch is taken as constant on each of these components. All together, this yields 884 structural design variables.

In summary, there are 884 structural variables, an angle of attack, 8 twist variables,

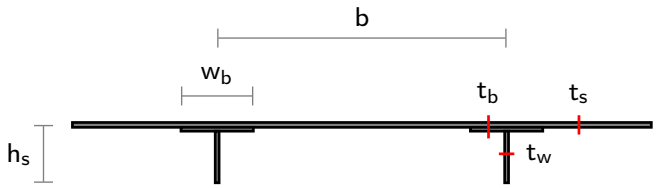

Figure 4.2: The structural design variables parametrize the geometry as has been done in past work [108].

192 shape variables spanning the entire wing, and 80 morphing shape variables on the aft 40% of the wing. To assure the problem is well-posed, given that there are lift, stress, and buckling constraints as discussed in Section 4.1.3, the structural and aerodynamic design variables are included in each of the optimizations. The selection of design variables defines the different optimizations discussed below. For the retrofitted wing, the only geometric design variables available to the optimizer are those representing the morphing trailing edge. Note that this adds 80 design variables for each of the flight configurations, allowing the wing to have alternate morphed shapes for cruise and maneuver. As such, there are 160 geometric design variables used in the retrofitted optimization. In the clean sheet design, 280 geometric variables are used. The 8 twist and 192 full wing shape variables are applied at each flight condition, and at the off design maneuver condition, one set of 80 morphing variables is used in conjunction with the full wing shape variables.

4.1.3 Constraints

To ensure that the optimization results represent a physically feasible system, a number of constraints are added to the problem. The optimizations below consider flight at two conditions: cruise and maneuver. The first constraints ensure steady flight at these two conditions, as the lift is set equal to the weight times the load factor. A 2.5 g load factor is used at maneuver. More detailed data on the two flight conditions is listed in Table 4.2

Parameter	Cruise	Maneuver
Load factor	1.0	2.5
Mach number	0.85	0.64
Altitude (ft.)	37 000	0
Weight	$\frac{1}{2}$(TOGW + LGW)	TOGW

Table 4.2: Overview of the cruise and maneuver flight conditions.

The first geometric constraint prevents the wing volume from decreasing, assuring that there is sufficient space in the wing for fuel. Geometric constraints prevent airfoil thickness reductions in a number of locations. The leading edge thickness is constrained to prevent the optimizer from designing sharp leading edges, which perform poorly at low speeds. The trailing edge thickness is constrained to maintain a manufacturable trailing edge. Finally, the thickness at the aft spar of the wingbox is constrained not to decrease, to assure there is sufficient space for control surface actuators. Constraints are added to the leading and trailing edges at cruise to prevent shearing twist. These constraints require that the control points along the front and back faces of the FFD move in equal and opposite directions, such that the center of the FFD faces won't be moved by shape changes. The structural constraints are used to prevent failure, maintain consistency, and again prevent unrealistic designs. Adjacency constraints prevent unreasonable changes in the skins and stiffeners between neighboring panels. Nonlinear consistency constraints are used to constrain panel lengths to match the length prescribed by the FFD, as discussed in Section 4.1.2. Finally, to ensure that the structure does not fail, buckling and stress constraints are enforced for the 2.5 g maneuver case. These constraints are aggregated into 6 KS constraints.

4.1.4 Trim Correction

In these analyses, we consider the wing and fuselage configuration without a tail. As such, a correction needs to be applied to account for the changes in the lift and

drag as a result of trimming the aircraft. A surrogate model was used to approximate the effects of the tail, as proposed and validated by Chen *et al.* [107]. To build this surrogate, Chen performed a lift coefficient constrained sweep of the tail twist angle variable on the baseline full configuration CRM. Specifically, a series of tail twist angles were prescribed, and the angle of attack was adjusted to set the lift coefficient to 0.5. The components of the lift, drag, and pitching moment were then decomposed, so that the effect of the tail in each condition could be isolated and used to construct a model for trim drag. It should be noted that this surrogate was produced using the aerodynamic-only CRM model, meaning that structural deflections were not considered.

The model consists of 1-D B-spline interpolations for the lift and drag coefficients, both with respect to the pitching moment required from the tail. Then,

$$C_L = C_{L_{wb}} + C_{L_t}, \tag{4.3}$$

and

$$C_D = C_{D_{wb}} + C_{D_t}, \tag{4.4}$$

where C_L and C_D are the approximate trimmed full configuration cruise lift and drag coefficients, $C_{L_{wb}}$ and $C_{D_{wb}}$ are the computed lift and drag coefficients on the wing-body configuration, and C_{L_t} and C_{D_t} are the lift and drag coefficient contributions produced by the horizontal tail. In this way, we account for the negative lift and positive drag produced by the trimming tail. The surrogate functions for $C_{D_t}(C_{M_y})$ and $C_{L_t}(C_{M_y})$ are shown in Figure 4.3.

While this trim penalty model does not predict the lift and drag produced by the tail exactly, there is a close agreement between results produced with this method and results found with a full wing-body-tail optimization [107]. The correction was applied only at cruise, as the maneuver drag is not as important.

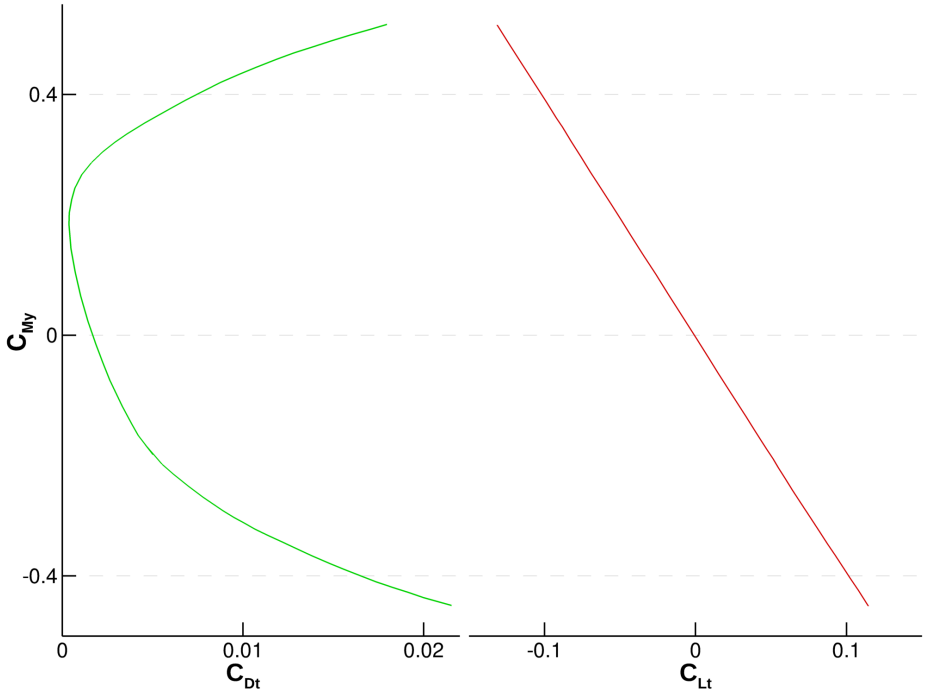

Figure 4.3: The trimming surrogate used in these optimizations defines the lift and drag coefficient contribution produced by the tail at a specified trimming moment.

4.2 Results

In this section, we quantify the fuel burn benefit resulting from a morphing trailing edge. We do so by comparing an optimized wing without a morphing trailing edge to a wing retrofitted with a morphing TE and a wing that was completely redesigned with a morphing TE.

4.2.1 Optimization of the retrofit trailing edge

In our first study, we consider the benefits associated with retrofitting a morphing trailing edge device onto an existing wing. To do this, we compare the aerostructural performance of the optimized uCRM to that of the uCRM enhanced with design variables in the morphing section of the wing. This optimization varies from the baseline optimization in the following ways:

- The 192 full wing FFD control points are not used

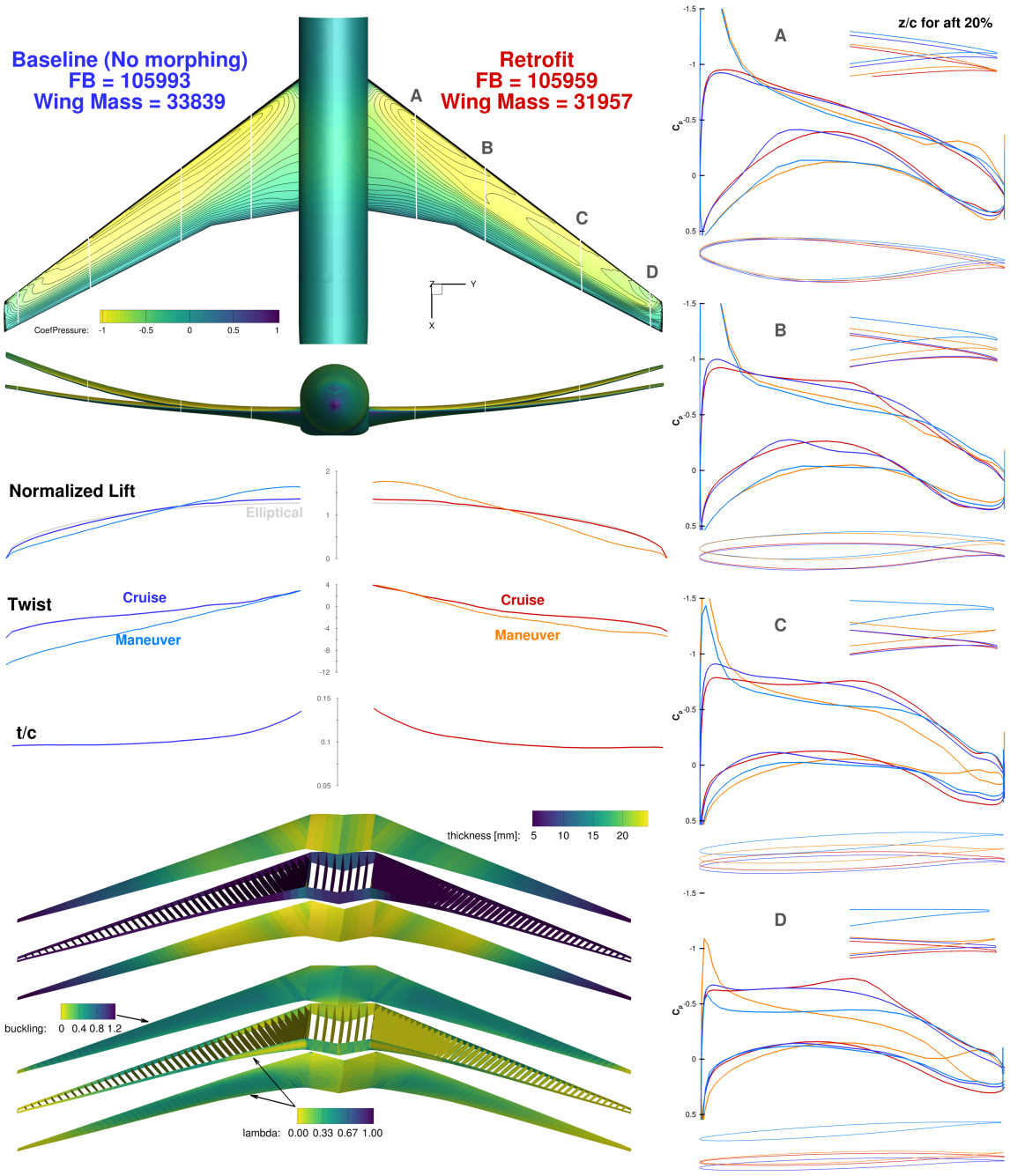

Figure 4.4: A comparison of a baseline aerostructural optimization of the uCRM to an optimization of the baseline uCRM retrofitted with a morphing trailing edge. The morphing TE produced an airfoil with reversed camber at the outboard sections during maneuver, helping to shift the loads inboard.

- 80 control points are added to control the morphing section, both at cruise and maneuver (adding 160 design variables total). These morphing control points are shown as blue spheres in Figure 4.1.
- The 8 twist design variables are not included
- The fixed trailing edge constraint is removed

A comparison of the resulting wing shapes is shown in Figure 4.4. When comparing the two cases, we see that the objective fuel burn values are nearly equal, varying by only 0.032%. Interestingly, the baseline uCRM produces a fuel burn of 112,491 kg, which means that both optimizations were able to reduce the fuel burn by approximately 5.8%. Looking at the pressure coefficient contours of the two wings at cruise, we see that the baseline optimization produces nearly parallel pressure contours, while the retrofit can produce such parallel contours only on the aft section of the wing. This feature of the pressure contours matches expectations, as the retrofit wing does not have shape control of the front portion of the wing. Interestingly, the retrofit wing is still able to achieve the same level of fuel burn reduction, due largely to its wing mass reduction. The reduction in the wing mass is achieved through load alleviation at the maneuver condition, which allows the structural member thicknesses to be decreased. The lift distributions of the two cases show a more substantial inboard shift of loading achieved in the retrofit case. Correspondingly, from the front view, it is clear that the wing deflection at maneuver is reduced through the use of the morphing TE.

Further insights about the outboard load alleviation achieved by the morphing can be found by considering the slice information on the right of Figure 4.4. At sections C and D, we see that the morphing has reversed the airfoil's camber near the TE for the maneuver case. Correspondingly, the chordwise pressure distributions show a region of negative lift is produced towards the trailing edge tip. Interest-

ingly, this effect also contributes to a change in the twist distribution between the two cases at maneuver. In the baseline case, passive load alleviation results from structural washout, as evidenced by the twist distribution. The twist distribution for the retrofit wing at maneuver is much closer to that at cruise. This result illustrates the difference in the two methods of load alleviation: passive load alleviation via aeroelastic tailoring to produce washout at maneuver, and active load alleviation via airfoil morphing, producing negative camber regions near the tip of the wing. As a final interesting note, the thickness distributions for the two cases is very similar. The retrofit wing is slightly thicker near the root and thinner near the tip, but this difference is much smaller than the other differences between the two configurations, suggesting the addition of the morphing trailing edge has little effect on the ideal thickness distribution.

4.2.2 Clean sheet design

We now consider the benefits of the morphing trailing edge on a clean sheet design, and again compare to an optimized wing without morphing. The only difference between the baseline optimization and the optimization of the clean sheet design is the addition of 80 morphing design variables at the maneuver case. The comparison between the two results is shown in Figure 4.5.

The fuel burn for the clean sheet design is 0.36% lower than that of the baseline, non-morphing optimized design. This improvement is slightly more than that of the retrofit wing. The cruise pressure coefficient contours show the advantage of having control of shape design variables which encompass the entire wing. The contours of the baseline and clean sheet wings at cruise are nearly identical, and both match what is expected for an optimized wing at its design condition. The lift distribution at cruise shows that the clean sheet design is able to match an elliptical distribution more closely than the baseline case. Given that the only difference between the two cases

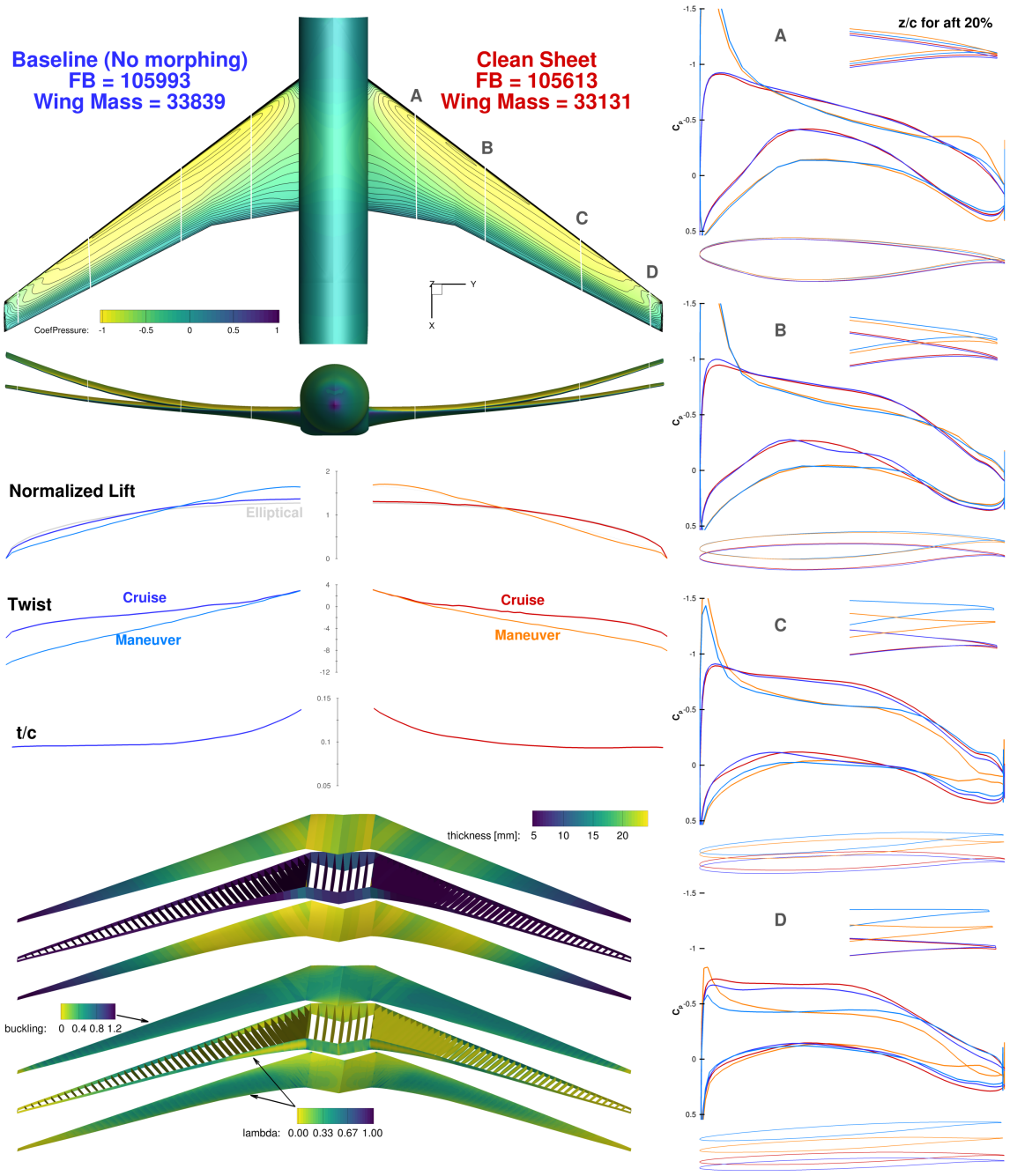

Figure 4.5: A comparison of a baseline aerostructural optimization of the uCRM to an analogous optimization of a clean sheet wing design with a morphing trailing edge. The morphing trailing edge is able to reduce the lift produced on the outboard section, shifting loads inboard at maneuver to alleviate stresses on the wingbox.

is the inclusion of morphing variables at maneuver, it follows that this improvement in the cruise performance is a result of the decrease in coupling between the cruise and maneuver configurations. The inclusion of morphing at maneuver removes the need to trade off between cruise performance and maneuver feasibility, but in the baseline optimization, consideration of performance at maneuver can compromise cruise performance, giving lift distributions slightly different than the elliptic ideal. The twist and thickness distributions show similar trends to those from the retrofit design, although the clean sheet maneuver twist does not follow the cruise twist as closely as in the retrofit case.

The structural thickness distribution shows the thicknesses of the structural members to be much closer than they were in the comparison of the baseline to the retrofit wing. This result is consistent with the wing mass comparison as well. Looking at the lift distribution of the clean sheet design at maneuver, we again see that it has achieved more load alleviation than the baseline optimization; however, there is not as much load alleviation as was present in the retrofit wing. The airfoil and pressure coefficient slices suggest a similar conclusion, as the clean sheet design also reversed the camber of the outboard airfoils, but did so to a much lower extent than the retrofit wing. The region of negative lift is confined to a smaller area near the trailing edge tip. This is interesting, given that the clean sheet design used the same set of morphing control points as the retrofit case. To better understand what is happening in these optimizations, we consider what physical means the optimizer uses to reduce fuel burn in each case.

From these results, we conclude that the morphing trailing edge optimization comes up with two ways to reduce the fuel burn. First, improved load alleviation at maneuver shifts the critical loads further inboard, resulting in a lower structural weight. The second method involves the weakening of the coupling between performance at various flight conditions. The coupling is not completely removed, but the

adaptability of the morphing trailing edge at off-design conditions allows the design at each condition to focus more on its own objectives, with less influence from the other flight conditions. This means that there are fewer compromises and trade-offs needed at each flight condition, which yields better performance. In the retrofit design, the aerodynamic improvements available at the cruise conditions were limited, as the twist distribution and much of the airfoil shape could not be changed, so the optimizer focused on improving the fuel burn through the first method. This is apparent as the wing mass is significantly decreased in the retrofit case. Both methods are used in the clean sheet design, as the cruise lift distribution more closely follows the ideal distribution, and the maneuver distribution is shifted further inboard than that of the non-morphing wing. The clean sheet wing mass is less than that of the baseline optimized wing, but is greater than that from the retrofit design. The relative wing masses in the clean sheet and retrofit designs demonstrate the difference in the balance between the two fuel burn reduction methods for the two optimizations.

4.3 Summary

In this chapter, we performed the design optimization of a standard non-morphing wing, a wing retrofitted with a morphing trailing edge, and a clean sheet wing designed with the morphing trailing edge. A summary of the optimization results is given in Table 4.3.

Optimization	**Fuel burn [kg]**	**Δ Fuel burn [%]**	**Wing mass [kg]**
Baseline	105,993	-5.776	33,839
Retrofit	105,959	-5.807	31,957
Clean Sheet	105,613	-6.114	33,131

Table 4.3: Comparison of the fuel burn and wing mass of the three singlepoint optimized wing designs. Percentage fuel burn reductions are measured from the 112,491 kg produced by the unoptimized uCRM configuration.

Compared to the starting point of the optimizations, the baseline optimized wing

reduced the fuel burn by 5.78%. Nearly the same level of fuel burn reduction was achieved in the retrofit optimization, where the optimizer had no control over the twist distribution or the shape variables on the front 60% of the wing. This result very clearly demonstrates the value of active load alleviation via a morphing trailing edge. Starting from a wing that had the potential for at least a 5.78% efficiency improvement, a retrofit design of an active morphing trailing edge device provided as much benefit as a complete redesign of the wing without morphing.

The clean sheet optimized wing reduced the fuel burn by 6.11% compared to the uCRM starting configuration. The morphing trailing edge achieved fuel burn reductions via two mechanisms. The first was based on the ability to improve maneuver load alleviation, allowing for lighter wing structures. The second was a reduction of the coupling between the cruise and maneuver cases, which allows the cruise configuration to improve without causing adverse effects on maneuver performance. The clean sheet design used both of these mechanisms, while the retrofit design focused on reducing the weight of the wing, as the increases it could make at cruise were limited by its design space.

These results show that a morphing trailing edge has the potential to decrease the fuel burn, but the improvements with respect to an aerostructurally optimized standard wing are rather marginal. This is due largely to the problem formulation. Given the geometric constraints and the set of two flight conditions, only one of which was concerned with the aerodynamic performance (in terms of L/D), the potential savings from using a morphing trailing edge were limited. One of the motivating attributes of morphing technology is its ability to increase a wing's robustness by improving the aircraft's performance at a wide variety of flight conditions. Performing singlepoint optimization restricts the potential gains from this advantage. Without morphing, aeroelastic tailoring alone is effective in designing a wing for singlepoint performance. To capture the benefits of morphing technology more effectively, we

consider multipoint optimization in the next chapter.

CHAPTER 5

Multipoint aerostructural optimization

The work in the previous chapter compared an optimized wing without morphing to a wing retrofit with a morphing device and a wing completely redesigned with a morphing trailing edge. These comparisons were completed using singlepoint aerostructural design optimization. The benefits produced by the morphing technology in these optimizations were limited by the problem formulation. To take advantage of the added versatility and robustness that the morphing trailing edge device offers, the work in this chapter considers a number of multipoint optimizations.

5.1 Problem formulation

The initial configuration for the baseline optimizations is the uCRM. As was done in the singlepoint case, the initial wing is first optimized without any morphing capabilities, to provide a fair reference from which to measure the improvements provided in subsequent optimizations. Those subsequent optimizations include morphing capabilities. Comparing the fuel burn of the optimized aircraft with and without the morphing design variables, we isolate and quantify the effects of the morphing trailing edge.

In the optimizations of the morphing wing, morphing design variables are included at all of the non-nominal flight conditions. The "baseline" or non-morphed

wing shape is defined using design variables over the entire FFD at the nominal flight condition. Since that set of design variables defines the baseline shape of the wing, adding redundant variables in the morphing region is both unnecessary and inadvisable. Adding redundant morphing variables at the nominal cruise conditions produces an ill-posed optimization problem. Redundant design variables are, in general, unfavorable in optimization problems, as they produce an infinite number of optimal solutions produced with linear combinations of redundant variables.

We consider two multipoint stencils: a 3-point stencil with varying lift coefficient and a 7-point stencil with varying lift coefficient, Mach number, and altitude. A variety of previous work [82, 112, 113] has investigated the importance of multipoint stencil selection. In general, there is a substantial difference between optimized singlepoint and multipoint results, even for a small multipoint stencil. Adding more points to the multipoint stencil typically produces diminishing returns in terms of the additional improvement in the optimized result for a standard non-morphing wing. Given the active adaptability of a morphing wing, the performance dependence on the stencil selection is less clear. Performing the 7-point optimization will help to better understand this relationship.

The multipoint stencils are detailed in Tables 5.1 and 5.2 below. The Mach number and C_L ranges used in the stencil have been used in previous work, and span a large portion of the typical flight regime. The altitude variations in the 7-point stencil are selected to correspond to full and empty aircraft weights. The stencils are selected to produce a wide variety of flight conditions so that they can effectively demonstrate the benefits of the morphing trailing edge capability.

The nominal flight condition for the uCRM is at a Mach number of 0.85 and a lift coefficient (C_L) of 0.5. The multipoint stencils are centered around this nominal flight condition. The Breguet range equation is again used to approximate the fuel burn of each configuration in the multipoint stencil. The average of the fuel burn at each

Flight condition	Mach	C_L	Altitude (ft)
Nominal	0.85	0.50	34,000
Low C_L	0.85	0.45	34,000
High C_L	0.85	0.55	34,000

Table 5.1: Overview of the 3-point stencil of cruise flight conditions. These three conditions are aligned vertically in Figure 5.2.

of the conditions is the objective function of the optimization. Maneuver conditions at 2.5 and $-1.0\,\mathrm{g}$ are considered to appropriately size the members of the wingbox. Note that when compared to the cases in the previous chapter, this optimization problem considers two more cruise conditions *and* one more maneuver condition. This additional maneuver condition helps size the lower skin more appropriately, and increase the benefit produced by the morphing trailing edge device. Stress and buckling constraints are added for both maneuver conditions [76].

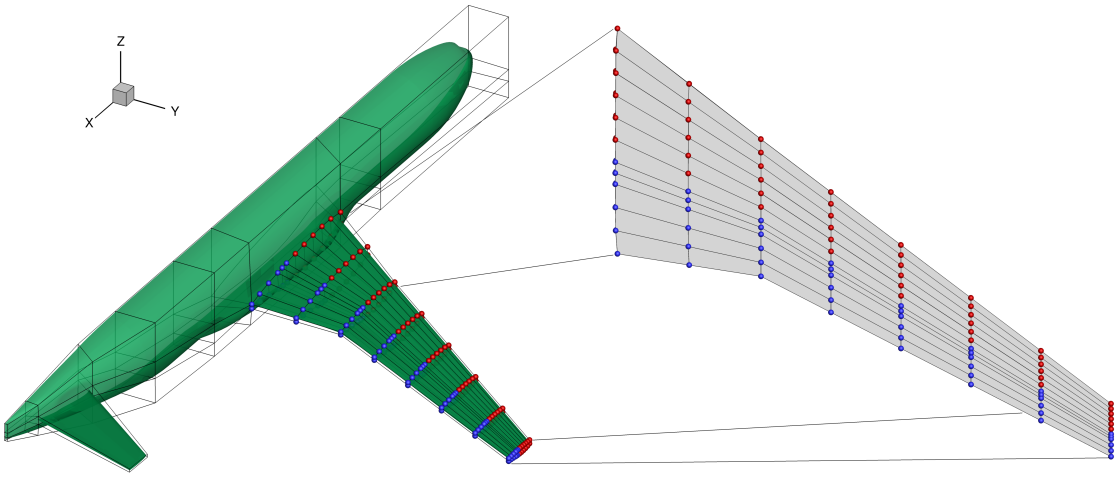

Figure 5.1: The FFD used for the multipoint optimizations. Note that while the blue control points represent the region where morphing is constrained, the two forward most points at each spanwise slice are not free to move as morphing variables.

The objective of each of the optimizations is to minimize the average fuel burn over each of the flight conditions in the multipoint stencil. To do this, the optimizer adjusts several design variables. These design variables can be found in Table 5.3 and

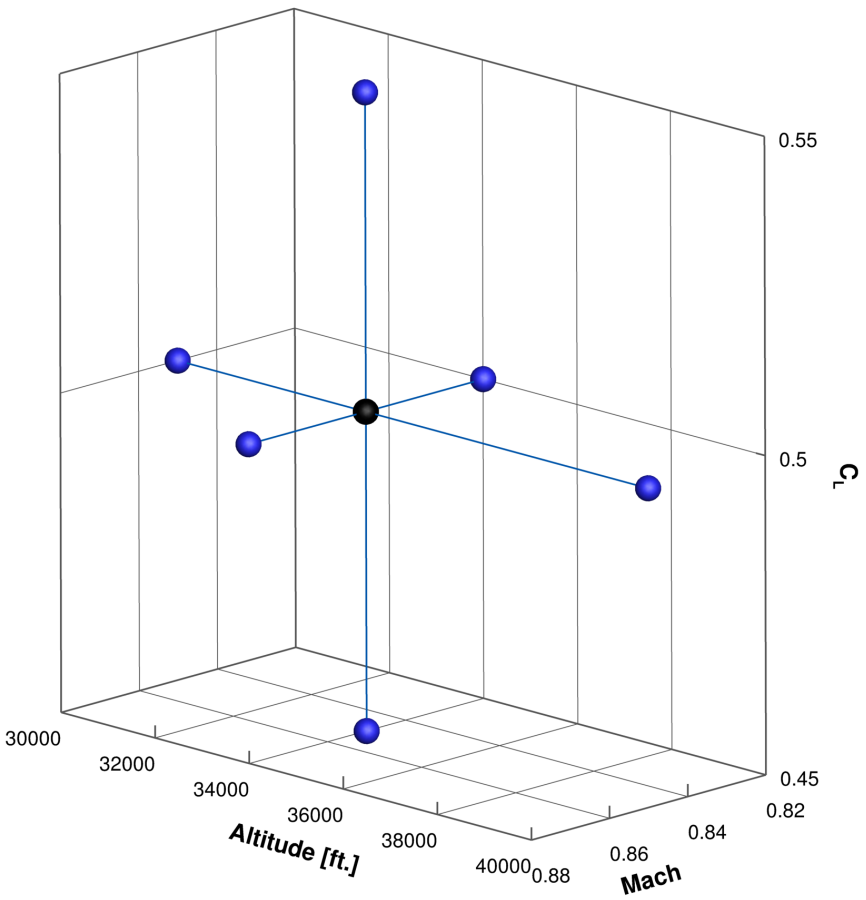

Figure 5.2: The 3-point stencil is a subset of the 7-point stencil shown here.

we will again consider aerodynamic variables first, followed by geometric variables, and ending with structural variables. The angle of attack can change at each flight condition (cruise and maneuver), so that each lift constraint is satisfied. The tail rotation angle is adjusted to trim the aircraft. The shape of the wing is controlled through adjustments of the FFD control points. There are 192 shape design variables, which define the non-morphed, nominal optimized wing shape. These variables are available in each of the four optimizations. They adjust the z-location of control points only, preserving the planform of the aircraft. The FFD used for these optimizations is shown in Figure 5.1.

A subset of 64 shape variables defines the morphing device. As such, 64 variables

Flight condition	**Mach**	C_L	**Altitude (ft)**
Nominal	0.85	0.50	34,000
Low C_L	0.85	0.45	34,000
High C_L	0.85	0.55	34,000
Low M	0.82	0.50	34,000
High M	0.88	0.50	34,000
Low alt.	0.85	0.50	30,000
High alt.	0.85	0.50	40,000

Table 5.2: Overview of the 7-point stencil of cruise flight conditions. This stencil is shown in Mach–Altitude–C_L space in Figure 5.2.

are added for each non-nominal flight condition. For the 3-point stencil, this results in 256 additional shape variables: 64 for each of the two additional cruise conditions and the two maneuver conditions. Note that in Figure 5.1, there are 48 visible blue morphing control points, suggesting a total of 96 including the corresponding control points on the bottom of the wing. In this problem, not all of the blue control points are assigned morphing design variables. Instead, the blue control points define the region within which the morphing deformations are contained. Given that the FFD control points have a region of influence spanning two control points in each (i,j,k) direction in the FFD, to limit the deformations within the convex hull formed by the blue control points, the 2 forward most control points at each spanwise location are not given freedom during morphing deformations. This shows how the 64 morphing control points are arranged for these optimizations, as $(4 \times 8 \times 2)$. Wing twist variables are also defined (as aggregate movements of control points) at eight spanwise locations, to give the optimizer more direct control of the twist distribution.

Shape changes are limited by a number of geometric constraints, which can be found in Table 5.3. The volume of the wing is constrained not to decrease, ensuring sufficient space for fuel. At 20 spanwise locations, the leading edge and trailing edge thicknesses are constrained not to decrease, to provide low speed performance and manufacturability, respectively. Additional thickness constraints provide room

	Function/variable	Description	3C	3M	7C	7M
minimize	Fuel burn					
w.r.t.	x_{α_c}	Cruise AoA	3	3	7	7
	x_{α_m}	Maneuver AoA	2	2	2	2
	x_{shape}	Wing shape (FFD)	192	192	192	192
	x_{morph}	Morphing shape (FFD)	0	256	0	512
	x_{twist}	Wing twist	8	8	8	8
	x_{tail}	Tail rotation angle	5	5	9	9
	x_{struct}	Structural sizing	854	854	854	854
		Total DVs	**1064**	**1320**	**1072**	**1584**
subject to	$L = n_i W$	Lift	5	5	9	9
	$M = 0$	Pitching moment	5	5	9	9
	$V/V_{\text{init}} \geq 1$	Fuel volume	1	1	1	1
	$t/t_{\text{init}}\|_{\text{LE}} \geq 1$	Leading edge thickness	20	20	20	20
	$t/t_{\text{init}}\|_{\text{TE}} \geq 1$	Trailing edge thickness	20	20	20	20
	$t/t_{\text{init}}\|_{\text{spar}} \geq 1$	Morphing thickness	20	220	20	220
	$\Delta z_{\text{LE}_u} = -\Delta z_{\text{LE}_l}$	Fixed leading edge	8	8	8	8
	$\Delta z_{\text{TE}_u} = -\Delta z_{\text{TE}_l}$	Fixed trailing edge	8	0	8	0
	$L_{\text{panel}} - x_{\text{panel}} = 0$	Panel consistency	272	272	272	272
	$\text{KS}_{\text{stress}} \leq 1$	Maneuver stress	3	3	3	3
	$\text{KS}_{\text{buckling}} \leq 1$	Maneuver buckling	6	6	6	6
	$\|x_{s_i} - x_{s_{i+1}}\| \leq 5\text{mm}$	Adjacency constraints	696	696	696	696
		Total constraints	**1064**	**1256**	**1072**	**1264**

Table 5.3: Overview of the 3-point conventional (**3C**), 3-point morphing (**3M**), 7-point conventional (**7C**), and 7-point morphing (**7M**) optimization problems.

for mounting actuation mechanisms to the aft spar, and limit shape changes in the morphing region. Shear twist is avoided by constraining the movements of the leading and trailing edge control points. Finally, 854 structural variables allow the optimizer to adjust thicknesses of spars, skins, ribs, and stiffeners. Length variables are also provided to the structural model, but they are constrained to be consistent with the geometric lengths through a series of nonlinear consistency constraints. The structure is constrained not to buckle at either maneuver condition, and is constrained not to fail at the 2.5 g pull up condition. These constraints are aggregated using KS functions, to limit the number of required adjoint solutions. Finally, 696 linear adjacency constraints ensure that thicknesses do not change by more than 5 mm between adjacent components of the structure. A summary of the four optimization problems is shown in Table 5.3.

5.2 Results

Having outlined the various optimization problems, we now describe the results of these optimizations. We start by considering the results for the conventional and morphing 3 point optimizations. After that we consider the analogous results from the 7 point optimization.

5.2.1 Three point optimization

Figure 5.3 shows a comparison of the optimized conventional wing and the optimized wing with morphing for the 3-point stencil. The addition of morphing had a clear positive effect on the performance of the wing, as the average fuel burn was reduced by 2.53%. This reduction is largely due to a substantial 22.4% reduction in structural weight. Looking at the pressure contours on the top of the wing for each of the cruise flight conditions, we see that in both optimizations there are few shocks and the pressure distribution is consistent with optimal transonic results with

a smooth pressure recovery [70].

On the front view of the aircraft, we see displaced wing shapes at the nominal cruise case as well as both maneuver conditions. We see that the addition of morphing at the maneuver conditions reduced the wing deflection at maneuver, which is consistent with the structural weight reduction we mentioned before. To see how this is achieved, we refer to the lift distribution below the front view of the aircraft. The distributions at the nominal cruise case and the 2.5 g maneuver overlay an elliptical lift distribution (in gray). The wing with morphing is able to shift more of the maneuver load inboard, reducing the root bending moment on the wing, which results in a much lighter structure.

Lower on Figure 5.3 we see the twist distributions, which show that the conventional wing washes out the tip using aeroelastic coupling at maneuver, while the wing with morphing produces a twist distribution more closely matching that at cruise. This is because adjustable camber handles the inboard shift of the load for the wing with morphing.

The thickness distribution of the structural members shows that the structure is thinner almost everywhere (where it is not limited by minimum gauge thickness) with the addition of morphing. The structural failure contours show that adding morphing allows the optimizer to push more structural members closer to their failure point, spreading the relatively localized stress and buckling concentrations seen in the conventional case.

Finally, considering the slices labeled A–D, we see further confirmation of the results discussed before, along with the mechanism by which the morphing achieves these results. Again, there are results for the nominal case and the 2.5 g maneuver case. Considering the pressure distributions on the slices, we see typical results for most cases, except the maneuver condition with morphing. For this case, the pressure distributions on the outboard section of the wing have inverted over the morphed

region. To see the cause of this, we consider the geometric slices. In the upper right corner of each plot is a zoomed-in view of the aft 20% of the airfoil. Here, we distinctly see the result of the morphing. At the maneuver condition, the morphing adds reverse camber on the outboard sections of the wing, producing the pressure distribution inversion and the inboard shift of the load distribution. This is the mechanism through which the wing with morphing reduces its structural weight, rather than relying solely on aeroelastic coupling like the conventional wing.

5.2.2 Seven point optimization

The results in this section consist of the same optimization applied to a 7-point stencil. Those optimization results are shown in Figure 5.4. Looking at the results, we see many of the same trends as for the 3-point optimization. Again, the addition of morphing led to a substantial fuel burn reduction, this time of over 5%, largely through the reduction of structural weight. As in the 3-point case, this reduction was enabled by the inboard shift of the maneuver load distribution resulting from the negative camber added to the outboard sections of the wing by the morphing. This mechanism for improving the aircraft's performance seems to be the same in the two morphing cases. However, we can gather a few more insights by examining the results in more detail.

Looking at the structural weights of the two wings optimized with morphing, we see that the optimal 7-point wing has a lighter structure. This is somewhat unexpected because the maneuver conditions and structural constraints used in both cases were the same. That is, both structures were sized so that the wing would not buckle or fail in either the 2.5 g pull up or the -1.0 g push over maneuvers. This discrepancy suggests that in the 7-point case, there is an increased incentive to reduce the structural weight. To understand why this is the case, we consider the objective function: the average fuel burn of the cruise conditions as estimated by

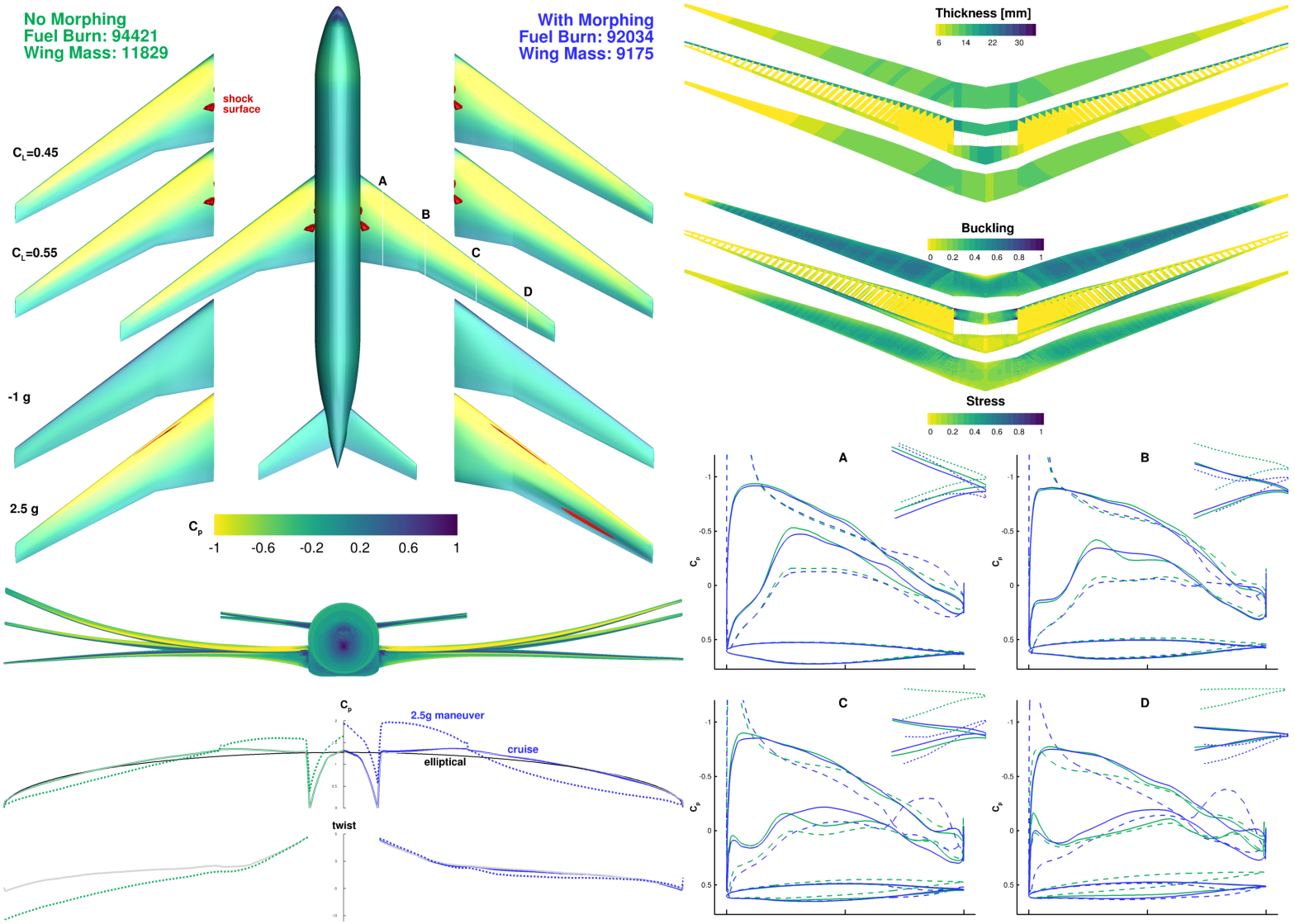

Figure 5.3: Adding morphing for the 3-point stencil reduced the fuel burn by 2.53%, and the structural weight was reduced by 22.4%.

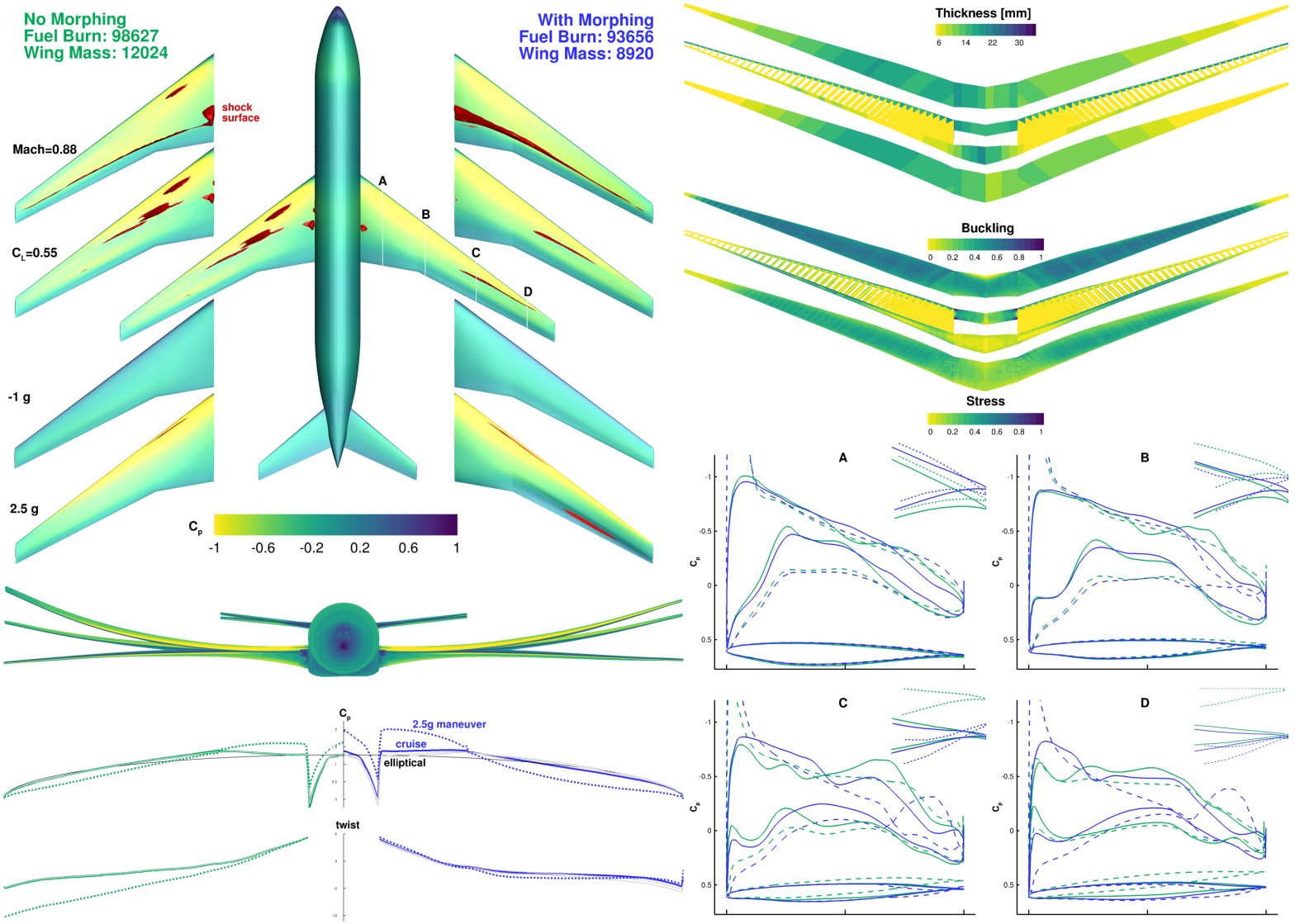

Figure 5.4: Adding morphing for the 7-point stencil reduced the fuel burn by 5.04%, and the structural weight was reduced by 25.8%.

the Breguet range equation (4.2). According to that equation, there are effectively two methods for reducing fuel burn: improving the aerodynamic performance at the cruise conditions (as given by the lift-to-drag ratio), and reducing the structural weight of the aircraft. These are the two mechanisms a morphing trailing edge can use to improve the aircraft's fuel burn, and thus improve the objective function of the optimizations. It is important to note that these two methods do not function independently. Instead, they are coupled, as reductions in structural weight often lead to reductions in cruise performance, which makes this trade-off difficult to handle without an effective optimizer.

We have already discussed the process by which morphing can reduce the structural weight. Morphing can also improve fuel burn through improvements to the aerodynamic performance at cruise. Without morphing, the wing shape is forced to compromise to achieve good performance at all of the flight conditions; however, the inclusion of morphing reduces the coupling between aerodynamic performance at various flight conditions. This was seen clearly in the previous chapter. This can also be seen in the solid-lined pressure contours at the nominal condition in Figure 5.4. For the conventional wing, the pressure contours show the waviness typical of multipoint aerodynamic or aerostructural optimization, highlighting the compromise made for optimal multipoint performance. After morphing is added, the contours become much smoother. While they are not as smooth as the analogous contours from the singlepoint cases of the previous chapter, they are much smoother than the conventional wing contours. This illustrates the weakening of the coupling between flight conditions that is enabled by morphing technology.

The optimization of a wing with morphing for minimum fuel burn is a balance between improving aerodynamic performance at cruise and reducing structural weight. While morphing helps to reduce the coupling between flight conditions, that coupling is *not* completely removed. The portion of the wing forward of the morphing is the

same for all flight conditions, and the thicknesses of the wingbox members cannot change in flight. Within this context, the lower structural weight for the 7-point result provides an interesting insight. With the addition of cruise flight conditions, the balance between improving aerodynamic performance and reducing structural weight shifted towards reducing the structural weight. Since there were no changes made to the constraints on the structure, this implies that the aerodynamic improvements available in the 7-point case are smaller than those available in the 3-point case. This conclusion makes sense, given the coupling between aerodynamic performance caused by the non-morphing section of the wing. Extrapolating this trend to consider aerodynamic performance for an aircraft's full set of flight conditions, the weight reductions available due to morphing become increasingly important. While morphing provides aerodynamic improvements through adaptability at a wide range of cruise conditions, its ability to substantially reduce structural weight through adaptive maneuver load alleviation yields a lighter structure, which reduces fuel burn at all flight conditions. This relationship is elaborated on in Chapter 6, where aerodynamic and aerostructural analysis are combined with full mission analysis.

5.2.3 30% morphing region

In this subsection, we discuss two additional optimizations, which resulted from reducing the size of the morphing device from the aft 40% of the chord to the aft 30%. The problem definition and setup for the 30% optimizations was similar to the previously discussed morphing optimization, except that the number of control points with morphing freedom was reduced by half, thus limiting the size of the morphing device. These optimizations were done to gain some insight into the significance the size of the morphing region has on the effectiveness of the morphing device. Figures 5.5 and 5.6 show comparisons between the uCRM wing optimized with a 30% and 40% morphing trailing edge for the 3-point and 7-point stencils, respectively. The

results for the 40% morphing device are the same as were shown in Figures 5.3 and 5.4. Looking at the results, the reduction of the morphing region produced small increases in both the wing mass and the fuel burn. As would be expected, with a smaller morphing device, the maneuver load alleviation was slightly less effective, resulting in the 2.78% heavier structure and 0.22% larger fuel burn. The general trends of the result match those for the 40% morphing device, again showing a lower structural weight for the 7-point case due to the previously detailed balance between reducing structural weight and improving cruise performance. While there is a reduction in savings for a smaller morphing device, the savings as compared to the wing without morphing are still sizable, showing that even if a morphing device is unable to extend all the way to the aft edge of the wingbox, it can still be an effective fuel burn reduction mechanism.

5.2.4 Morphing optimization of the uCRM-13.5

Given the results of the morphing optimizations of the uCRM discussed above, it follows that the fuel burn savings provided by morphing trailing edge technology should increase as the flexibility of the wing increases. As materials science and structural composite design continue to progress, the development of lighter and stronger next generation aircraft structures will enable the use of higher aspect ratio wings. In aerostructural optimization, there is a trade-off between the aerodynamic induced drag benefit and the structural penalty from increasing a wing's aspect ratio [79]. Decreasing the weight and/or increasing the strength of structural components shifts the balance in this trade-off, increasing the optimal aspect ratio. As such, we expect the current trend to continue, and for future aircraft wings to be more flexible and have higher aspect ratios. Given this likely trait of next generation aircraft wings, determining definitively the relationship between a wing's flexibility and the effectiveness of morphing technology is an important task. That is the objective of this

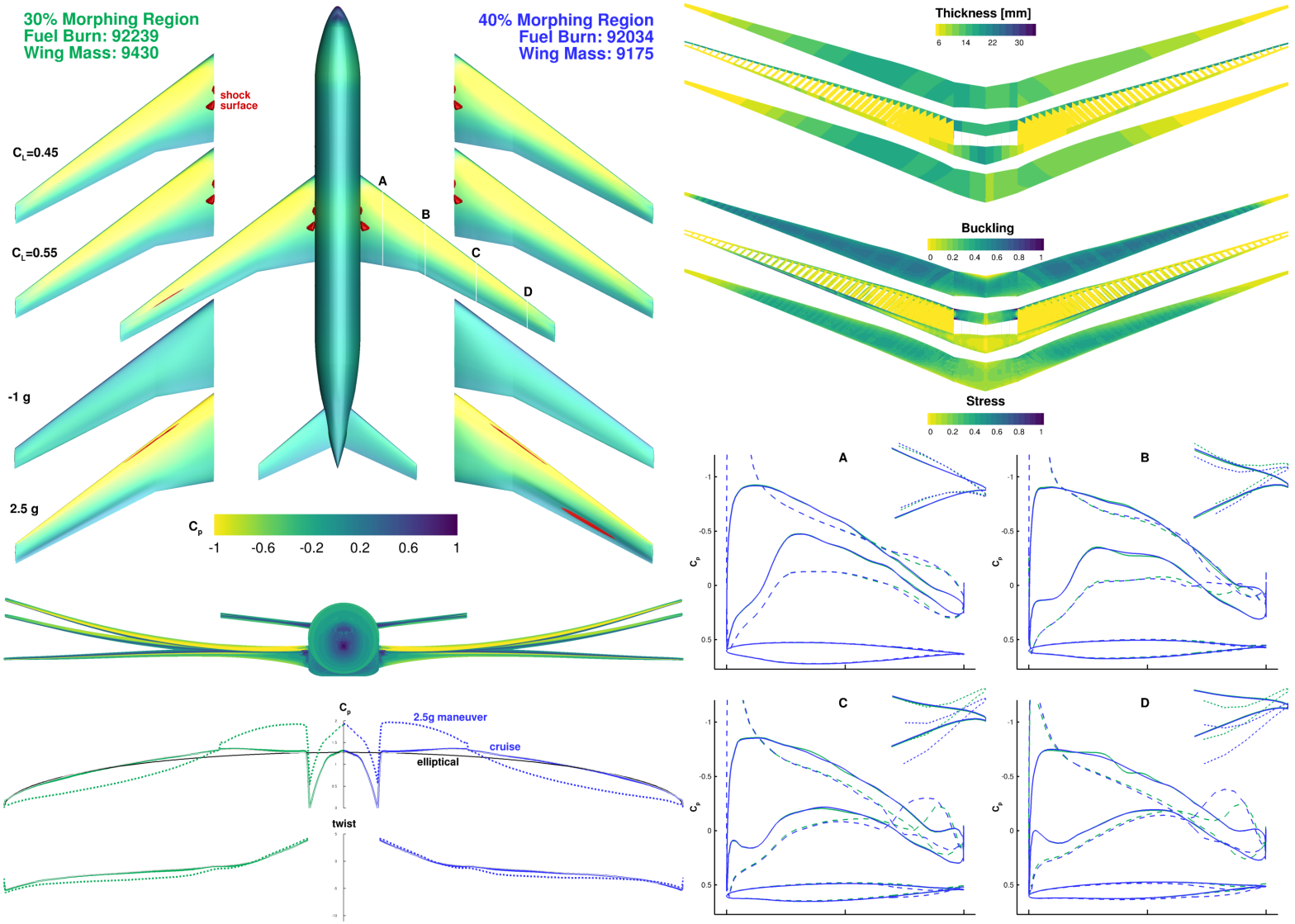

Figure 5.5: For the 3-point stencil when the morphing region was reduced from 40% to 30% of the chord, the fuel burn increased by 0.22% and the wing mass increased by 2.78%.

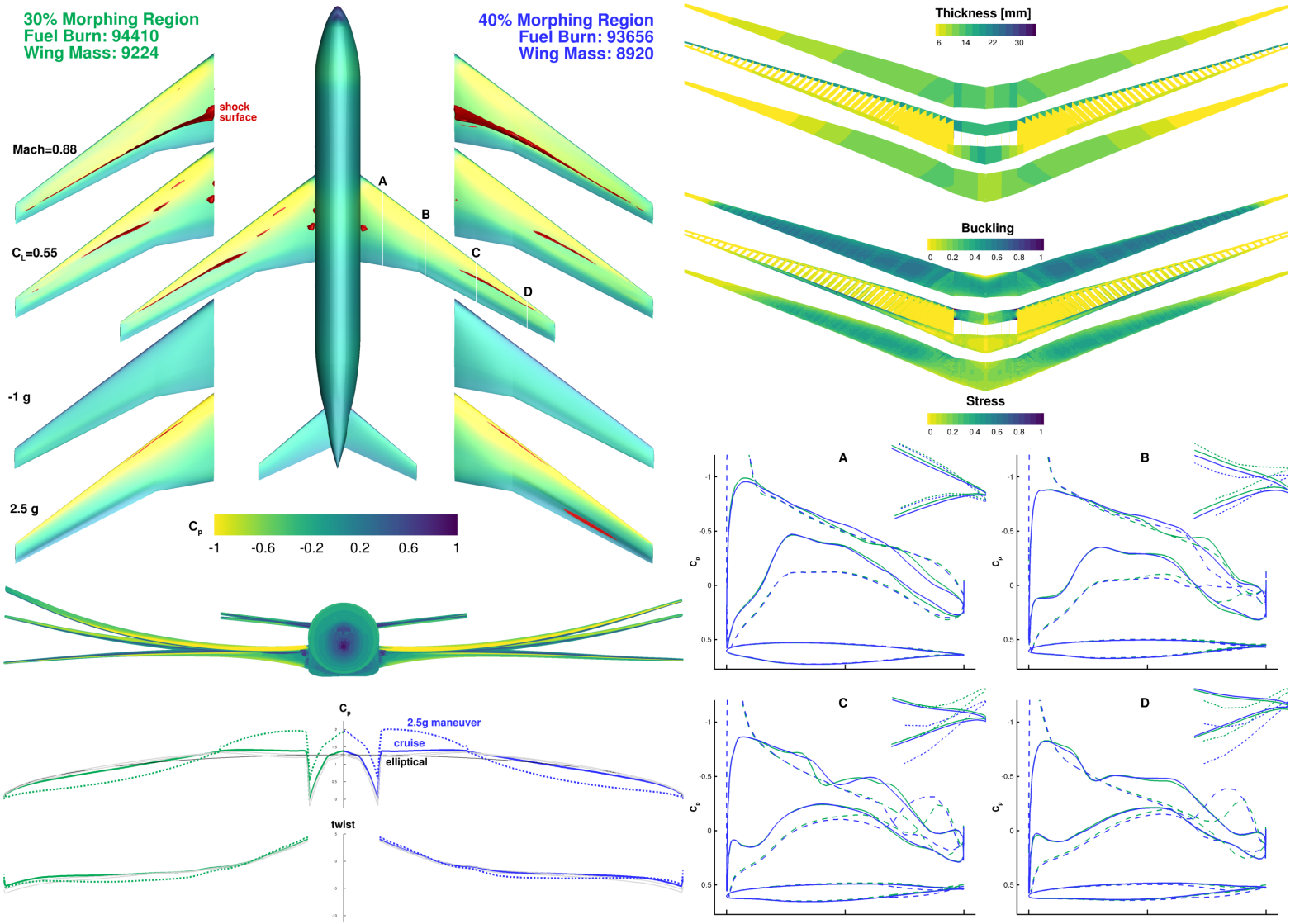

Figure 5.6: For the 7-point stencil when the morphing region was reduced from 40% to 30% of the chord, the fuel burn increased by 0.81% and the wing mass increased by 3.41%.

section.

This section includes two optimizations. First, a conventional wing is optimized to set a baseline for reference. That same optimization is repeated with the addition of morphing design variables. The baseline configuration for these optimizations is the uCRM-13.5, as described in Chapter 3. The morphing region for this optimization again spans the aft 40% of the wing. the FFD used for these optimizations is shown in Figure 5.7.

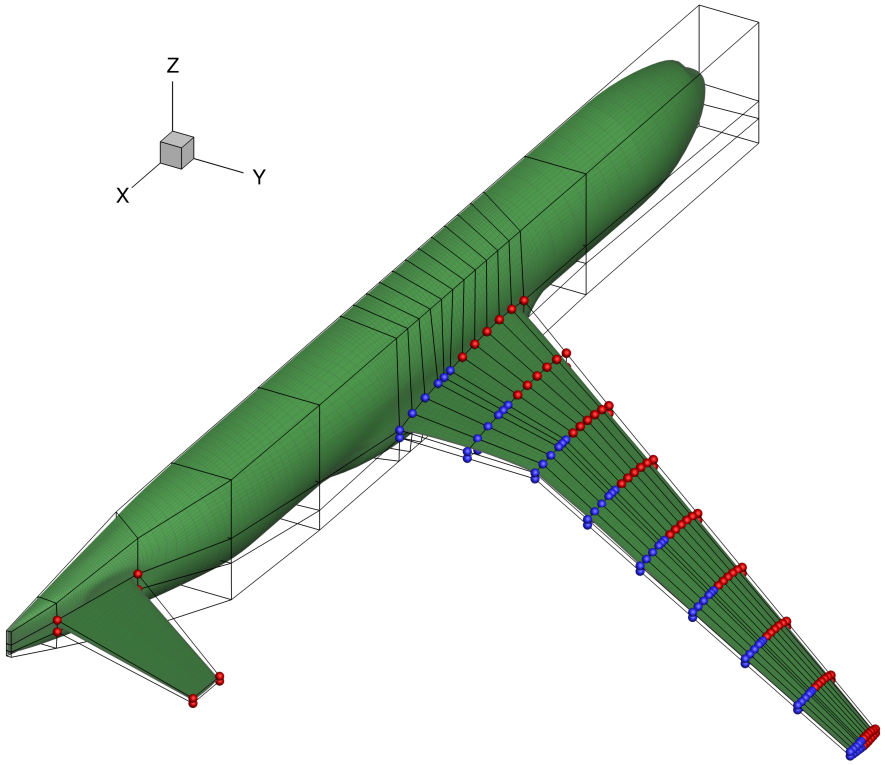

Figure 5.7: The FFD used for the uCRM-13.5 optimizations included morphing variables (in blue) on the aft 40% of the wing.

To explore the hypothesis that increasing the aspect ratio of a wing increases the effectiveness of morphing technology, we consider a 3-point optimization much like that outlined in Table 5.3. The results of that optimization are shown in Figure 5.8.

The optimization results confirm the assumption that morphing trailing edge de-

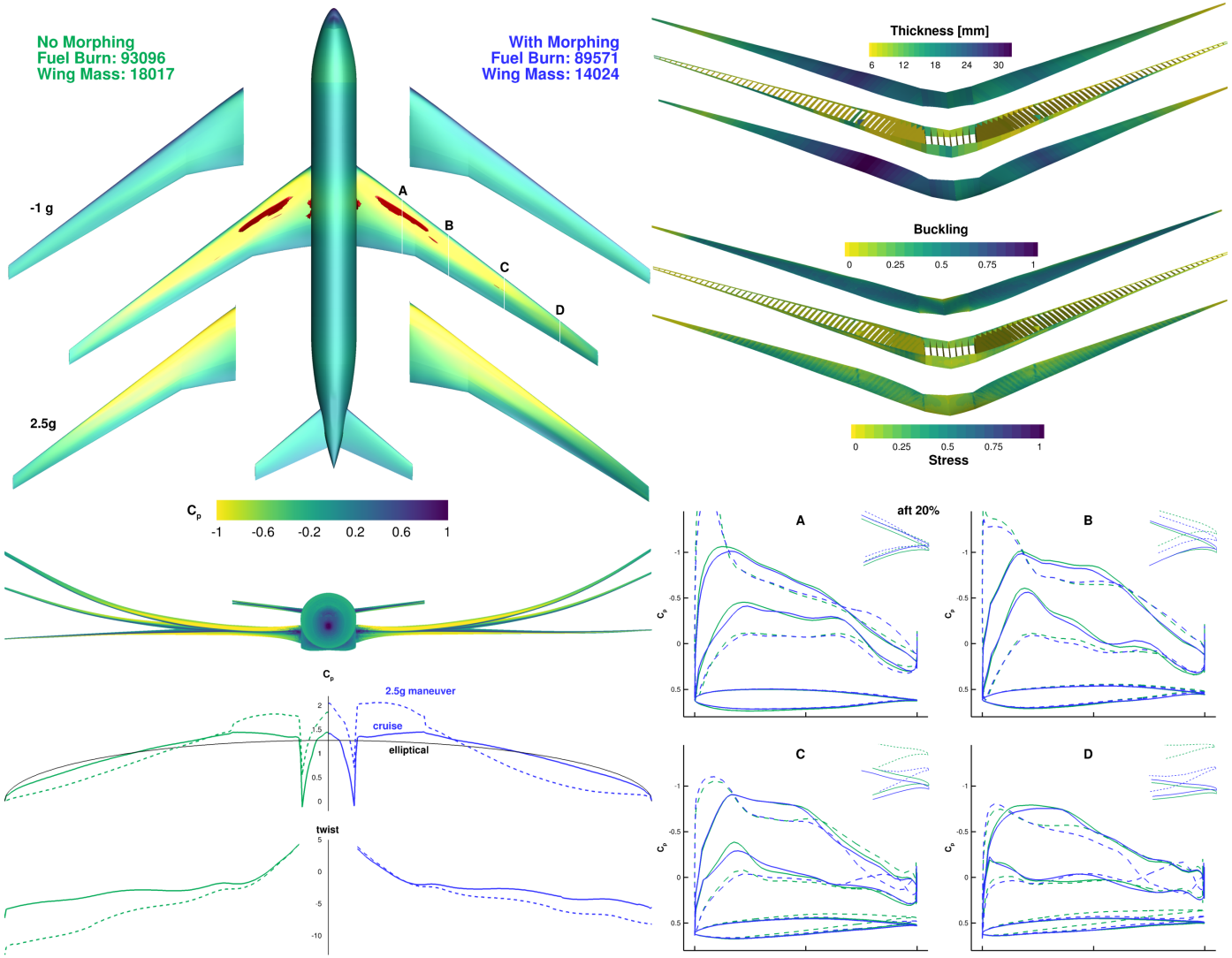

Figure 5.8: Adding a morphing trailing edge device to the high aspect ratio uCRM enabled a 22.2% reduction in structural weight, and produced a fuel burn savings of 3.79%.

vices are more effective for higher aspect ratio wings. Comparing the results in Figure 5.8 to those from previous optimizations, we again see many of the same trends. The morphing device produced substantial fuel burn reductions due largely to an inboard shift of the maneuver load distribution. Comparing the results in Figure 5.8 to those in Figure 5.3, we see the percentage reduction in structural weight is nearly identical (22.2% vs 22.4% for the high and low aspect ratio wings, respectively). However, the fuel burn reduction is more significant for the high aspect ratio case (3.79% vs. 2.53%). It follows that in the high aspect ratio optimization, the morphing device is able to provide more substantial aerodynamic improvements. As the aspect ratio increases, the robustness of conventional wings becomes limited, providing more opportunity for morphing devices to improve performance. It is clear that through maneuver load alleviation and increased aerodynamic robustness, morphing trailing edge technology can help enable higher aspect ratio wing design in future aircraft.

5.3 Summary

In this chapter are a number of multipoint optimizations that clearly demonstrate the value of morphing technology. While the singlepoint results in Section 4.2 produced limited benefits from morphing technology, the multipoint results in this section show much larger gains. These multipoint optimizations are summarized in Table 5.4.

Stencil	**Morphing**	**Fuel Burn** [kg]	**Wing Mass** [kg]
3 point	No	94,421	29,573
	Yes	92,034	22,938
7 point	No	98,627	30,060
	Yes	93,656	22,300

Table 5.4: As the multipoint stencil size is increased from 3 to 7 points, the fuel burn savings increases from 2.53% to 5.04%, respectively.

In the singlepoint optimizations in Section 4.2, the clean sheet morphing design

burned 0.358% less fuel than its counterpart without morphing. The 3-point optimization in this chapter yielded much better results, as the addition of morphing reduced fuel burn by 2.53%. This comparison of the benefits of morphing technology on 1-point and 3-point (and 2 maneuver) optimizations clearly demonstrates that singlepoint optimizations are insufficient to quantify the benefits enabled by morphing technology. While aeroelastic tailoring effectively designs an aircraft for a single cruise and a single maneuver condition, its ability to design a wing for additional conditions is limited. Bend-twist coupling can effectively tailor a wing's singlepoint performance, but given the passive nature of this tailoring, the benefits become limited as additional flight conditions are considered. The addition of morphing adds the active versatility the wing needs to perform more efficiently for a range of conditions. When optimized for the 7-point stencil, the addition of morphing technology produced an even larger 5.04% fuel burn reduction. Further, a comparison of the results from the 3- and 7- point stencils highlighted the trade-off between a lighter structure and improved aerodynamic performance, resulting from more consistent deformed shapes with a heavier structure.

The comparison also demonstrated the effect that morphing technology has on this trade-off in wing weight. Without morphing, adding more points to the multipoint stencil produces a heavier stiffer optimized wing, which helps maintain consistency in structural deformations at the various cruise conditions, improving aerodynamic performance, and thus fuel burn. This trend reverses with the addition of morphing. As more points are added to the multipoint stencil of a wing with morphing, the optimal structural weight is reduced. Because the morphing reduces the coupling between performance at various flight conditions, the benefit associated with increasing the consistency of the structural deformations is reduced. This can alternatively be considered as follows: Given that the morphing technology largely makes up for the aerodynamic cost of compromising for a multipoint stencil, the aerodynamic bene-

fit associated with increasing the structural weight, and thus the consistency of the deformed wing shapes, is reduced. This in turn shifts the balance in the trade-off between a lighter and heavier wing structure, increasing the incentive to reduce the wing weight to save fuel burn.

Extrapolating this result further, since an aircraft does not need to perform well at a discrete set of flight conditions, but rather over the typical flight envelope, morphing technology clearly incentivizes a reduction in structural wing weight. At first glance, many understand that morphing technology increases the aerodynamic versatility of an aircraft, and thus improves aerodynamic performance at a variety of flight conditions. These results demonstrate a more subtle conclusion: while there is an aerodynamic benefit resulting from the versatility of morphing technology, there is also a shift in the trade-off between weight and drag, incentivizing structural weight reductions. Given the maneuver load alleviation capabilities of morphing technology, this structural weight reduction becomes the major factor in the efficiency improvement provided by morphing for aircraft of this size.

Given the potential for restrictions on the size of the morphing region, particularly in relation to the aft spar of the wing box, this thesis includes analogous morphing optimizations with a smaller morphing region. This smaller region spanned the aft 30% of the chord, leaving 10% of the chord between the morphing region and wing box for actuator mechanisms, high lift devices, etc. While the smaller morphing mechanism was less effective, the increase in fuel burn with respect to the wing with the larger morphing mechanism was limited. For both the 3- and 7-point cases, the increase in fuel burn associated with the decrease in morphing region was less than 1%, suggesting that the sensitivity of the performance of the morphing device with respect to the size of the morphing region is small.

In the final multipoint optimization in this chapter, we sought to identify whether increasing the aspect ratio and flexibility of a wing would increase morphing tech-

nology's effectiveness. A comparison of the fuel burn savings produced by adding a similar morphing trailing edge on a current generation wing to those produced on a higher aspect ratio next generation wing shows that morphing technology is clearly more effective for higher aspect ratio wings. This result is very important given the trend in aircraft design to move towards higher aspect ratio wings. There will be a synergistic effect developed by the use of next generation structural materials and morphing trailing edge technology.

CHAPTER 6

Benefits of morphing considering full mission

The studies up to this point in this thesis have used a series of single- and multipoint aerostructural design optimizations to compare the performance of aircraft with and without a morphing trailing edge device. These have been meaningful comparisons; however, they are also limited. First was a comparison of singlepoint optimizations in Chapter 4. This comparison did not appropriately capture the benefits of morphing trailing edge technology, as it was limited in the diversity of flight conditions it considered. Next, the optimizations were expanded to consider a multipoint stencil in Chapter 5. The multipoint optimizations did a much better job capturing the benefits offered by morphing technology, but this approach is still limited. The objective function of the multipoint optimizations is an average cruise fuel burn, as calculated with the Breguet range equation, Equation 4.2. Inherent in this optimization is the assumption that the fuel burn at cruise drives the total fuel burn for a mission, as contributions from taxi, takeoff, climb, descent, and landing are ignored. This assumption generally introduces an acceptable amount of error, particularly for long distance flights, and still allows the designer to produce a configuration with improved fuel burn.

As this thesis is considering the effects of morphing trailing edge devices, there is potential for dramatic improvement at off-design conditions, so consideration of non-

cruise portions of a mission may be important. This chapter expands on the previous results and comparisons by comparing performance of a conventional aircraft to that of an aircraft with a morphing trailing edge over the course of a mission, including climb, cruise, and descent. A second major change for the studies in this chapter with respect to those from previous chapters is the size of the morphing region used herein. For this study, the morphing region spans the aft 10% of the wing, representing a small morphing region, which can offer easier integration with current wing configurations and high lift devices.

6.1 Aerodynamic optimization of the CRM

This section considers aerodynamic-only optimization of the CRM with a small morphing device. The studies in previous chapters have demonstrated that structural considerations are critical for a full evaluation of the ability of morphing trailing edge technology to reduce fuel burn. A comparison including those structural changes is included in later sections; however, this study seeks to isolate the effect of the improved aerodynamic robustness without considering active load alleviation.

6.1.1 Mission profile

The mission used to quantify the fuel burn savings resulting from the inclusion of the morphing trailing edge has a range of 7,730 nautical miles, based on the maximum range of a Boeing 777-200ER. The mission includes two step climbs during its cruise. The step climbs are larger than what is seen in a typical flight, but the three altitudes correspond to nominal flight conditions at full fuel weight, half fuel weight, and empty fuel weight, and the inclusion of such drastic changes in flight conditions should effectively demonstrate the value of a morphing trailing edge. These cruise altitudes were selected the same way as those from the 7-point cruise stencil in Figure 5.2. The mission profile is shown in Figure 6.1.

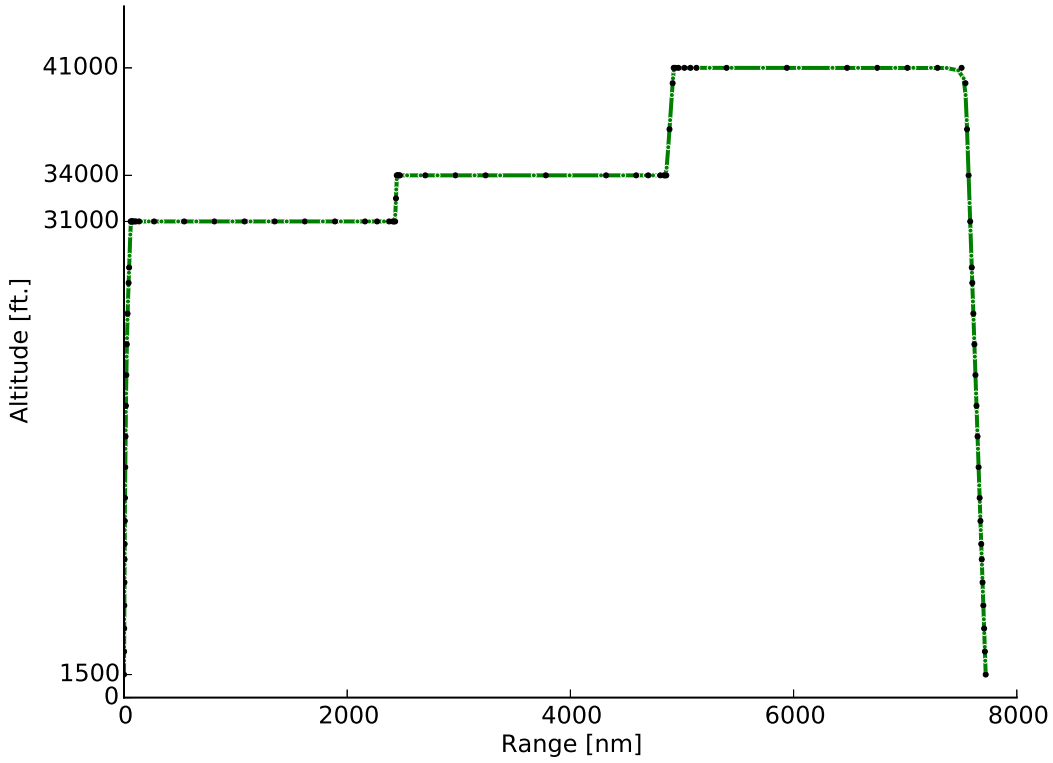

Figure 6.1: The representative mission used in the morphing trailing edge aerodynamic optimization includes climb, cruise (with two step climbs), and descent.

The mission starts its climb at an altitude of 1,500 ft. An accelerating climb continues to 10,000 ft where the the indicated air speed is 250 kts. The aircraft continues climbing and increasing speed until it reaches 13,000 ft, where the velocity increase stops. At 28,000 ft, the aircraft reaches the Mach limit crossover, and becomes limited by the Mach number, which is set to 0.85. The Mach number remains at 0.85 for the remainder of the climb to the first cruise altitude of 31,000 ft, corresponding roughly to a lift coefficient of 0.5 at MTOW. The 34,000 ft altitude corresponds to a lift coefficient of 0.5 for half-fuel weight, and the final altitude of 41,000 ft gives the same lift coefficient for LGW. A slowing descent at 2° returns the aircraft to an altitude of 1,500 ft. Takeoff and landing are not included in these analyses because of the high lift requirements at those conditions. Our framework constrains our geometry

to a constant topology, which prevents the inclusion of analysis of high lift devices. As such, including the flight conditions at takeoff and landing would lead to those conditions having a disproportionately large influence on the design of the aircraft.

In Figure 6.1, the black points represent B-spline control points, which define the shape of the profile. That combination of control points results in the mission profile shown by the green line. The green points embedded within the green mission profile line represent the collocation points, where the governing equations are enforced by pyMission. To simplify the fuel burn calculation, approximate fuel weights are pre-defined at each of the collocation points. These fuel weights were calculated with a lower fidelity aerodynamic panel-based surrogate. This approximation neglects second order implicit effects coming from a lower drag requiring less fuel, yielding a lower required lift at points earlier in the mission. However, the first order effects resulting from a decreased drag yielding a lower fuel burn are captured.

6.1.2 Aerodynamic surrogate model

During the mission analysis, an aerodynamic surrogate is required to prevent the mission analysis from becoming unreasonably slow. The computational cost of a high fidelity RANS solution is too large for use at every flight condition encountered by the mission analysis tool during its convergence. As such, we provide aerodynamic performance through a surrogate model that can be evaluated quickly. The data for these analyses is a series of trimmed lift-to-drag ratios computed at 240 flight conditions, as shown in Figure 6.2.

The novel surrogate model parameterization assumes optimal morphing shape scheduling throughout the mission. Rather than basing the surrogate on a series of active morphing actuator positions, these variables are pre-optimized based on the other active flight parameters (like Mach number, lift coefficient, and altitude) and removed from the mission analysis. This approach can be generalized to any variables

which are actively changed in-flight and which have optimal values based on the flight condition.

There are a few key points to notice about the selection of the flight conditions used to train the surrogate model. First, the flight conditions are bunched at higher Mach numbers. This is intentionally done as this region of the flight envelope has larger gradients, and thus requires finer data resolution to accurately capture the trends. At lower Mach numbers, performance contours are much more smooth, and therefore require fewer data points to resolve. Another aspect of the data point distribution to consider is the shape of the convex hull created by the points. The data is contained within the boundaries shown in black in Figure 6.2 for two reasons. Some boundaries were put in place as they define explicit boundaries beyond which we know no data will be required. For example, due to the problem formulation, we know that no data will be required for Mach numbers beyond 0.85. As such, in our data set we include enough data to provide an accurate cubic fit at that Mach number. In other words, we provide data two points beyond a Mach number of 0.85. As seen in Figure 6.2, the data set is bounded at a Mach number of 0.87. The other reason for boundaries on the data set is the robustness of the aerodynamic solver. At conditions with too much separation or at slow speeds, the solver can encounter errors. Such errors typically require manual intervention to address, and are thus undesirable within an automated optimization of 240 morphed wing shapes. While the solver is robust within the domain of the training points, that does not guarantee solver accuracy at those conditions. While it is not considered here, additional work could explore the accuracy of the aerodynamic solutions at extreme flight conditions, and the implications of that accuracy on predictions of morphing benefits.

Once the L/D values are computed at each of the specified flight conditions, the surrogate is constructed with a cubic interpolation function, along with a nearest point approximation for points that fall outside the convex hull of the training data.

Because we are considering only aerodynamic effects in this case, a two dimensional flight condition space is sufficient, assuming that the Reynolds number changes are small and that the aircraft is trimmed everywhere. This will not be the case in the later aerostructural study, where structural deflections are a function of the additional flight condition dimension.

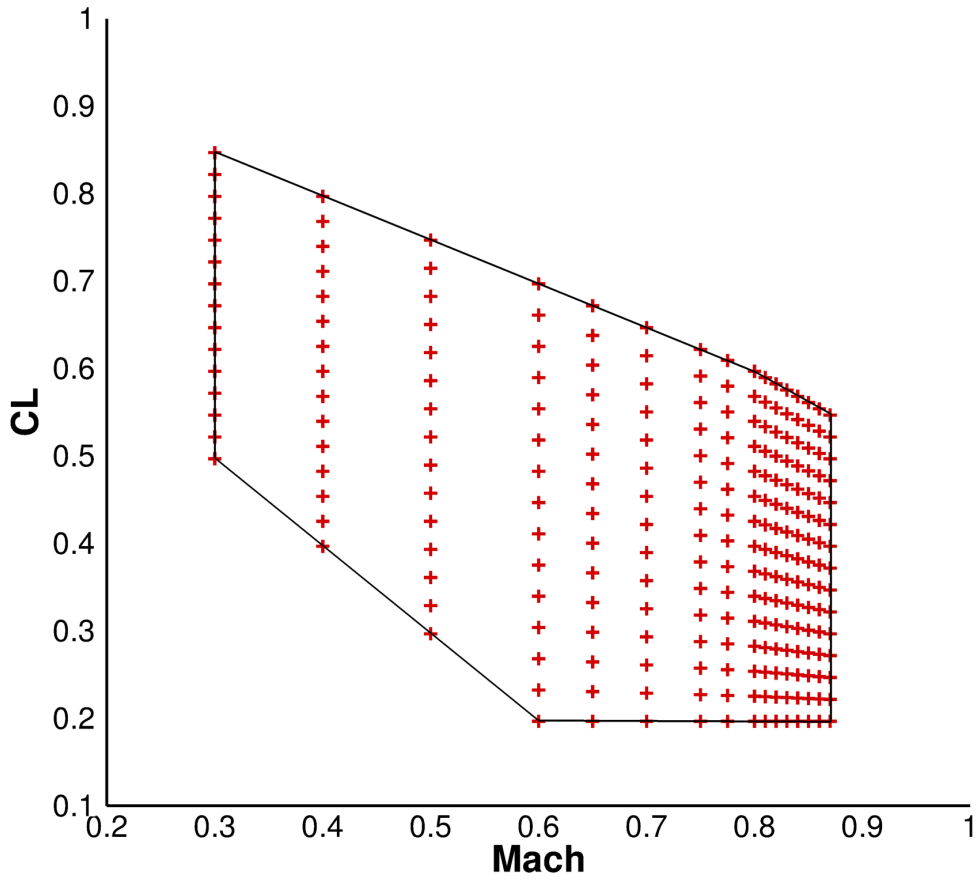

Figure 6.2: A 240-point stencil was used to create surrogates of the aerodynamic performance.

6.1.3 Optimization problem formulation

The objective of this study is to develop an adaptive morphing trailing edge wing that outperforms a conventional wing in terms of fuel burn over the provided mission. Starting from the baseline CRM configuration, a series of 240 aerodynamic shape optimizations at the various flight conditions shown in Figure 6.2 are performed. The purpose of these optimizations is to find the shape of the morphing section that provides the best performance for the wing at the given flight conditions. By aggregating the performance improvements resulting from wing morphing at each of the flight conditions, we can quantify the fuel burn reduction provided by adaptive wing technology.

The problem definition for each of the 240 aerodynamic shape optimizations, as shown in Table 6.1, is identical, except for the variance in flight conditions. Thirty-two morphing design variables were used in each optimization. Tail rotation and angle of attack are also variables, which allow the aircraft to trim and meet its lift requirement. A wing volume constraint is used to ensure that sufficient volume is available for fuel in the wing. Additionally, to ensure that the optimized morphing shapes are physically reasonable, 200 linear thickness constraints are distributed throughout the morphing section of the wing. These constraints prevent the morphing design variable from dramatically changing the thickness within the morphing region of the wing. The thickness constraints use a 2% thickness tolerance. Without this small freedom, the problem becomes too strictly constrained, and the optimizer is unable to consistently find feasible solutions at the various flight conditions being analyzed. A more detailed explanation of the optimization problems used to define optimal trailing edge shapes with respect to flight conditions is given in Table 6.1.

	Function/variable	Description	Quantity
minimize	C_D	Drag coefficient	
w.r.t.	α	Angle of attack	1
	x_{shape}	Morphing shape (FFD)	32
	η	Tail rotation angle	1
		Total design variables	**34**
subject to	$C_L = C_L^*$	Lift coefficient constraint	1
	$C_{M_y} = 0$	Moment coefficient	1
	$V/V_{\text{init}} \geq 1$	Fuel volume	1
	$0.98 \geq t/t_{\text{init}} \geq 1.02$	Thickness constraints	200
		Total constraints	**203**

Table 6.1: Overview of a morphing trailing edge optimization problem.

6.1.4 Aerodynamic shape optimization results

The aerodynamic shape optimizations were completed with a 363,000 cell (L2) mesh. A 3 million cell (L1) mesh was then used for an aerodynamic analysis of the baseline wing at each of the stencil points. Next, the drag reduction between the L1 and L2 meshes for the baseline wing at each flight condition was computed. This drag reduction was then applied to the results from the morphing shape optimizations, to give an appropriate estimate of the drag on the morphed designs throughout the stencil. This approach prevents the need for any optimization to take place on the finer mesh, saving computational time [59]. The approach is summarized as follows:

$$D_{1m} = D_{1b} - D_{2b} + D_{2m} \tag{6.1}$$

where D_{1m} is the drag coefficient on the morphing trailing edge wing with the L1 mesh, D_{1b} is the drag coefficient on the baseline wing with the L1 mesh, D_{2m} is the drag coefficient on the morphing trailing edge wing with the L2 mesh, and D_{2b} is the drag coefficient on the baseline wing with the L2 mesh.

The purpose of these optimizations is to create an aerodynamic surrogate for mission analysis, so we consider the results of the optimizations within that context.

To visualize the impact of the adaptive trailing edge on the aircraft's performance, we consider the difference in drag predicted throughout the stencil by the two surrogates, as shown in Figure 6.3.

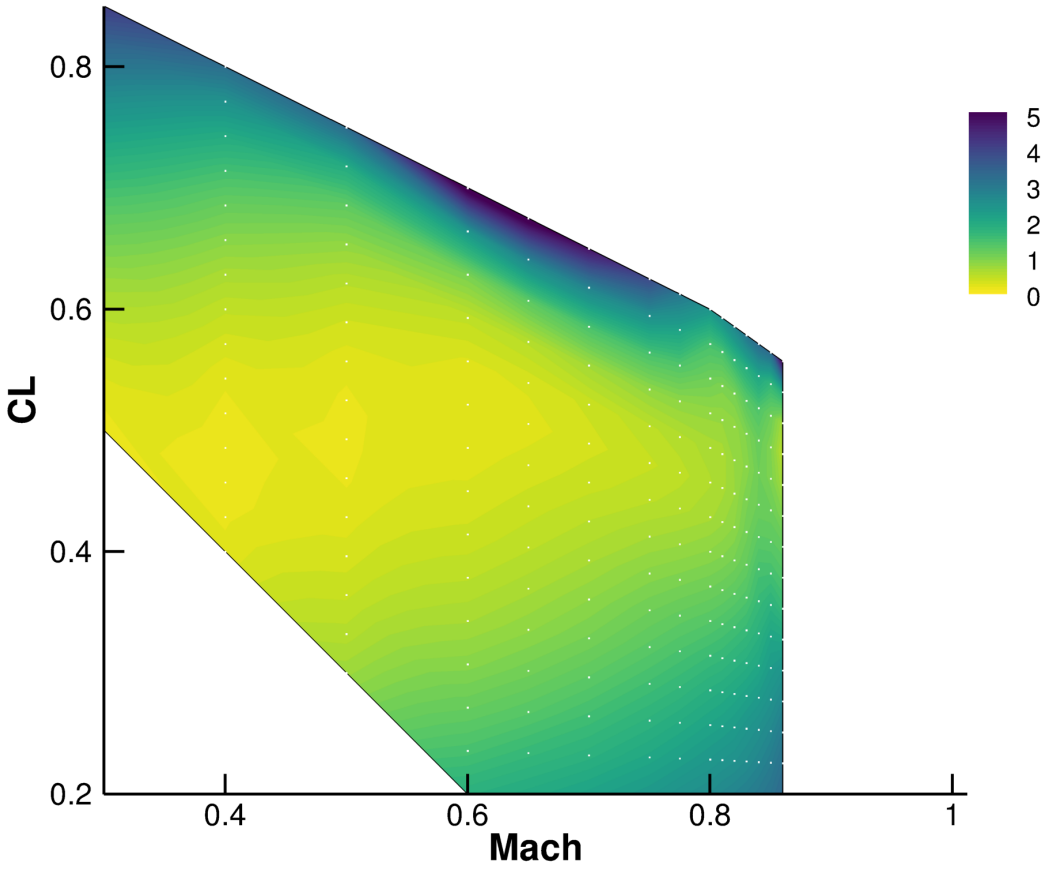

Figure 6.3: The percentage drag reduction throughout the stencil between the baseline CRM and the same wing retrofitted with an adaptive morphing trailing edge.

By analyzing the drag reduction plotted in Figure 6.3, we see that through a large region of the stencil, the drag reduction is less than 1%. However, near the boundaries of the stencil we see drag reductions as large as 5%. This result makes sense, because in the region where there is little savings, the Mach number and lift coefficient are both relatively low. This means that the wave drag and induced drag are low, and the

adaptive trailing edge cannot reduce them much more. In the regions with larger Mach number or lift coefficient, the drag was reduced more, as those off-design conditions produce more extraneous drag that can be removed. While the baseline configuration shows strong performance robustness, the addition of the morphing trailing edge is able to provide additional performance improvements at off-design conditions.

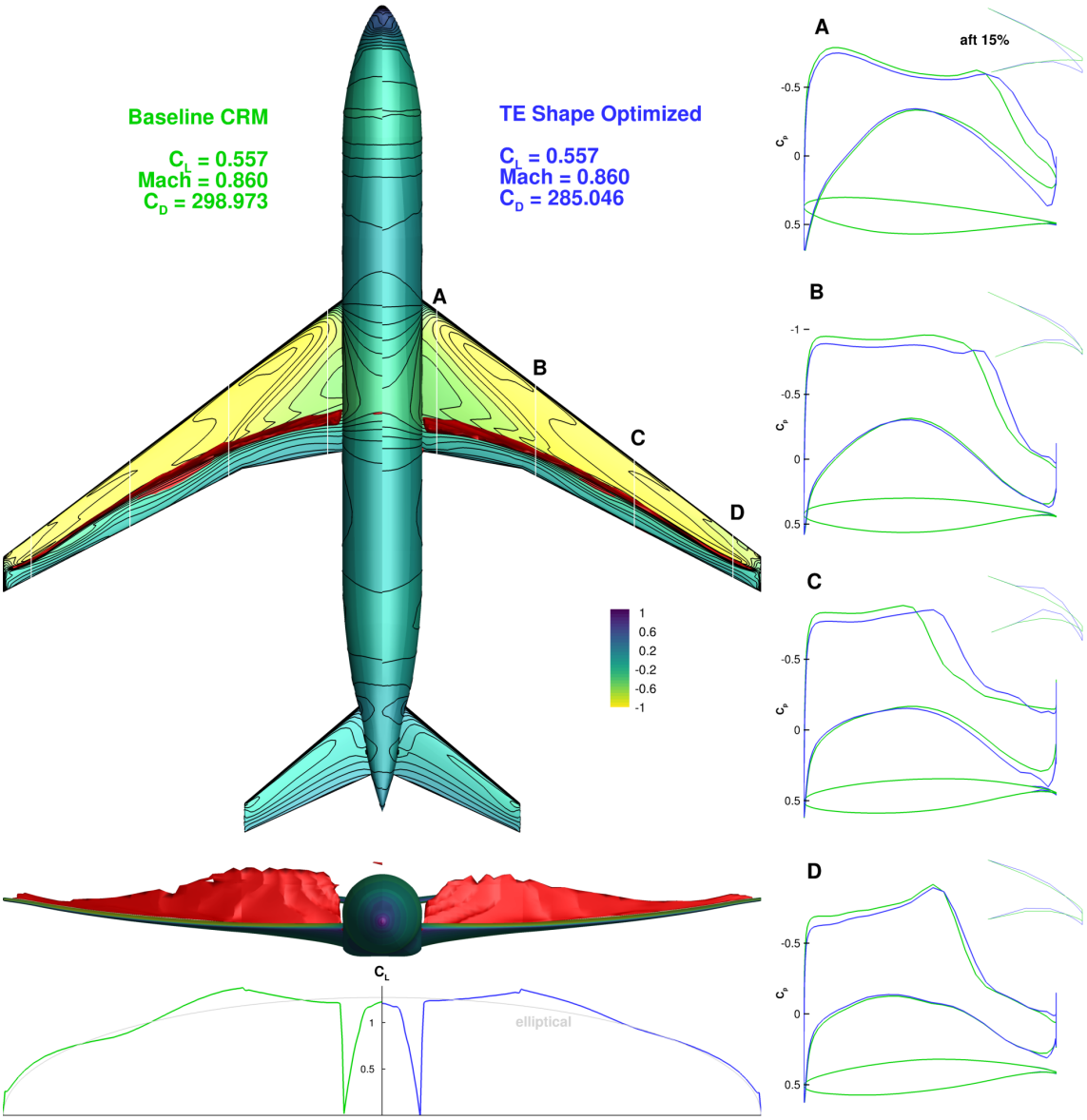

Figure 6.4: A summary of the morphing trailing edge aerodynamic shape optimization at $M = 0.86$ and $C_L = 0.557$.

For an example of how these savings are actually achieved, we consider in more

detail one of the morphing trailing edge shape optimization results, as shown in Figure 6.4. This optimization was run at $M = 0.86$ and $C_L = 0.557$, near the region with the highest drag reduction in the flight condition stencil. At this point, the drag coefficient is reduced by 4.62%. We can see this is a result of reduced wave drag and induced drag, as the shock (shown in red) has become smaller and the lift distribution is closer to elliptical after the morphing. On the right side of Figure 6.4, we also see airfoil and pressure distribution slices taken from four spanwise locations labeled A–D in the planform view. These slices also have an enlarged view of the morphing region, and the shapes that are designed with the FFD parameterization and mesh density used in this optimization.

6.1.5 Mission performance of the CRM retrofit with an adaptive wing

While the drag improvements are insightful, the true objective of this study is to reduce fuel burn over the course of the example mission, so we now consider what effects the trailing edge has in that regard. A summary of the fuel burn for the optimized wing and the original CRM is given in Table 6.2.

Wing	**Fuel Weight [lbs]**	**Percent Reduction**
Nominal CRM	105,737	-
Morphing trailing edge	104,639	1.04

Table 6.2: The adaptive trailing edge reduces the fuel burn by more than 1% as compared to the baseline wing.

As we can see from Table 6.2, the drag reductions achieved by the adaptive trailing edge successfully reduced the fuel burn by more than 1%. This is a relatively modest fuel burn improvement, but it is important to keep in mind what has been considered in this analysis, and conversely, what has not. This performance improvement is a result of an analysis in which the effects from increased aerodynamic robustness provided by the morphing trailing edge have been isolated. This improvement is strictly a result of improved aerodynamic performance during the climb, cruise, and descent

portions of a typical range mission for an aircraft of this size. This result illustrates a rigid wing's weakness in performing at a range of flight conditions experienced during a typical mission, as well as the ability of a small morphing trailing edge device on the aft 10% of the wing to effectively manage that weakness and improve the aircraft's robustness.

6.1.6 Summary

This section considered the aerodynamic performance benefit over the course of a full mission of retrofitting the CRM with a small morphing trailing edge device. Aerodynamic performance surrogates for the baseline CRM and the CRM retrofitted with the morphing device were generated using 240 aerodynamic morphing shape optimizations spanning the flight envelope. The individual morphing shape optimizations yielded drag reductions up to 5%. High lift and high Mach number flight conditions produced the largest benefit from the morphing device. The aerodynamic performance surrogates were used in an analysis of a 7,730 nautical mile mission including climb, cruise, and descent. Over the course of the mission, the morphing trailing edge device reduced the fuel consumption by a modest 1.04%. The selected mission spent a large portion of its flight in conditions where the morphing trailing edge provided limited benefits. Given that the initial design of the wing used herein is somewhat arbitrary, the next section considers a similar analysis, including an initial clean sheet redesign of the morphing CRM, using a multipoint aerodynamic optimization.

6.2 Aerodynamic optimization of the CRM including an initial multipoint redesign

The previous section found a 1% fuel burn reduction produced by aerodynamic shape optimization of a retrofit morphing trailing edge device on the CRM. In this

section the same mission analysis comparison is studied, using a baseline geometry determined using an initial multipoint optimization. This initial multipoint optimization is used to shape the front 90% of the wing, which was unchanged in the retrofit case in the previous section. The analysis in this section will use the same mission profile as the previous section, shown in Figure 6.1. The aerodynamic surrogate generation will also follow the same procedure outlined in the previous section, using the flight condition stencil shown in Figure 6.2 and the morphing shape optimization problem definition given in Table 6.1.

6.2.1 Initial aerodynamic multipoint optimization

The first step in this analysis is the definition of the new clean sheet design. The new design was generated with a 5-point aerodynamic optimization. The stencil used for this aerodynamic optimization is shown in Table 6.3. This 5-point stencil is a subset of the 7-point stencil in Figure 5.2, with the variation in altitude. The stencil is selected to be representative of a typical stencil used in aerodynamic shape design of a transonic wing design. Again, because this analysis is aerodynamic-only, Reynolds number effects are ignored and the flight condition space is reduced to two dimensions.

Flight Condition	**Mach**	C_L	**Description**
1	0.85	0.50	Nominal cruise
2	0.82	0.50	Low Mach
3	0.88	0.50	High Mach
4	0.85	0.45	Low C_L
5	0.85	0.55	High C_L

Table 6.3: The 5-point stencil for the multipoint design optimization that designs the baseline wing shape before the installation of the morphing trailing edge.

The multipoint aerodynamic optimization problem is shown in Figure 6.4. The objective function of the optimization is the minimization of the average of the

drag coefficients at the 5 cruise conditions. The design variables are the vertical $z-$displacements of 192 control points distributed around the FFD. As with previous optimizations in this thesis, the planform of the wing is kept constant. Eight twist variables are distributed along the span. Angle-of-attack and tail rotation variables at each condition provide means for meeting lift and moment constraints, respectively. Note that this multipoint optimization does not include any maneuver conditions. As this optimization is aerodynamic-only, and there are no structural considerations, there is no need for load-critical maneuver case consideration.

The multipoint aerodynamic optimization uses many constraints seen in previous optimizations herein. The wing volume is constrained not to decrease to ensure that there is enough space for the fuel. Linear constraints are added to both the leading and trailing edge to prevent shearing twist. A grid of 25×30 thickness constraints are distributed throughout the wing planform. These thickness constraints ensure a reasonably thick leading edge for low speed performance, a sufficiently thick trailing edge for manufacturability, and sufficient space for an efficient structure throughout the wing. The optimization problem is detailed in Table 6.4.

By optimizing the average drag at the five points in the multipoint stencil, we design a new baseline wing shape from which to add morphing. Note that this approach is not quite the same as that used in the previous clean sheet optimizations in this thesis. In those optimizations, the optimization generating the baseline shape of the wing considered morphing capabilities at non-nominal cases. Here, the baseline shape is determined with a typical aerodynamic multipoint optimization, and the morphing shape optimizations are subsequently run starting from that initial design. This approach will demonstrate the effects of multipoint optimization on full mission performance for transonic commercial transport-sized aircraft.

The results of the initial aerodynamic multipoint optimization are shown in Figure 6.5. The average drag at the five cruise conditions is more than 10 counts lower

	Function/variable	Description	Quantity
minimize	$\sum_{i=1}^{N} \mathcal{T}_i C_{D_i}$	Average drag coefficient	
w. r. t.	α_i	Angle of attack	5
	x_{shape}	Full wing FFD	192
	x_{twist}	Wing twist	8
	η_i	Tail rotation angle	5
		Total DVs	**210**
subject to	$C_L = C_L^*$	Lift coefficient constraint	5
	$C_{M_y} = 0$	Moment coefficient	5
	${}^{V}/_{V_{\text{init}}} \geq 1$	Fuel volume	1
	$\Delta z_{\text{LE,upper}} = -\Delta z_{\text{LE,lower}}$	Leading edge	8
	$\Delta z_{\text{TE,upper}} = -\Delta z_{\text{TE,lower}}$	Trailing edge	8
	${}^{t}/_{t_{\text{init}}} \geq 1$	Thickness constraints	750
		Total constraints	**777**

Table 6.4: Overview of the baseline multipoint optimization problem.

than that of the baseline CRM. This drag reduction demonstrates the effectiveness of the gradient-based multipoint optimization routine. Again justified by the findings of Lyu *et al.* [59], the multipoint optimization is completed using the 363,000 cell coarse CRM mesh that was used in the previous morphing shape optimizations. While the drag reductions found with this coarse grid are valid, the drag values themselves are around 40 counts higher than their physical values.

In support of the 10 count reduction in the average drag count, we see in Figure 6.5 that the nominal lift distribution has become more elliptical, and that the size of the shock has substantially decreased. These results demonstrate reductions in the induced and wave drag, respectively. The figure also shows airfoil and pressure coefficient slices at four spanwise locations labelled A–D. The results before and after the optimization are shown in green and blue, respectively. The pressure contours additionally show non-nominal distributions in grey. This multipoint optimization has created a better transonic wing design that serves as the new baseline for the next set of morphing shape optimizations.

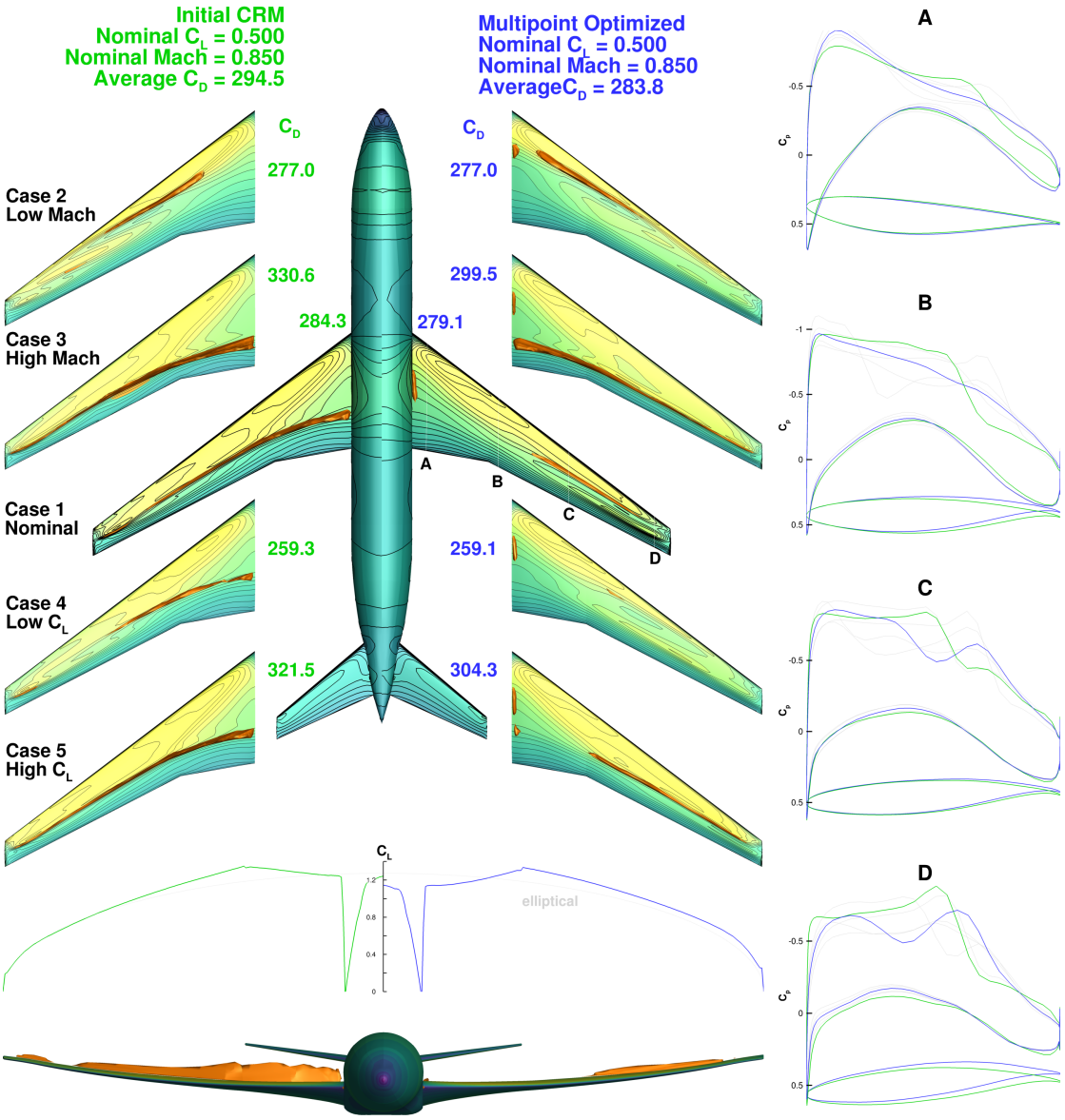

Figure 6.5: A summary of the initial multipoint optimization results. The optimization reduced the average drag at the 5 flight conditions by more than 10 counts.

6.2.2 Mission performance comparisons

After the multipoint optimization, the aerodynamic surrogate generation and mission analysis follow the same approach as was taken in Sections 6.1.4 and 6.1.5. The only difference between the optimizations here and those completed in the previous study is the initial geometry. Instead of using the baseline CRM geometry, these op-

timizations start from the mulitpoint optimization result from the previous section. Given that the only shape variables available in these morphing shape optimizations are those that control the morphing section, the forward 90% of the wing in these results is exactly equal to that from the multipoint optimization.

After the morphing shape optimizations were completed and the aerodynamic surrogates were developed, the next step was to run mission analysis on the multipoint and the multipoint-with-morphing configurations. The fuel burned by each configuration is given in Table 6.5, along with the values from the analysis without the initial multipoint optimization.

Wing	**Fuel Weight [lbs]**	**Percent Reduction**
Nominal CRM	105,737	-
CRM with morphing	104,640	-1.04
Multipoint optimized	106,495	0.717
Multipoint with morphing	104,649	-1.03

Table 6.5: The multipoint optimized wing has a higher fuel burn than the baseline CRM, and both morphing configurations have nearly identical fuel consumptions.

The fuel burn of the multipoint optimized wing is higher than that of the baseline CRM. This is a somewhat surprising result, as the common assumption that optimizing for cruise performance produces a more efficient design suggests that the multipoint optimized wing should outperform its baseline geometry. This result demonstrates that the baseline CRM geometry is a well-designed, robust wing. To better understand the relationship between the CRM and the multipoint optimized wing, we consider the percentage difference in drag between the two designs. This difference is shown across the stencil of flight conditions, in Figure 6.6.

Comparing the performance of the CRM and the multipoint optimized wing over the entire aerodynamic surrogate, we see that the baseline CRM outperforms the multipoint optimized wing at the majority of flight conditions (where the contour is blue). The multipoint optimization dramatically reduced the drag near the multipoint stencil; however, those improvements came at the cost of performance at most of the

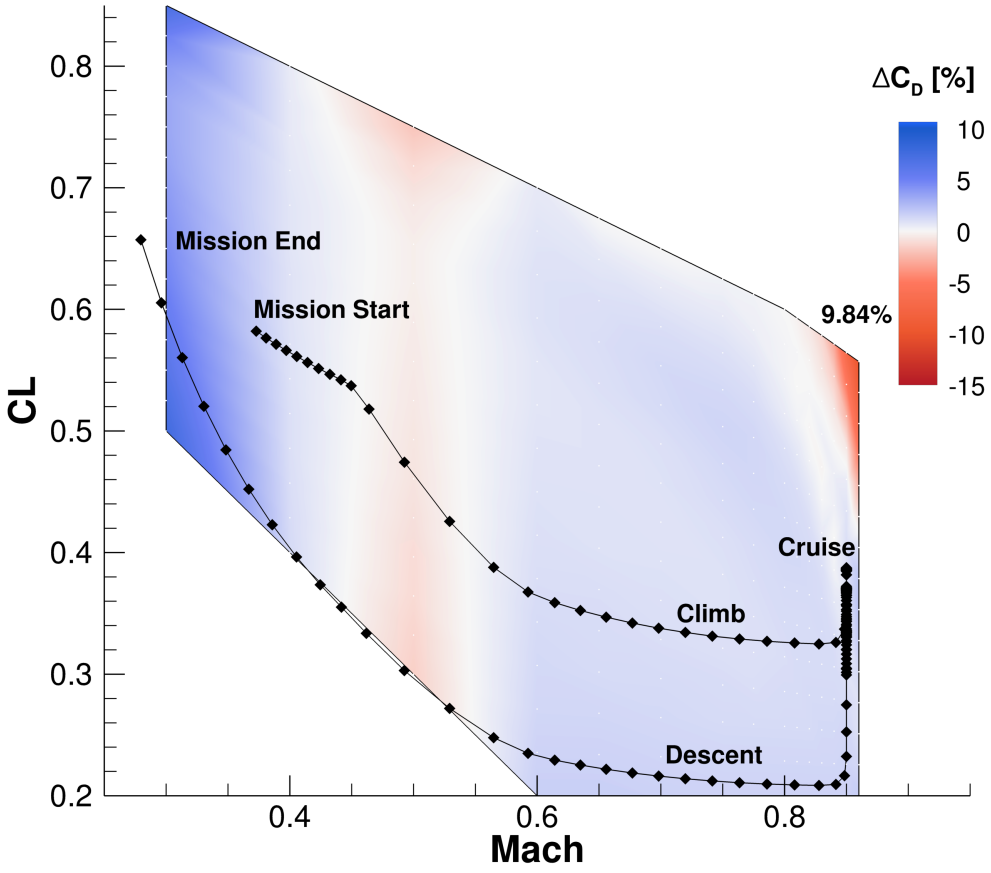

Figure 6.6: This contour shows the percentage change in drag coefficient between the baseline CRM and the multipoint optimized wing. Red sections show regions where the CRM has better performance, while blue regions show where the multipoint optimized wing performs better.

other flight conditions. Figure 6.6 also shows the path (in Mach-C_L space) the CRM took to complete the mission. Following this path, we see that it primarily lies in the region of the stencil where the CRM outperforms the multipoint optimized wing. The test mission doesn't reach C_L values near the nominal value used in the multipoint stencil, and thus does not take advantage of the improvements provided by the multipoint optimization. This example demonstrates the importance of multipoint stencil selection.

The next result of note in Table 6.5 is that the CRM with a morphing trailing edge and the multipoint optimized wing with a morphing trailing edge have nearly identical fuel burn values. The addition of the morphing trailing edge for the multipoint optimized wing dramatically improved the wing's performance robustness, and largely negated the performance losses away from the multipoint stencil that were added during the initial optimization. This relationship can be seen in the comparison of the CRM to the multipoint optimized wing with a morphing trailing edge, in Figure 6.7.

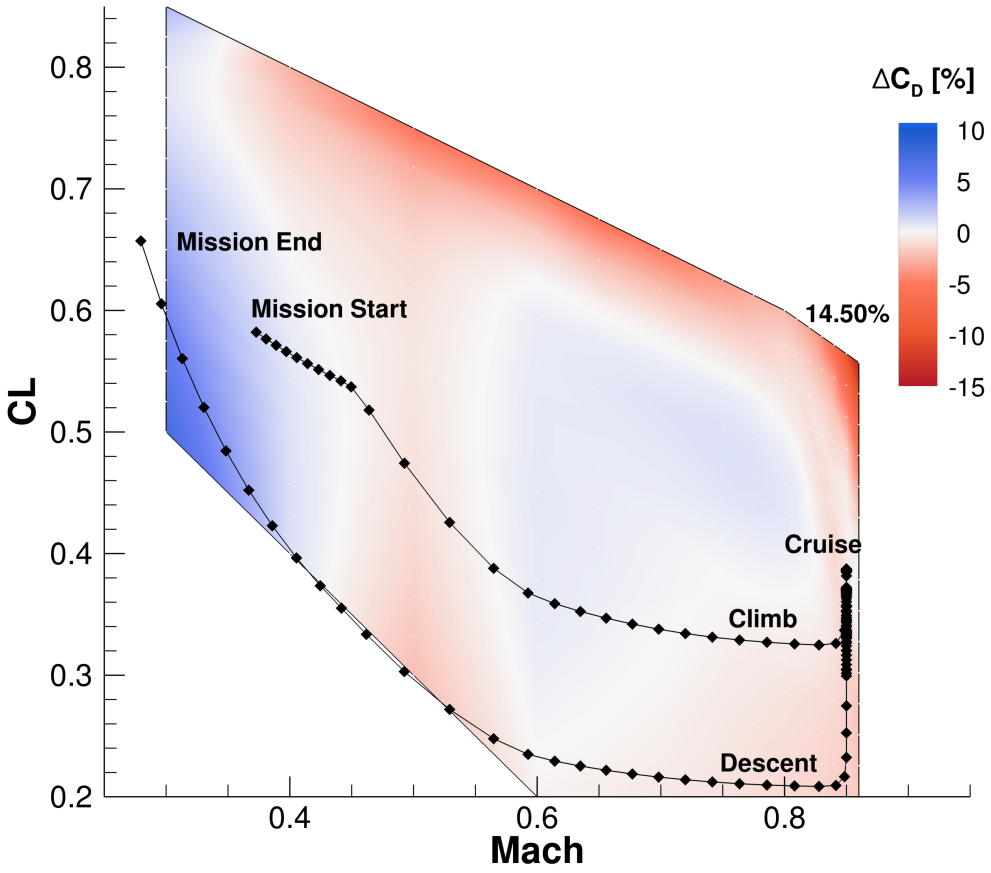

Figure 6.7: This contour shows the percentage change in drag coefficient between the baseline CRM and the multipoint optimized wing with a morphing trailing edge. Again, red sections show regions where the CRM has better performance.

While the majority of the stencil in Figure 6.6 shows better performance for the CRM compared to the multipoint optimized wing, the addition of a morphing trailing edge increases the efficiency of the multipoint optimized wing, which has better performance for most conditions in Figure 6.7. The morphing trailing edge made up for the losses from the multipoint optimization at many flight conditions, and improved the performance in the regions of the stencil where the multipoint design was already performing well. In the upper-right corner of the stencil, the multipoint design reduces the drag by about 10% compared to the CRM, but with the addition of morphing, that savings becomes 14.5%.

While the proximity of the fuel burn values for the two morphing configurations is largely a coincidental product of the selected mission profile, the result clearly demonstrates that a small morphing device can substantially improve a wing's performance at a variety of flight conditions. Starting from two initial geometries—one with relatively robust performance throughout the stencil, and another with very good performance in small regions and less efficient performance in large portions of the stencil—the morphing trailing edge device was able to produce designs with very similar overall performance.

6.2.3 Summary

In this section we repeated the aerodynamic morphing shape optimizations and mission analysis considered previously for the CRM, with the addition of an initial multipoint optimization. The multipoint optimization substantially improved the aerodynamic performance of the wing near the stencil, but reduced the wing's performance at other flight conditions. Adding a morphing trailing edge made up for many of the losses incurred during the multipoint optimization, and produced a wing with fuel burn requirements nearly identical to those of the CRM wing with a morphing device. Morphing trailing edge devices are able to improve the performance

robustness of a wide variety of initial conditions, again suggesting that retrofitting existing designs with morphing devices could be a feasible option. Having considered two cases with aerodynamic-only analysis, we now continue our study and consider the effects of structural deformations during the mission.

6.3 Aerostructural optimization of the uCRM retrofit with an adaptive trailing edge

The previous studies in this Chapter have considered aerodynamic-only analysis of morphing trailing edge devices. The results in Chapter 5 clearly demonstrated the importance of structural effects when quantifying the potential benefits of morphing trailing edge devices. As such, in this section we consider structural effects, although not in the same way as in the previous aerostructural optimizations in this thesis. This study considers a fixed wing box structure, and aerodynamic morphing shape optimization of a coupled aerostructural model. The baseline configuration used throughout these optimizations is the uCRM.

6.3.1 Mission profile

In this aerostructural analysis, we use essentially the same mission profile as was used in the aerodynamic analysis, but a few details of the mission become more important with the inclusion of structural considerations. First, because we are including structural deformations, the constant Reynolds number approximation is no longer valid. To compensate, we prescribe the altitude at each flight condition as well as the Mach number and lift coefficient. This gives us the three-dimensional flight condition space, which is discussed in more detail in the next section. The increased dimensionality of the flight condition space did affect the selection of the mission profile. By selecting a mission in which the Mach number is a function of altitude, we reduce

the dimensionality of the space the surrogate model needs to represent, allowing the use of fewer training data points. As such, the Mach number profile during descent does not exactly match that seen during a typical mission, but the effects of this difference are small with respect to the mission performance. Note also that this assumption was used during the aerodynamic-only study, to make the two studies as similar as possible and comparable. The mission profile and the altitude-Mach number relationship used to generate it can be seen in Figure 6.8.

6.3.2 Coupled aerostructural surrogate model

This mission profile was tested using pyMission and a low-fidelity performance surrogate developed with MACH's panel method code, Tripan [81]. An approximate lift coefficient profile required to fly the mission with the CRM was developed. This distribution served as the starting point from which the higher fidelity surrogate model's training points were selected. Given that the altitude-Mach number relation is prescribed throughout the mission, it can also be prescribed for the training data; however, variations are required in the other two dimensions. The relationship between the low-fidelity data and the location of the training points can be seen in Figure 6.8. The low-fidelity mission data is shown in black, while the selected training data points are shown in red. Note that like in the aerodynamic-only case, training points are more clustered near the transonic cruise region, where performance gradients are much larger than those in subsonic and lower lift regions.

The surrogate model for aerodynamic performance is based on the Regularized Minimal-energy Tensor-product Spline (RMTS) interpolant [114]. This method uses cubic tensor-product splines to generate a minimum energy interpolant from unstructured data. These features allow the method to work well for banded data in 2-4 dimensional space, which is the type of data being modelled herein. While the relationship between Mach number and altitude would have allowed the surrogate model

to be reduced to two dimensions, that simplification is not made. The additional computational time required to converge the RMTS interpolant with a third dimension as compared to just two dimensions was negligible, so the simplification was not necessary.

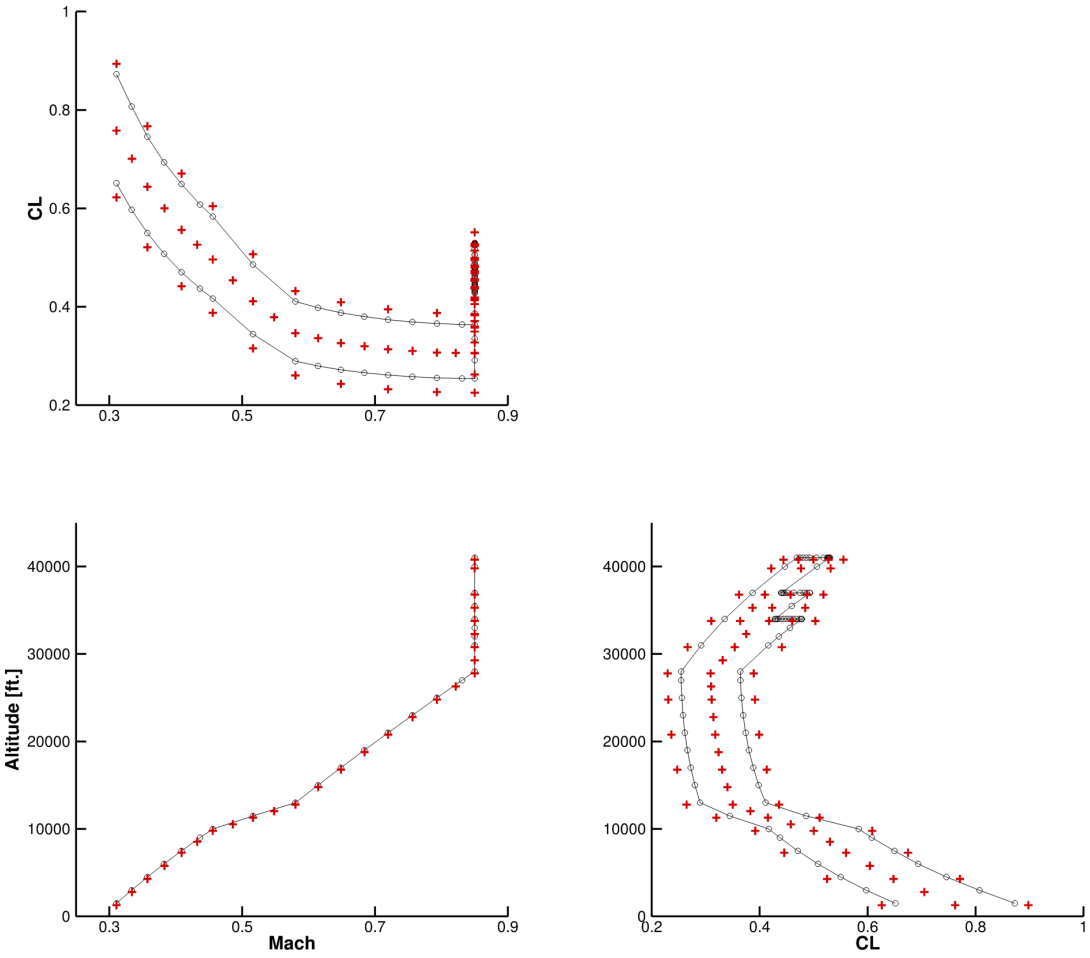

Figure 6.8: A set of 65 training points (in red) were used in the aerostructural performance surrogate. The training point locations were selected based on a low-fidelity mission analysis model, shown in black.

6.3.3 Optimization problem formulation

Starting from the baseline uCRM, we perform 65 optimizations of the morphing trailing edge shape. The optimization formulation is essentially identical to that from the aerodynamic-only study (outlined in Table 6.1), however structural deflections at each flight condition are included. In typical aerodynamic shape optimizations there are no considerations of structural effects, while typical aerostructural optimizations typically include control over both the structural sizing and the OML shape. This optimization does not fall strictly into either of those typical categories, as here there are no structural design variables. We are performing aerodynamic shape optimization with coupled structural analysis.

6.3.4 Coupled aerostructural optimization of the trailing edge shape

As we did for the aerodynamic results, we first consider the drag reduction resulting from the addition of the morphing trailing edge. The percentage drag reduction is shown in Figure 6.9. Note that this is not the exact interpolant used for the mission analysis, but rather a simplified two dimensional surrogate that takes advantage of the relationship between altitude and Mach number. Because this is the simplified interpolant, it is important to note that altitude changes also include changes in Mach number, as defined in Figure 6.8. The white points superimposed over the contour show the locations of the training data. While the interpolant solves for minimal energy throughout the entire region shown, values outside the convex hull of the training data should not be considered accurate. The energy-minimizing approach of this interpolant yields poor results in regions extrapolating from the provided data; however, since the data we need lies within the training data, this is not a problem.

Within the region of interest, the contour shows similar results to those seen in Figure 6.3 for the aerodynamic case. First, we see that as the altitude and Mach number are increased, the savings from the addition of the morphing trailing edge are

also increased. We also see increased savings at the larger lift coefficients, although this trend is not as strong as it was in the aerodynamic case. With the inclusion of altitude variation, the flight conditions with high lift coefficients are all at low altitude, which has reduced the savings from the morphing trailing edge. While the reductions at the low altitude conditions are smaller than they were for the aerodynamic case, they are larger almost everywhere else in the mission. This suggests that the benefits of a morphing trailing edge are more substantial with the inclusion of structural deflections.

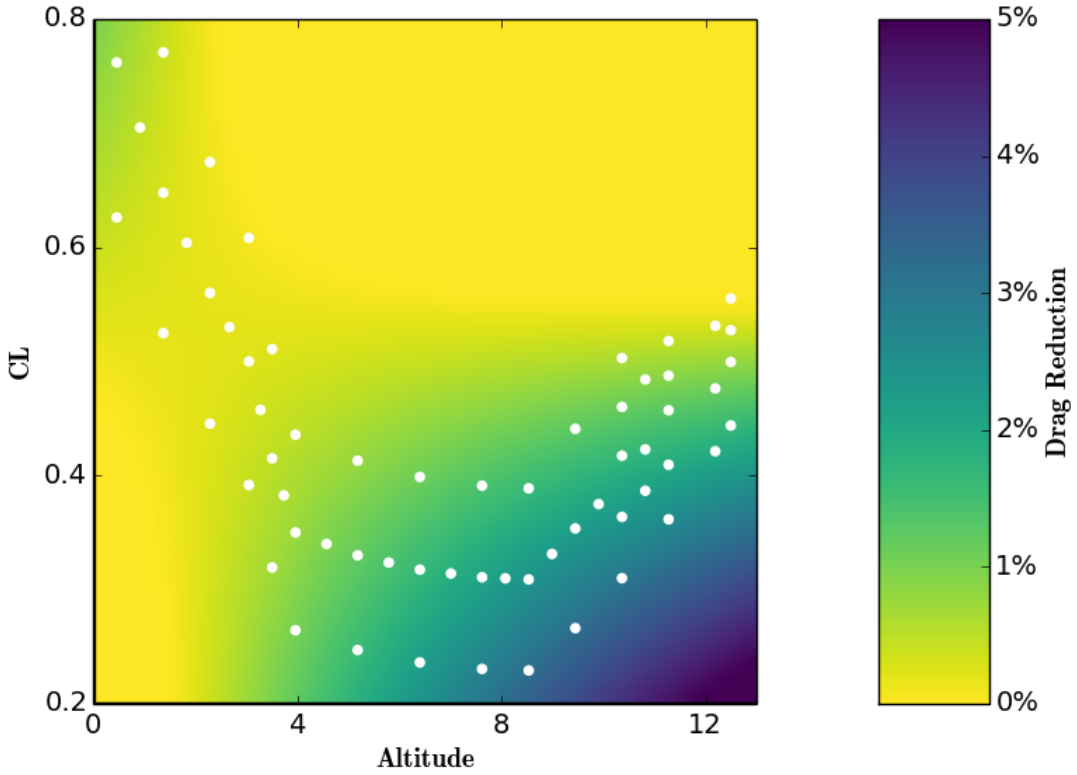

Figure 6.9: The percentage drag reduction for a 2-D interpolation of the aerostructural morphing trailing edge data.

6.3.5 Mission performance of an adaptive wing including structural deflections

Again, the true objective of these studies is to find the fuel burn improvements provided by the adaptive morphing trailing edge. With performance surrogates for both the baseline uCRM and the uCRM retrofitted with a morphing trailing edge on the aft 10% of the wing, we computed the fuel burn for each configuration over the prescribed mission. The fuel burn results are shown in Table 6.6.

Wing	**Fuel Weight [lbs]**	**Percent Reduction**
Nominal uCRM	100,568	-
Morphing Trailing Edge	98,834	1.72

Table 6.6: The adaptive trailing edge reduces the fuel burn by 1.72% compared to the baseline uCRM.

From the results in Table 6.6, we can see that with the addition of structural deformations, use of a morphing trailing edge reduced the fuel burn by 1.72%. This is a substantial increase compared to the 1.04% seen for the aerodynamic-only case. It is again important to consider what is responsible for that savings. The additional fuel burn reduction is strictly a result of the addition of structural deflections throughout the mission. The consideration of structural deflections applies a wider range of conditions to the wing throughout the mission, resulting in a larger potential for savings from increased robustness.

6.3.6 Summary

In this study, we considered the effects of structural deformations on the performance benefits provided by morphing trailing edge devices. Aerodynamic performance surrogates were developed using 65 high-fidelity aerodynamic morphing shape optimizations of the uCRM using coupled aerostructural analysis. When considering full mission analysis, the addition of morphing trailing edge devices produced a fuel

burn reduction of 1.72%. This value is directly comparable to the 1.04% reduction found in the aerodynamic-only studies in the previous sections. The additional fuel burn savings in this case are directly attributed to the improvements in performance robustness provided by morphing trailing edge devices. Without the robustness added by the active morphing, the baseline non-morphing uCRM wing encounters aerodynamic performance penalties resulting from structural deformations. Without considering maneuver load alleviation (which we have shown to provide the majority of the performance improvements for multipoint clean sheet wing design) the improved robustness provided by active morphing devices can yield a 1.72% reduction in fuel burn.

6.4 Aerostructural optimization of a uCRM morphing trailing edge including an initial clean sheet redesign

All of the previous studies in this chapter considering the benefits of morphing devices for full mission performance have not included structural weight reductions enabled by active load alleviation. As such, the savings found in those studies are directly attributed to the improved aerodynamic performance and robustness provided by morphing devices. In this section, we add the savings provided by maneuver load alleviation to the mission analysis. To accomplish this, we first redesign the wing using a multipoint aerostructural optimization that includes morphing at non-nominal conditions. That multipoint optimization provides the clean sheet new baseline design for the wing, including a lighter structure enabled by active load alleviation at maneuver conditions. Starting from that multipoint result, we again construct a performance surrogate like that in the last section. That surrogate is used to perform mission analysis of the same mission as outlined in Figure 6.8. Comparing the fuel burn of this configuration with that of the baseline CRM provides a full measurement

of the potential savings enabled by a small morphing device, including aerodynamic, structural, and mission analyses.

6.4.1 Initial aerostructural multipoint optimization

The first step in this study is the definition of the new baseline, non-morphed design of the wing. A 3-point aerostructural optimization defines this clean sheet design. While the full mission performance of the aerodynamic-only multipoint optimized wing in Section 6.2.2 shows that an initial aerodynamic optimization is not the best way to increase performance at all relevant flight conditions, that study did not include active load alleviation. Adding structural sizing optimization to the initial clean sheet optimization allows the morphing device to reduce the structural weight of the wing, which improves the fuel efficiency everywhere in the mission.

In the previous multipoint clean sheet design, the multipoint stencil was defined in terms of Mach number and C_L. The combination of the selected test mission and the location of the multipoint stencil led the multipoint optimization to produce a design which reduced the mission performance of the wing. To help address this issue, the stencil used in this multipoint optimization is defined in terms of lift, rather than C_L. As the structural weight of the aircraft is reduced, this change results in a stencil at lower lift, more accurately representing the conditions seen in the test mission. The cruise and maneuver conditions used in the multipoint optimization are shown in Table 6.7.

Flight Condition	**Mach**	**Load Factor**	**Description**
Cruise 1	0.85	1.00	Nominal cruise
Cruise 2	0.85	0.90	Low lift
Cruise 3	0.85	1.10	High lift
Maneuver 1	0.64	2.50	Pull up
Maneuver 2	0.64	-1.00	Push over

Table 6.7: The 3-point stencil for the multipoint aerostructural design optimization including active load alleviation.

The multipoint optimization problem is similar to those used in previous optimizations. A detailed description of the optimization problem is given in Table 6.8. The objective function is the aircraft's average fuel burn at cruise. Angle of attack and tail rotation design variables are included for each flight condition. The baseline shape of the wing at the nominal flight condition is defined with 192 shape variables and 8 twist variables. 854 structural variables including panel thicknesses, panel lengths, stiffener heights, stiffener thicknesses, and stiffener pitches control the wing box definition. 32 morphing variables are added for each non-nominal flight condition to control the shape of the trailing 10% of the wing.

The lift and pitching moment are constrained at each flight condition. The geometric volume of the wing cannot be decreased, to provide space for fuel in the wing. A consistency constraint ensures the fuel weight design variable (included in the structural sizing variables in Table 6.8) matches the fuel weight state variable. Geometric thickness constraints provide low speed performance, manufacturability, and sufficient space for actuators at the leading edge, trailing edge, and aft spar, respectively. Linear shape constraints prevent shearing twist and maintain constant thickness in the morphing region. Nonlinear structural constraints ensure the structural lengths match those defined by the FFD. Linear adjacency constraints prevent drastic variable differences in adjacent structural components. The failure of all structural members at the pull up condition are aggregated into 4 KS constraints. The buckling of all non-rib structural members is constrained at the pull up and push over conditions, with 3 KS constraints at each. In total, the optimization problem includes 1046 constraints.

The results of the initial multipoint optimization are shown in Figure 6.10. Note that this multipoint optimization was run twice, once with morphing and a second time without morphing, for reference. The non-morphing optimized wing is shown on the left of Figure 6.10, while the morphing result is to the right. We see similar

	Function/variable	Description	Quantity
minimize	Fuel burn		
w.r.t.	x_α	AoA	5
	x_{tail}	Tail rotation angle	5
	x_{shape}	Wing shape (FFD)	192
	x_{twist}	Wing twist	8
	x_{struct}	Structural sizing	854
	x_{morph}	Morphing shape (32×4)	128
		Total DVs	**1192**
subject to	$L = n_i W$	Lift	5
	$M = 0$	Pitching moment	5
	${}^{V}/_{V_\text{i}} \geq 1$	Fuel volume	1
	$x_{\text{fuel}} - y_{\text{fuel}} = 0$	Fuel mass consistency	1
	${}^{t}/_{t_\text{i}}\big\vert_{\text{LE}} \geq 1$	Leading edge thickness	20
	${}^{t}/_{t_\text{i}}\big\vert_{\text{TE}} \geq 1$	Trailing edge thickness	20
	${}^{t}/_{t_\text{i}}\big\vert_{\text{spar}} \geq 1$	Aft spar thickness	20
	$\Delta z_{\text{LE}_\text{u}} = -\Delta z_{\text{LE}_\text{l}}$	Fixed leading edge	8
	$c_1 x_i + c_2 x_j = 0$	Linear shape change constraints	8
	$L_{\text{panel}} - x_{\text{panel}} = 0$	Panel consistency	272
	$KS_{\text{stress}} \leq 1$	Pull up maneuver stress	4
	$KS_{\text{buckling}} \leq 1$	Maneuver buckling	6
	$\lvert x_{\text{str}_i} - x_{\text{str}_{i+1}} \rvert \leq 0.0005$	Adjacency	696
		Total constraints	**1046**

Table 6.8: This aerostructural multipoint optimization problem includes active load alleviation and is used to define the initial condition for subsequent morphing shape optimizations.

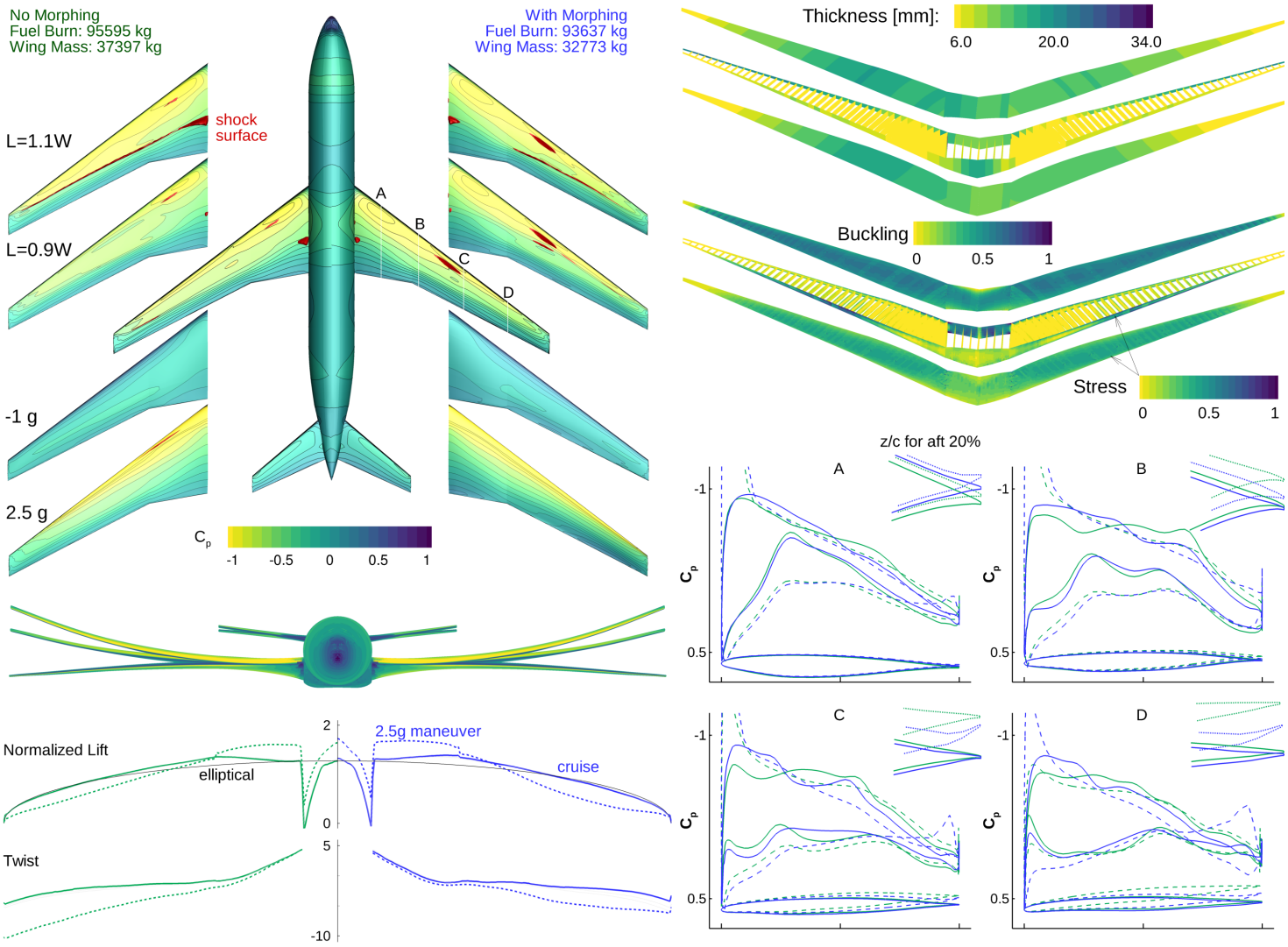

Figure 6.10: A comparison of the aerostructural multipoint optimization results with and without a morphing trailing edge on the aft 10% of the wing. The maneuver load alleviation enabled by the morphing trailing edge leads to a 12.4% reduction in the wing mass and a 2.05% reduction in the average fuel burn.

results here to those in Figure 5.3, although, the morphing here is limited to the aft 10% of the wing rather than the aft 40% as was the case in that comparison. As the morphing section is smaller, the benefits of morphing are correspondingly slightly smaller; although, as we saw previously with the 30% vs 40% comparison in Section 5.2.3, the size of the morphing region is not strongly related to the benefit of the morphing device. Small changes in the size of the device will only make small changes to the effectiveness of the device. While a 40% morphing region yielded about 2.5% fuel burn reduction, this 10% morphing region does nearly as well, providing a 2% fuel burn reduction. The mechanisms by which the morphing improves the aircraft performance are similar to those seen in the previous results.

With the addition of a morphing trailing edge, the lift distribution in Figure 6.10 at maneuver is shifted inboard. The airfoil slices show reflex regions at maneuver, particularly in the outboard regions, which reduce lift there. The effects of these reflex regions are also seen in the pressure distributions at the pull up maneuver. The pressure distributions at slices C and D show regions of negative lift near the trailing edge. This load alleviation enables the structural weight reductions seen in the thickness distributions.

6.4.2 Mission performance of an adaptive wing including active load alleviation

The nominal shape of the multipoint optimized wing from the previous section is used as the baseline configuration for the morphing shape optimizations. The morphing shape optimizations are formulated exactly like those from the previous studies. The relevant problem formulation is shown in Table 6.1. Like in the last study, the morphing shape optimizations include structural deformations; however, the structure in this study is the lighter, more flexible structure that was designed by the initial multipoint optimization. Again 65 morphing shape optimizations are

performed at the flight conditions outlined in Figure 6.8. The results of the optimizations are aggregated into a performance surrogate using the same 3-dimensional RMTS interpolation method used in the previous section. Along with the changes to the performance surrogate, the aircraft weight is adjusted in the mission analysis to reflect the weight reductions achieved by the active load alleviation. Compared to the baseline CRM, the optimized morphing aircraft with maneuver load alleviation has a 3.08% lower total aircraft weight.

Wing	**Fuel Weight [lbs]**	**Percent Reduction**
Nominal uCRM	100,568	-
Retrofit morphing wing	98,834	1.72
Clean sheet morphing wing	97,828	2.72
Theoretical uCRM	98,856	1.70

Table 6.9: The clean sheet adaptive trailing edge design requires 2.72% less fuel than the baseline uCRM.

Over the course of the test mission, the clean sheet morphing trailing edge design burned a total of 97,828 pounds of fuel. This total, along with the other related results are shown in Table 6.9. While the addition of a morphing trailing edge without the inclusion of structural weight reductions (retrofit design) produced a fuel burn savings of 1.72%, the clean sheet design saved 2.72% fuel compared to the baseline uCRM. Listed in Table 6.9 is an additional "theoretical uCRM" result. This aircraft represents the uCRM if it had the same aeroelastic performance, but had a 3.08% weight reduction, like that which was enabled by the maneuver load alleviation. This theoretical aircraft saves 1.7% on fuel compared to the actual uCRM. When considered together with the other results in Table 6.9, this result demonstrates the trade-off between structural weight reductions and aerodynamic performance. For the test mission, structural weight reductions (in the theoretical uCRM) and improved aerodynamic performance (in the retrofit morphing wing) both independently save around 1.7% fuel burn compared with the baseline uCRM wing. If these two effects were independent of each other, we would expect to be able to apply them

sequentially to get a 3.4% fuel burn savings on the clean sheet design. Instead, the two effects conflict with each other, as lighter structures produce larger deflections and limit aerodynamic performance.

6.4.3 Summary

In this section, we studied the performance of a clean sheet redesign of the uCRM with a morphing trailing edge on the aft 10% of the wing. The clean sheet design was analyzed over a full mission, and compared with previous designs in this chapter. The clean sheet design was developed with an initial aerostructural multipoint optimization that included active maneuver load alleviation. That initial optimization reduced the structural weight of the uCRM wing by 15.73%. Compared with a clean sheet design without a morphing trailing edge, the weight of the wing is 12.4% lower. The multipoint optimized morphing wing was used as the baseline for 65 aerostructural morphing shape optimizations. The optimized performance of the morphing wing at a variety of flight conditions was aggregated into a performance surrogate that was used for mission analysis. Over the course of a full mission, the clean sheet morphing design required 2.72% less fuel than the baseline uCRM. Combined with the results in previous sections of this chapter, this result clearly demonstrates the trade-off between aerodynamic performance and structural weight reductions for morphing wing design.

6.5 Summary

In this chapter, we considered a number of morphing wing optimization studies involving full mission analysis. Mission analysis is included to get a more representative measure of the benefit of morphing technology over the course of a mission than is provided by the use of the Breguet range equation in a multipoint optimization. Given the adaptability of morphing technology, full mission analysis can expose fuel

burn savings during non-cruise portions of a flight that would be missed with less accurate models of mission analysis.

We started with aerodynamic-only optimization of the CRM with a morphing trailing edge. The CRM was retrofit with a small morphing trailing edge device on the aft 10% of the wing. The shape of the morphing device was optimized at 240 flight conditions. In large portions of the flight regime, the morphing device provided nearly no benefit, although at high Mach number and high lift conditions, the drag was reduced by as much as 5%. The performance of the baseline CRM and the CRM retrofit with the morphing device were aggregated into aerodynamic surrogates. These surrogates were used in mission analysis of a 7,730 nautical mile mission with three cruise altitudes. Over the course of the mission, the small morphing device reduced the fuel consumption of the CRM by 1.04%. This modest savings is partially attributed to the selected mission, but is fairly representative of the potential savings during a standard flight.

The next study considered the aerodynamic clean sheet design of the same CRM wing. To generate a clean sheet design, the CRM was first optimized using a multipoint stencil centered at the nominal flight condition. This initial optimization produced an average drag reduction of 10 counts at the flight conditions in the stencil. That multipoint design was used as the baseline for the subsequent 240 morphing shape optimizations spanning the flight regime. Surrogate models for the aerodynamic performance of both the multipoint optimized wing and the multipoint optimized wing with a morphing trailing edge were constructed. Those surrogates were again used in mission analysis on the same test mission. Interestingly, the multipoint optimized wing increased the fuel consumption over the course of the mission. While the multipoint optimization reduced drag near the multipoint stencil, it did so at the expense of performance at off-design conditions. Those conditions were experienced during the full mission, and limited the effectiveness of the multipoint optimized

wing. After the morphing trailing edge was added to the multipoint optimized wing, its integrated fuel burn performance nearly matched that of the original CRM with a morphing device. The proximity of these integrated values is largely a coincidence based on the selected test mission, but it demonstrates the effectiveness of morphing devices in improving the efficiency of a number of initial designs.

The next study in this chapter built on the previous studies by adding coupled aeroelastic analysis. The uCRM was retrofit with a morphing trailing edge device on the aft 10% of the wing. The morphing shape of this wing was optimized using aerostructural analysis. These aerostructural morphing shape optimizations were completed at 65 flight conditions spanning a band of typical conditions within Mach number-C_L-altitude space. The performance of the baseline uCRM and the retrofit morphing wing were assembled into performance surrogates built with an RMTS interpolant. Compared with the baseline uCRM, the retrofit configuration used 1.72% less fuel. In this study, no active load alleviation-enabled weight reductions were included. The structure in both wings was the baseline structure of the uCRM. The increased fuel burn savings from about 1% in the aerodynamic-only cases to about 1.75% in this case demonstrates the effect structural deflections can have on aerodynamic efficiency. Without morphing, structural deflections reduce the aerodynamic performance of the uCRM wing; however, the small morphing trailing edge device can largely negate those losses, improving the performance robustness of the wing.

The final study in this chapter considered a clean sheet redesign of the uCRM with a small morphing trailing edge device. The clean sheet configuration was designed with an aerostructural multipoint optimization. This optimization included morphing capabilities and structural sizing design variables, and thus took advantage of the active load alleviation enabled by the morphing trailing edge. The wing structural weight was reduced by 15.73%. That multipoint optimized configuration was used as a baseline for another 65 aerostructural morphing shape optimizations.

The performance of the clean sheet morphing wing was aggregated into a surrogate model the same way as the configurations in the previous study. Compared with the baseline uCRM, the clean sheet morphing configuration used 2.72% less fuel over the course of the mission. An additional theoretical wing was considered, which had the aeroelastic performance of the baseline uCRM and the mass of the clean sheet design. This theoretical wing yielded a 1.70% fuel burn reduction compared with the CRM. Considering the four aerostructural models discussed in this chapter, the trade-off between reducing structural mass and improving aerodynamic performance is clear. In the optimizations in this study, the mission discipline was considered in sequence to the coupled aerostructural optimizations. To completely address the trade-off in structural weight and aerodynamic performance at the appropriate flight conditions, a fully coupled mission-aero-structural optimization with morphing is required.

CHAPTER 7

Conclusions

7.1 Final Remarks

This chapter gives an overview of the final conclusions of this thesis, the main contributions of this work, and a few potential directions for future work building on the research herein.

7.2 Conclusions

Given the environmental dangers of maintaining current levels of pollution and carbon emissions, and the time and work still required before more efficient aircraft configurations are available to the market, the aircraft industry is pursuing a number of technologies that offer efficiency improvements for current- and next- generation aircraft. One such technology is morphing trailing edge devices. The work in this thesis leverages state of the art computational methods to evaluate the potential efficiency improvements offered by morphing trailing edge technology. Specifically, I use high-fidelity MDO to compare optimal performance of aircraft with and without morphing capabilities. These comparisons yield a number of insights about the effectiveness of morphing trailing edge devices and their influence on the trade-offs involved in aircraft design.

In Chapter 3, we demonstrated the impact of aerodynamic solver accuracy on transonic shape optimization. The CRM wing was optimized with both Euler and RANS solvers, and the resulting optimized shapes were compared. The wing shape found using optimization with Euler analysis produced nearly 10% more drag than the wing optimized with RANS analysis. This result demonstrated the need for high-fidelity RANS analysis for transonic wing design. Exclusively using lower fidelity models like the Euler equations or panel methods does not provide the accuracy needed to appropriately shape transonic wings.

In Chapter 4, the uCRM was aerostructurally optimized for cruise performance, both with and without a morphing device. The morphing device considered in this study spanned the aft 40% of the wing. The single point optimizations in this study minimized cruise fuel burn while preventing failure at maneuver. To establish a baseline, the uCRM was first optimized without any morphing variables, producing a design with 5.8% lower fuel burn. That optimized, non-morphing configuration was then compared to a wing retrofit with a morphing device and a clean sheet design that included morphing.

The CRM retrofit with a morphing device reduced the fuel burn as much as the complete optimization without morphing capabilities. This result demonstrated the potential morphing devices can have for retrofit application to existing aircraft. The clean sheet optimized wing with morphing produced a fuel burn 0.36% lower than that of the optimized non-morphing wing. Both the retrofit and clean sheet designs used active load alleviation at the maneuver condition, although the retrofit design shifted more of the load inboard to reduce the structural weight more, as it did not have shape control of the leading 60% of the wing.

These optimizations demonstrated that singlepoint aerostructural optimization with consideration of one cruise and one maneuver condition is insufficient for evaluating the benefits offered by morphing technology. Although singlepoint optimization

navigates a trade-off between cruise and maneuver performance, passive aeroelastic tailoring does a good job managing the compromise needed between the opposing objectives. As such, there is little additional savings available to active load alleviation in singlepoint optimization. To get a better measure of the potential of morphing trailing edge technology, we next considered multipoint optimizations.

Chapter 5 compared a number of multipoint aerostructural optimizations with and without a morphing trailing edge device. First, the uCRM optimized with and without morphing for a 3-point stencil were compared. In this case, the morphing trailing edge device reduced the fuel burn by 2.53% and the structural weight by 22.4% compared with the wing optimized without morphing.

The same aerostructural optimization comparison was repeated on a 7-point stencil, which produced larger differences in performance. The wing with morphing saved 5.05% on fuel burn, and reduced the weight of the wing by 25.8%, again compared with the same wing optimized without morphing. Comparing in more detail the mechanisms by which the morphing device improved performance in the various optimizations, we found that structural weight reductions enabled by active load alleviation are the primary factor in the efficiency improvement provided by morphing technology for commercial transport-sized aircraft.

In an additional investigation, we considered the implications of reducing the size of the morphing device. Specifically, we repeated the 3- and 7-point optimizations with a morphing region spanning the aft 30% of the wing, to compare with the previous optimized wings with a morphing region over the aft 40% of the wing. Reducing the morphing region size by 25% resulted in just a 0.22% increase in fuel burn, and a 2.78% increase in wing weight for the 3-point optimization. Similarly, for the 7-point optimization, reducing the size of the morphing region to just the aft 30% of the wing yielded a 0.81% increase in fuel burn and a 3.41% increase in wing weight. From these results we concluded that the benefits provided by morphing trailing edge

devices are not strongly dependent on the size of the morphing region.

We next considered the influence a wing's aspect ratio has on the benefits provided by morphing trailing edge devices. The 3-point optimization comparison using a 40% morphing region was repeated with the uCRM-13.5. Compared with the 2.53% fuel burn savings found for the aspect ratio 9 CRM, morphing reduced the fuel burn of the uCRM-13.5 by 3.79%. Interestingly, the structural weight reductions in the two comparisons were similar, at 22.4% and 22.2% for the uCRM and uCRM-13.5, respectively. This demonstrated the positive relationship between wing flexibility and the benefits of morphing. We concluded that morphing technology offers additional benefits for higher aspect ratio wings.

In Chapter 6, we considered the implications of a small morphing device on the aft 10% of a wing over a 7,730 nautical mile mission, including climb, cruise, and descent. We developed aerodynamic and aerostructural surrogate models of baseline and optimized configurations for use in mission analysis. Using aerodynamic analysis and optimization, the nominal CRM was compared with the CRM retrofit with a morphing trailing edge device, a multipoint optimized configuration without morphing, and the multipoint optimized wing with morphing. Over the course of the mission, the multipoint optimized wing had the worst performance, burning 0.717% more fuel than the baseline wing. This result demonstrated the importance of multipoint stencil selection, and more generally optimization problem objective function selection. Interestingly, both configurations with morphing reduced the fuel burn compared to the baseline CRM by about 1%. This result further demonstrates the potential for use of morphing trailing edge devices retrofit on a variety of existing aircraft.

The final results in this thesis consider mission analysis paired with aerostructural optimization of morphing and non-morphing wings. Again performance surrogates were developed, including coupled aeroelastic effects. Compared with the nominal uCRM, a uCRM retrofit with a morphing trailing edge device was found to increase

fuel efficiency by 1.72%. Expanding further to a clean sheet redesign of the uCRM with morphing, we found a 2.72% reduction of fuel burn compared with the nominal uCRM. From this result, we concluded that even a small morphing device on the aft 10% of a wing provides enough active versatility and performance robustness to noticeably improve an aircraft's efficiency.

7.3 Contributions

Given the high-fidelity and coupled nature of the work herein, this thesis represents the state of the art for aircraft design optimization, particularly for morphing trailing edge aircraft. The main contributions of this thesis are as follows:

1. Demonstrated the need for high-fidelity RANS analysis in transonic wing design.
2. Performed high-fidelity single- and multi- point aerostructural optimization of a commercial transport-sized aircraft with a morphing trailing edge.
3. Developed a novel morphing-wing surrogate parameterization scheme that leverages optimization to assume ideal morphing scheduling, removing the need for morphing variable consideration in mission analysis
4. Performed the first mission analyses using performance surrogates trained with $\mathcal{O}(100)$ high-fidelity aerodynamic and coupled aerostructural optimizations of morphing trailing edge aircraft.

7.4 Recommendations for future work

Throughout this thesis, a number of potential directions for future work have been encountered that can continue to advance the state of the art of high-fidelity coupled aircraft design optimization for use in novel technologies like morphing trailing edge devices.

1. The analysis and optimization in this work did not consider the control systems required for morphing actuation. This application offers potential for high-fidelity coupled aeroservoelastic optimization.

2. This thesis clearly demonstrated that morphing trailing edge devices are more effective for higher aspect ratio next generation wings. A comparison of optimal planform shapes with and without morphing capabilities can more clearly detail the influence morphing technology has on the trade-offs between structural weight and aerodynamic performance.

3. The full mission studies in this thesis sequentially paired high-fidelity coupled aerostructural design with mission analysis. While a fully coupled system presents a number of challenges due to the number of function evaluations required for mission analysis and the cost of high-fidelity aerostructural optimization, tighter coupling between these disciplines could provide meaningful insights about the trade-offs between mission, structural, and aerodynamic performance.

4. The full mission studies used a series of mission analyses, without optimization. Adding mission and potentially allocation optimization for morphing aircraft can identify and explain further implications of morphing trailing edge devices.

BIBLIOGRAPHY

BIBLIOGRAPHY

[1] Air Transport Action Group, "Facts and Figures," `http://www.atag.org/facts-and-figures.html`, Feb. 2017.

[2] Lee, D. S., Fahey, D. W., Forster, P. M., Newton, P. J., Wit, R. C., Lim, L. L., Owen, B., and Sausen, R., "Aviation and global climate change in the 21st century," *Atmospheric Environment*, Vol. 43, No. 22, 2009, pp. 3520–3537.

[3] Solomon, S., *Climate change 2007-the physical science basis: Working group I contribution to the fourth assessment report of the IPCC*, Vol. 4, Cambridge University Press, 2007.

[4] Cattafesta III, L. N. and Sheplak, M., "Actuators for active flow control," *Annual Review of Fluid Mechanics*, Vol. 43, 2011, pp. 247–272.

[5] Jutte, C. V., Stanford, B. K., Wieseman, C. D., and Moore, J. B., "Aeroelastic tailoring of the NASA common research model via novel material and structural configurations," *52nd Aerospace Sciences Meeting*, American Institute of Aeronautics and Astronautics, January 2014. doi:10.2514/6.2014-0598.

[6] Jani, J. M., Leary, M., Subic, A., and Gibson, M. A., "A review of shape memory alloy research, applications and opportunities," *Materials & Design*, Vol. 56, 2014, pp. 1078–1113.

[7] Gibson, R. F., "A review of recent research on mechanics of multifunctional composite materials and structures," *Composite structures*, Vol. 92, No. 12, 2010, pp. 2793–2810.

[8] Blakey, S., Rye, L., and Wilson, C. W., "Aviation gas turbine alternative fuels: A review," *Proceedings of the combustion institute*, Vol. 33, No. 2, 2011, pp. 2863–2885.

[9] Suder, K., Delaat, J., Hughes, C., Arend, D., and Celestina, M., "NASA Environmentally Responsible Aviation Project's Propulsion Technology Phase I Overview and Highlights of Accomplishments," *51st AIAA Aerospace Sciences Meeting including the New Horizons Forum and Aerospace Exposition*, p. 414.

[10] Gohardani, A. S., Doulgeris, G., and Singh, R., "Challenges of future aircraft propulsion: A review of distributed propulsion technology and its potential

application for the all electric commercial aircraft," *Progress in Aerospace Sciences*, Vol. 47, No. 5, 2011, pp. 369–391.

[11] Campbell, R. L. and Lynde, M. N., "Natural Laminar Flow Design for Wings with Moderate Sweep," *34th AIAA Applied Aerodynamics Conference*, 2016, p. 4326.

[12] Barbarino, S., Bilgen, O., Ajaj, R. M., Friswell, M. I., and Inman, D. J., "A review of morphing aircraft," *Journal of intelligent material systems and structures*, Vol. 22, No. 9, 2011, pp. 823–877.

[13] Ivaldi, D., Secco, N. R., Chen, S., Hwang, J. T., and Martins, J. R. R. A., "Aerodynamic Shape Optimization of a Truss-Braced-Wing Aircraft," *Proceedings of the 16th AIAA/ISSMO Multidisciplinary Analysis and Optimization Conference*, Dallas, TX, June 2015. doi:10.2514/6.2015-3436.

[14] Gur, O., Bhatia, M., Mason, W. H., Schetz, J. A., Kapania, R. K., and Nam, T., "Development of a framework for truss-braced wing conceptual MDO," *Structural and Multidisciplinary Optimization*, Vol. 44, 2011, pp. 277–298. doi:10.1007/s00158-010-0612-9.

[15] Lyu, Z. and Martins, J. R. R. A., "Aerodynamic Design Optimization Studies of a Blended-Wing-Body Aircraft," *Journal of Aircraft*, 2014. doi:10.2514/1.C032491.

[16] Liebeck, R. H., "Design of the Blended Wing Body Subsonic Transport," *Journal of Aircraft*, Vol. 41, No. 1, 2004.

[17] Wakayama, S., *Multidisciplinary design optimization of the blended-wing-body*, American Institute of Aeronautics and Astronautics, 2016/02/21 1998. doi:doi:10.2514/6.1998-4938.

[18] Drela, M., "Development of the D8 transport configuration," *29th AIAA Applied Aerodynamics Conference*, 2011, p. 3970.

[19] Mader, C. A., Kenway, G. K. W., Martins, J. R. R. A., and Uranga, A., "Aerostructural Optimization of the D8 Wing with Varying Cruise Mach Numbers," *18th AIAA/ISSMO Multidisciplinary Analysis and Optimization Conference, Denver, CO*, 2017.

[20] Waitz, I. A., Lukachko, S. P., and Lee, J. J., "Military aviation and the environment: Historical trends and comparison to civil aviation," *Journal of aircraft*, Vol. 42, No. 2, 2005, pp. 329–339.

[21] Martins, J. R. R. A. and Lambe, A. B., "Multidisciplinary Design Optimization: A Survey of Architectures," *AIAA Journal*, Vol. 51, No. 9, September 2013, pp. 2049–2075. doi:10.2514/1.J051895.

[22] Haftka, R., "Structural optimization with aeroelastic constraints —- a survey of U.S. applications," *International Journal of Vehicle Design*, Vol. 7, 1986, pp. 381–392.

[23] Weisshaar, T. A., "Morphing aircraft systems: historical perspectives and future challenges," *Journal of Aircraft*, Vol. 50, No. 2, 2013, pp. 337–353.

[24] Martins, J. R. R. A., *Encyclopedia of Aerospace Engineering*, Vol. Green Aviation, chap. Fuel burn reduction through wing morphing, Wiley, October 2016, pp. 75–79. doi:10.1002/9780470686652.eae1007.

[25] Wright, O. and Wright, W., "O. & W. Wright Flying Machine," U.S. Patent 821393, May 1906.

[26] Friswell, M. I., "Hierarchical models of morphing aircraft," *23rd International Conference on Adaptive Structures and Technologies, ICAST*, 2012.

[27] Ivanco, T., Scott, R., Love, M., Zink, S., and Weisshaar, T., "Validation of the Lockheed Martin morphing concept with wind tunnel testing," *48th AIAA/ASME/ASCE/AHS/ASC Structures, Structural Dynamics, and Materials Conference*, 2007, p. 2235.

[28] Gilbert, W. W., "Mission adaptive wing system for tactical aircraft," *Journal of Aircraft*, Vol. 18, No. 7, 1981, pp. 597–602.

[29] BONNEMA, K. and SMITH, S., "AFTI/F-111 mission adaptive wing flight research program," *4th Flight Test Conference*, 1988, p. 2118.

[30] Wlezien, R., Horner, G., McGowan, A., Padula, S., Scott, M., Silcox, R., and Simpson, J., "The aircraft morphing program," *39th AIAA/ASME/ASCE/AHS/ASC Structures, Structural Dynamics, and Materials Conference and Exhibit*, 1998, p. 1927.

[31] Kudva, J. N., Martin, C. A., Scherer, L. B., Jardine, A. P., McGowan, A. R., Lake, R. C., Sendeckyj, G., and Sanders, B., "Overview of the DARPA/AFRL/NASA smart wing program," *Proc of 6th Ann Int Symp Smart Struct Mat, Newport Beach, USA, 1*, Vol. 3674, 1999.

[32] Kudva, J. N., Sanders, B. P., Pinkerton-Florance, J. L., and Garcia, E., "Overview of the DARPA/AFRL/NASA smart wing phase II program," *SPIE's 8th Annual International Symposium on Smart Structures and Materials*, International Society for Optics and Photonics, 2001, pp. 383–389.

[33] Kudva, J. N., Sanders, B. P., Pinkerton-Florance, J. L., and Garcia, E., "DARPA/AFRL/NASA Smart Wing program: final overview," *SPIE's 9th Annual International Symposium on Smart Structures and Materials*, International Society for Optics and Photonics, 2002, pp. 37–43.

[34] Szodruch, J. and Hilbig, R., "Variable wing camber for transport aircraft," *Progress in Aerospace Sciences*, Vol. 25, No. 3, 1988, pp. 297–328.

[35] Reckzeh, D., "Multifunctional wing moveables design of the A350XWB and the way to future concepts," *29th Congress of the International Council of the Aeronautical Sciences (ICAS), St. Petersburg, ISBN*, 2014, pp. 3–932182.

[36] Molinari, G., Quack, M., Dmitriev, V., Morari, M., Jenny, P., and Ermanni, P., "Aero-Structural Optimization of Morphing Airfoils for Adaptive Wings," *Journal of Intelligent Material Systems and Structures*, Vol. 22, No. 10, 2011, pp. 1075–1089. doi:10.1177/1045389X11414089.

[37] Molinari, G., Quack, M., Arrieta, A., Morari, M., and Ermanni, P., "Design, realization and structural testing of a compliant adaptable wing," *Smart Materials and Structures*, Vol. 24, No. 10, 2015, pp. 105027.

[38] Pankonien, A. M., *Smart Material Wing Morphing for Unmanned Aerial Vehicles*, Ph.D. thesis, University of Michigan, 2015.

[39] Kota, S., Hetrick, J. A., Osborn, R., Paul, D., Pendleton, E., Flick, P., and Tilmann, C., "Design and application of compliant mechanisms for morphing aircraft structures," *Smart Structures and Materials*, International Society for Optics and Photonics, 2003, pp. 24–33.

[40] Kota, S., Osborn, R., Ervin, G., Maric, D., Flick, P., and Paul, D., "Mission adaptive compliant wing–design, fabrication and flight test," *RTO Applied Vehicle Technology Panel (AVT) Symposium*, 2009.

[41] Kota, S., Flick, P., and Collier, F., "Flight Testing of the FlexFloil TM Adaptive Compliant Trailing Edge," *54th AIAA Aerospace Sciences Meeting*, 2016, p. 0036.

[42] Hetrick, J., Osborn, R., Kota, S., Flick, P., and Paul, D., "Flight testing of mission adaptive compliant wing," *48th AIAA/ASME/ASCE/AHS/ASC Structures, Structural Dynamics, and Materials Conference*, 2007, p. 1709.

[43] Miller, E. J., Cruz, J., Lung, S.-F., Kota, S., Ervin, G., Lu, K.-J., and Flick, P., "Evaluation of the Hinge Moment and Normal Force Aerodynamic Loads from a Seamless Adaptive Compliant Trailing Edge Flap in Flight," *54th AIAA Aerospace Sciences Meeting*, 2016, p. 0038.

[44] FlexSys, personal communication, Feb. 2016, Discussion with Gregory Ervin and Dragon Maric on 2/9/2016.

[45] Holland, J. H., "Genetic algorithms," *Scientific american*, Vol. 267, No. 1, 1992, pp. 66–73.

[46] Eberhart, R. and Kennedy, J., "A new optimizer using particle swarm theory," *Micro Machine and Human Science, 1995. MHS'95., Proceedings of the Sixth International Symposium on*, IEEE, 1995, pp. 39–43.

[47] Lyu, Z., Xu, Z., and Martins, J. R. R. A., "Benchmarking Optimization Algorithms for Wing Aerodynamic Design Optimization," *8th International Conference on Computational Fluid Dynamics (ICCFD8)*, Chengdu, China, July 2014, ICCFD8 2014-0203.

[48] Martins, J. R. R. A., Sturdza, P., and Alonso, J. J., "The Complex-Step Derivative Approximation," *ACM Transactions on Mathematical Software*, Vol. 29, No. 3, 2003, pp. 245–262. doi:10.1145/838250.838251.

[49] Martins, J. R. R. A. and Hwang, J. T., "Review and Unification of Methods for Computing Derivatives of Multidisciplinary Computational Models," *AIAA Journal*, Vol. 51, No. 11, 2013, pp. 2582–2599. doi:10.2514/1.J052184.

[50] Mader, C. A., Martins, J. R. R. A., Alonso, J. J., and van der Weide, E., "ADjoint: An Approach for the Rapid Development of Discrete Adjoint Solvers," *AIAA Journal*, Vol. 46, No. 4, April 2008, pp. 863–873. doi:10.2514/1.29123.

[51] Jameson, A., "Aerodynamic design via control theory," *Recent advances in computational fluid dynamics*, Springer, 1989, pp. 377–401.

[52] Reuther, J. J., Jameson, A., Alonso, J. J., Rimlinger, M. J., and Saunders, D., "Constrained Multipoint Aerodynamic Shape Optimization Using an Adjoint Formulation and Parallel Computers, Part 1," *Journal of Aircraft*, Vol. 36, No. 1, 1999, pp. 51–60. doi:10.2514/2.2413.

[53] Reuther, J. J., Jameson, A., Alonso, J. J., Rimlinger, M. J., and Saunders, D., "Constrained Multipoint Aerodynamic Shape Optimization Using an Adjoint Formulation and Parallel Computers, Part 2," *Journal of Aircraft*, Vol. 36, No. 1, 1999, pp. 61–74. doi:10.2514/2.2414.

[54] Hicken, J. E. and Zingg, D. W., "Induced-drag minimization of nonplanar geometries based on the Euler equations," *AIAA journal*, Vol. 48, No. 11, 2010, pp. 2564–2575.

[55] Hicken, J. E. and Zingg, D. W., "Aerodynamic optimization algorithm with integrated geometry parameterization and mesh movement," *AIAA journal*, Vol. 48, No. 2, 2010, pp. 400–413.

[56] Lyu, Z., Kenway, G. K., Paige, C., and Martins, J. R. R. A., "Automatic Differentiation Adjoint of the Reynolds-Averaged Navier–Stokes Equations with a Turbulence Model," *21st AIAA Computational Fluid Dynamics Conference*, San Diego, CA, Jul. 2013. doi:10.2514/6.2013-2581.

[57] Jameson, A., Pierce, N., Martinelli, L., Jameson, A., Pierce, N., and Martinelli, L., "Optimum aerodynamic design using the Navier-Stokes equations," *35th Aerospace Sciences Meeting and Exhibit*, 1998, p. 101.

[58] Nielsen, E. J. and Anderson, W. K., "Aerodynamic design optimization on unstructured meshes using the Navier-Stokes equations," *AIAA journal*, Vol. 37, No. 11, 1999, pp. 1411–1419.

[59] Lyu, Z., Kenway, G. K. W., and Martins, J. R. R. A., "Aerodynamic Shape Optimization Investigations of the Common Research Model Wing Benchmark," *AIAA Journal*, Vol. 53, No. 4, apr 2015, pp. 968–985. doi:10.2514/1.j053318.

[60] Haftka, R. T., "Optimization of flexible wing structures subject to strength and induced drag constraints," *AIAA Journal*, Vol. 15, No. 8, 1977, pp. 1101–1106.

[61] Martins, J. R. R. A., Alonso, J. J., and Reuther, J. J., "A Coupled-Adjoint Sensitivity Analysis Method for High-Fidelity Aero-Structural Design," *Optimization and Engineering*, Vol. 6, No. 1, March 2005, pp. 33–62. doi:10.1023/B:OPTE.0000048536.47956.62.

[62] Martins, J. R. R. A., Alonso, J. J., and Reuther, J. J., "High-fidelity aerostructural design optimization of a supersonic business jet," *Journal of Aircraft*, Vol. 41, No. 3, 2004, pp. 523–530.

[63] Kenway, G. K. W., Kennedy, G. J., and Martins, J. R. R. A., "Scalable Parallel Approach for High-Fidelity Steady-State Aeroelastic Analysis and Adjoint Derivative Computations," *AIAA Journal*, Vol. 52, No. 5, 2014, pp. 935–951. doi:10.2514/1.J052255.

[64] Kenway, G. K. W., Kennedy, G. J., and Martins, J. R. R. A., "Aerostructural optimization of the Common Research Model configuration," *15th AIAA/ISSMO Multidisciplinary Analysis and Optimization Conference*, Atlanta, GA, June 2014.

[65] Dhert, T., Ashuri, T., and Martins, J. R. R. A., "Aerodynamic Shape Optimization of Wind Turbine Blades Using a Reynolds-Averaged Navier–Stokes Model and an Adjoint Method," *Wind Energy*, 2016. doi:10.1002/we.2070.

[66] Garg, N., Kenway, G. K. W., Lyu, Z., Martins, J. R. R. A., and Young, Y. L., "High-fidelity Hydrodynamic Shape Optimization of a 3-D Hydrofoil," *Journal of Ship Research*, Vol. 59, December 2015, pp. 209–226. doi:10.5957/JOSR.59.4.150046.

[67] Henry, A. C., Molinari, G., and Arrieta, A. F., "Smart Morphing Wing: Optimization of Distributed Piezoelectric Actuation," *25th AIAA/AHS Adaptive Structures Conference*, 2017, p. 0294.

[68] Gamboa, P., Vale, J., P. Lau, F., and Suleman, A., "Optimization of a morphing wing based on coupled aerodynamic and structural constraints," *AIAA journal*, Vol. 47, No. 9, 2009, pp. 2087–2104.

[69] Hansen, N., Müller, S. D., and Koumoutsakos, P., "Reducing the time complexity of the derandomized evolution strategy with covariance matrix adaptation (CMA-ES)," *Evolutionary computation*, Vol. 11, No. 1, 2003, pp. 1–18.

[70] Lyu, Z. and Martins, J. R. R. A., "Aerodynamic Shape Optimization of an Adaptive Morphing Trailing Edge Wing," *Journal of Aircraft*, Vol. 52, No. 6, November 2015, pp. 1951–1970. doi:10.2514/1.C033116.

[71] Urnes, J., Nguyen, N., Ippolito, C., Totah, J., Trinh, K., and Ting, E., "A Mission Adaptive Variable Camber Flap Control System to Optimize High Lift and Cruise Lift to Drag Ratios of Future N+ 3 Transport Aircraft," *51st AIAA Aerospace Sciences Meeting, Grapevine, TX*, 2013.

[72] Kaul, U. K. and Nguyen, N. T., "Drag Optimization Study of Variable Camber Continuous Trailing Edge Flap (VCCTEF) Using OVERFLOW," *AIAA Paper*, Vol. 2444, 2014.

[73] Ting, E., Dao, T., and Nguyen, N., "Aerodynamic Load Analysis of a Variable Camber Continuous Trailing Edge Flap System on a Flexible Wing Aircraft," *AIAA SciTech Conference*, 2015, pp. 5–9.

[74] Stanford, B., "Static and Dynamic Aeroelastic Tailoring with Variable Camber Control," *15th Dynamics Specialists Conference*, 2016, p. 1097.

[75] Wakayama, S. and White, E. V., "Evaluation of Adaptive Compliant Trailing Edge Technology," *33rd AIAA Applied Aerodynamics Conference, AIAA*, Vol. 3289, 2015.

[76] Kennedy, G. J. and Martins, J. R. R. A., "A parallel aerostructural optimization framework for aircraft design studies," *Structural and Multidisciplinary Optimization*, Vol. 50, No. 6, 2014, pp. 1079–1101. doi:10.1007/s00158-014-1108-9.

[77] Hwang, J. T., *A Modular Approach to Large-scale Design Optimization of Aerospace Systems*, Ph.D. thesis, University of Michigan, 2015.

[78] Gray, J. S. and Martins, J. R. R. A., "Approach to Modeling Boundary Layer Ingestion using a Fully Coupled Propulsion-RANS Model," 2017.

[79] Kenway, G. K. W. and Martins, J. R. R. A., "Multipoint High-fidelity Aerostructural Optimization of a Transport Aircraft Configuration," *Journal of Aircraft*, Vol. 51, No. 1, 2014, pp. 144–160. doi:10.2514/1.C032150.

[80] Liem, R. P., Kenway, G. K. W., and Martins, J. R. R. A., "Multimission Aircraft Fuel Burn Minimization via Multipoint Aerostructural Optimization," *AIAA Journal*, Vol. 53, No. 1, January 2015, pp. 104–122. doi:10.2514/1.J052940.

[81] Kennedy, G. J., Kenway, G. K., and Martins, J. R. R. A., "High Aspect Ratio Wing Design: Optimal Aerostructural Tradeoffs for the Next Generation of Materials," *AIAA Science and Technology Forum and Exposition (SciTech), National Harbor, MD*, January 2014.

[82] Brooks, T. R., Kennedy, G. J., and Martins, J. R. R. A., "High-fidelity Multipoint Aerostructural Optimization of a High Aspect Ratio Tow-steered Composite Wing," *Proceedings of the 58th AIAA/ASCE/AHS/ASC Structures, Structural Dynamics, and Materials Conference, AIAA SciTech Forum*, January 2017. doi:10.2514/6.2017-1350.

[83] Samareh, J. A., "Survey of shape parameterization techniques for high-fidelity multidisciplinary shape optimization," *AIAA journal*, Vol. 39, No. 5, 2001, pp. 877–884.

[84] Sederberg, T. W. and Parry, S. R., "Free-form Deformation of Solid Geometric Models," *SIGGRAPH Comput. Graph.*, Vol. 20, No. 4, Aug. 1986, pp. 151–160. doi:10.1145/15886.15903.

[85] Lyu, Z. and Martins, J. R. R. A., "Aerodynamic Shape Optimization of an Adaptive Morphing Trailing Edge Wing," *Proceedings of the 15th AIAA/ISSMO Multidisciplinary Analysis and Optimization Conference*, Atlanta, GA, June 2014, AIAA 2014-3275.

[86] Kenway, G. K., Kennedy, G. J., and Martins, J. R. R. A., "A CAD-free Approach to High-Fidelity Aerostructural Optimization," *Proceedings of the 13th AIAA/ISSMO Multidisciplinary Analysis Optimization Conference, Fort Worth, TX*, 2010. doi:10.2514/6.2010-9231.

[87] Luke, E., Collins, E., and Blades, E., "A fast mesh deformation method using explicit interpolation," *Journal of Computational Physics*, Vol. 231, No. 2, 2012, pp. 586–601.

[88] van der Weide, E., Kalitzin, G., Schluter, J., and Alonso, J., "Unsteady Turbomachinery Computations Using Massively Parallel Platforms," *44th AIAA Aerospace Sciences Meeting and Exhibit*, 2006. doi:10.2514/6.2006-421.

[89] Kenway, G. K. W., Mishra, A., Secco, N. R., Duraisamy, K., and Martins, J. R. R. A., "An Efficient Parallel Overset Method for Aerodynamic Shape Optimization," *58th AIAA/ASCE/AHS/ASC Structures, Structural Dynamics, and Materials Conference*, 2017, p. 0357.

[90] Kennedy, G. J. and Martins, J. R. R. A., "A Parallel Finite-Element Framework for Large-Scale Gradient-Based Design Optimization of High-Performance Structures," *Finite Elements in Analysis and Design*, Vol. 87, September 2014, pp. 56–73. doi:10.1016/j.finel.2014.04.011.

[91] Brown, S. A., "Displacement Extrapolation for CFD+CSM Aeroelastic Analysis," *Proceedings of the 35thAIAA Aerospace Sciences Meeting, Reno, NV*, 1997, AIAA 1997-1090.

[92] Kao, J. Y., Hwang, J. T., and Martins, J. R. R. A., "A Modular Approach for Mission Analysis and Optimization," *56th AIAA/ASME/ASCE/AHS/ASC Structures, Structural Dynamics, and Materials Conference*, 2015.

[93] Gill, P. E., Murray, W., and Saunders, M. A., "SNOPT: An SQP Algorithm for Large-Scale Constrained Optimization," *SIAM journal on optimization*, Vol. 12, No. 4, 2002, pp. 979–1006. doi:10.1137/S1052623499350013.

[94] Perez, R. E., Jansen, P. W., and Martins, J. R. R. A., "pyOpt: a Python-based object-oriented framework for nonlinear constrained optimization," *Structural and Multidisciplinary Optimization*, Vol. 45, No. 1, 2012, pp. 101–118. doi:10.1007/s00158-011-0666-3.

[95] Wächter, A. and Biegler, L. T., "On the implementation of an interior-point filter line-search algorithm for large-scale nonlinear programming," *Mathematical Programming*, Vol. 106, No. 1, 2006, pp. 25–57. doi:10.1007/s10107-004-0559-y.

[96] Kraft, D., "A Software Package for Sequential Quadratic Programming," Tech. rep., Tech. Rep. DFVLR-FB 88-28, DLR German Aerospace Center, 1988.

[97] Haarhoff, P. C., Buys, J. D., Von Molendorff, H., and Africa., S., *Conmin: a computer programme for the minimization of a non-linear function subject to nonlinear constraints, by P. C. Haarhoff, J. D. Buys [and] H. von Molendorff*, Atomic Energy Board Pelindaba [South Africa], 1969.

[98] Audet, C., Le Digabel, S., and Tribes, C., "NOMAD user guide," Tech. Rep. G-2009-37, Les cahiers du GERAD, 2009.

[99] Le Digabel, S., "Algorithm 909: NOMAD: Nonlinear Optimization with the MADS algorithm," *ACM Transactions on Mathematical Software*, Vol. 37, No. 4, 2011, pp. 44:1–44:15. doi:10.1145/1916461.1916468.

[100] Svanberg, K., "The method of moving asymptotesa new method for structural optimization," *International Journal for Numerical Methods in Engineering*, Vol. 24, No. 2, 1987, pp. 359–373. doi:10.1002/nme.1620240207.

[101] Jansen, P. W. and Perez, R. E., "Constrained structural design optimization via a parallel augmented Lagrangian particle swarm optimization approach," *Computers & Structures*, Vol. 89, 2011, pp. 1352–1366. doi:10.1016/j.compstruc.2011.03.011.

[102] Deb, K., Pratap, A., Agarwal, S., and Meyarivan, T., "A Fast and Elitist Multiobjective Genetic Algorithm: NSGA-II," *Evolutionary Computation, IEEE Transactions on*, Vol. 6, No. 2, 2002, pp. 182–197. doi:10.1109/4235.996017.

[103] Hicks, R. M., Murman, E. M., and Vanderplaats, G. N., "An Assessment of Airfoil Design by Numerical Optimization," Tech. Rep. NASA-TM-X-3092, NASA, 1974.

[104] Hicken, J. E. and Zingg, D. W., "Aerodynamic Optimization Algorithm with Integrated Geometry Parameterization and Mesh Movement," *AIAA journal*, Vol. 48, No. 2, 2010, pp. 400–413. doi:10.2514/1.44033.

[105] Vassberg, J., Dehaan, M., Rivers, M., and Wahls, R., "Development of a Common Research Model for Applied CFD Validation Studies," *26th AIAA Applied Aerodynamics Conference*, American Institute of Aeronautics and Astronautics, August 2008. doi:10.2514/6.2008-6919.

[106] Lyu, Z., *High-Fidelity Aerodynamic Design Optimization of Aircraft Configurations*, Ph.D. thesis, University of Michigan, Ann Arbor, 2014.

[107] Chen, S., Lyu, Z., Kenway, G. K. W., and Martins, J. R. R. A., "Aerodynamic Shape Optimization of the Common Research Model," *AIAA Science and Technology Forum and Exposition (SciTech), Kissimmee, FL*, January 2014, AIAA-2015-1718.

[108] Kenway, G. K. W., Kennedy, G. J., and Martins, J. R. R. A., "Aerostructural Optimization of the Common Research Model Configuration," *15th AIAA/ISSMO Multidisciplinary Analysis and Optimization Conference*, Atlanta, GA, June 2014, AIAA 2014-3274.

[109] Anonymous, "777-200/300 Airplane Characteristics for Airport Planning," Tech. Rep. D6-58329, Boeing Commercial Airplanes, July 1998.

[110] Kenway, G. K. W. and Martins, J. R. R. A., "High-fidelity aerostructural optimization considering buffet onset," *Proceedings of the 16th AIAA/ISSMO Multidisciplinary Analysis and Optimization Conference*, June 2015.

[111] Kennedy, G. J., Kenway, G. K., and Martins, J. R. R. A., "A Comparison of Metallic, Composite and Nanocomposite Optimal Transonic Transport Wings," Tech. rep., NASA, March 2014, CR-2014-218185.

[112] Liem, R. P., Martins, J. R. R. A., and Kenway, G. K., "Expected Drag Minimization for Aerodynamic Design Optimization Based on Aircraft Operational Data," *Aerospace Science and Technology*, Vol. 63, April 2017, pp. 344–362. doi:10.1016/j.ast.2017.01.006.

[113] Kenway, G. K. W. and Martins, J. R. R. A., "Multipoint Aerodynamic Shape Optimization Investigations of the Common Research Model Wing," *AIAA Journal*, Vol. 54, January 2016, pp. 113–128. doi:10.2514/1.J054154.

[114] Hwang, J. T. and Martins, J. R. R. A., "A fast-prediction surrogate model for large datasets," *Aerospace Science and Technology*, 2017, Submitted: May 21, 2017.